The Dissertation Committee for Tarik Ali Khan Certifies that this is the approved version of the following dissertation:

Delivery of Vaccines and Therapeutics to Treat Infectious Diseases

Committee:

Jennifer Maynard, Supervisor

George Georgiou

Donald Paul

Krishnendu Roy

Phillip Tucker

Alan Watts

Delivery of Vaccines and Therapeutics to Treat Infectious Diseases

by

Tarik Ali Khan, B.A.Ch.; B.S.Ch.E.; M.S.E.

Dissertation

Presented to the Faculty of the Graduate School of

The University of Texas at Austin

in Partial Fulfillment

of the Requirements

for the Degree of

Doctor of Philosophy

The University of Texas at Austin

December 2012

Dedication

I dedicate this work to all my friends and family who have supported me throughout my life and during my graduate studies.

Acknowledgements

I would like to thank Dr. Jennifer Maynard for all of her support, guidance, and expertise during my graduate studies. I would also like to thank all of the individuals that contributed or helped support the science and execution of my work, in particular current and past members of the Maynard lab group, my committee members, and many other students and faculty at The University of Texas at Austin.

Delivery of Vaccines and Therapeutics to Treat Infectious Diseases

Tarik Ali Khan, Ph.D.

The University of Texas at Austin, 2012

Supervisor: Jennifer Maynard

Efficient delivery of vaccines and therapeutic agents *in vivo* is a critical aspect for ensuring a desired immunological or biological response is achieved. This work focuses on developing effective delivery systems for vaccines and therapeutics to achieve biological potency while maintaining patient friendly administration.

Traditional vaccines are administered via parenteral injection, which requires skilled personnel for administration and does not elicit strong mucosal immune responses. An alternative approach is to develop an oral vaccine; however, this requires antigens to be protected during transit through the gastrointestinal tract and be transported across specialized intestinal sampling cells called M cells. These M cells are extremely rare, making them an important target for oral vaccines. The protein invasin, from *Yersinia psuedotuberculosis*, naturally binds α5β1 integrin, a receptor found exclusively on M cells within the gastrointestinal tract. Therefore, we generated combinatorial libraries of invasin, followed by a directed evolution and high-throughput screening strategy to identify invasin variants with increased affinity towards α5β1 integrin. This process led to the creation of an invasin variant exhibiting a nine-fold decrease in EC_{50}, which could be used for targeted oral vaccine systems.

In order to test for increased vaccine efficacy due to the engineered invasin ligand, we developed a polymeric microparticle delivery system. These microparticles

were formulated to encapsulate the model antigen ovalbumin and be decorated with the invasin targeting ligands. To measure physiological trafficking and intestinal retention, novel fluorescent nanocrystals were loaded into particles conjugated to invasin. These nanocrystals served as a contrast agent for *in vivo* imaging in mice. While these particles were unsuccessful in generating an antibody response toward ovalbumin when administered to mice, a response directed to the targeting ligand itself was observed. These findings provide insights for further optimizing a delivery system for oral vaccination.

In addition to developing an oral vaccine delivery system, we created a high concentration therapeutic protein formulation, suitable for low-volume subcutaneous administration. By adding crowding agents, we were able to generate reversible protein nanoclusters with low viscosity. These nanoclusters were found to revert to monomer upon dilution and pharmacokinetic profiles similar to solutions.

Table of Contents

Chapter 3

List of Tables

List of Figures

Chapter 1: Introduction and Background

Critical cellular recognition and processes must take place in order for a successful adaptive immune response to be implemented. One key recognition event takes place when a professional antigen presenting cell (APC) presents a peptide, representative of an immunogenic antigen, on a major histocompatibility complex (MHC) to a naïve T cell. The T cell then goes on to induce a cellular, humoral, or suppressive immune response by interacting with other cells (Figure 1). While it is possible to induce T cell independent humoral immunity, young children cannot efficiently elicit such a response and memory T cells help provide long lasting protection (1, 2). Once a naïve helper T cell (TH0) is properly stimulated by an APC, it can go on to activate B cells in the form of TH1 or TH2 cells, initiating class switching and ultimately produce an antibody response. TH1 responses tend to induce an acute proinflammatory response, but provide long lasting protection by inducing memory T cells. The TH1 response can be characterized by antigen specific IgG2a in mice or IgG1 in humans. TH2 responses are capable of inducing memory B cells, IgG1(murine), IgG2(human), and IgA responses, but may also produce unwanted IgE antibodies. Therefore, a balanced CD4+ TH1/TH2 response is preferred to provide a complete cellular and humoral protection from extracellular pathogens. Immune responses to intracellular pathogens such as viruses rely primarily on activation of CD8+ T cells, which recognize infected cells and signal them for apoptosis.
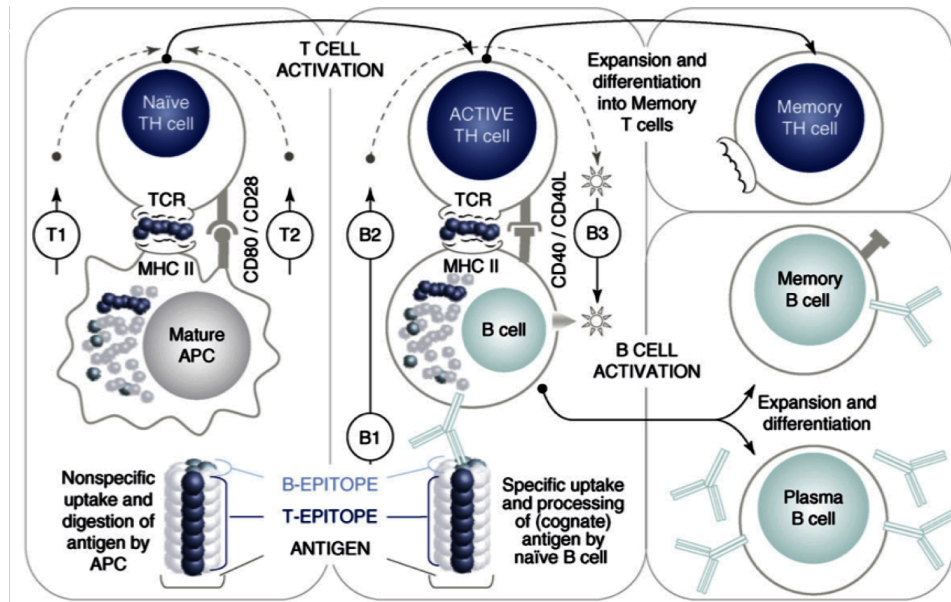
Figure 1.1: T-cell dependent humoral response mechanism. This image was reproduced with permission (3).

Vaccines tend to focus on modulating two main processes: antigen recognition and co-stimulation. When vaccinating against a virus, it is important to achieve MHC class I presentation. The pathway leading to this type of presentation relies on the antigen being free in the cytosol of cells. Attenuated viruses slowly replicate inside cells leading to their proteins being found in the cytosol. While attenuated viruses are very capable of inducing complete immune responses, the safety concerns of reversion into virulent strains push vaccine technology towards acellular and DNA vaccines (4). For MHC class I presentation, acellular and DNA vaccines must release their payload in the cytosol after being endocytosed by APCs. Endosomal release can be achieved by incorporating a buffering agent with the delivered payload, which acts as a proton sponge and ultimately lyses endosomes (5). To protect against extracellular pathogens a humoral, or antibody mediated response, is needed. For induction of a humoral response via MHC class II

presentation, no special modifications need to be done to lyse endosomes. However, B cell epitopes must be preserved to allow for proper affinity maturation of antibodies. Another area for optimization is to increase the duration of antigen recognition. Sustained in vivo antigen recognition increases the strength and duration of antibody responses, which can supersede that of multiple booster dosing (6). This sustained recognition can be achieved by using attenuated replicating pathogens, DNA vaccines, and polymeric controlled release systems.

Outside of antigen recognition, T cells respond to signals such as co-stimulation and extracellular cytokines. These signals direct T cells to either suppress or stimulate a protective immune response. Professional APCs are capable of displaying co-stimulatory molecules such as CD80, CD86, and CD40. Naive T cells recognizing these molecules, in association with an MHC-peptide complex, will be strongly directed to induce a protective immune response. Conversely, cytokines such as IL-10 and TGF-β will signal naïve T cells to become suppressors of antigens they recognize. Therefore, it is beneficial for vaccines to stimulate the expression of co-stimulatory molecules and/or suppress cytokines such as IL-10 and TGF-β (7). By incorporating adjuvants, immunomodulatory molecules, other than the antigen alone, stronger immune responses can be created. Although adjuvants are quite beneficial in increasing immune responses, some can lead to excessive inflammation raising safety concerns.

ORAL VACCINE DELIVERY SYSTEMS

Traditional vaccines have been administered by intramuscular injection, with the exception being the oral polio vaccine (OPV). Great efforts are being made to produce vaccines capable of oral administration. Oral is the preferred route for any therapeutic due to ease of administration, which leads to increased patient compliance. Cost per dose is also decreased as the need for trained administration and needles is reduced. Oral dosage forms are also considered to be safer and have reduced purity requirements compared to injectables (8). With regards to vaccines, oral administration mimics natural pathogen exposure leading to a more complete immune response by activating both the mucosal and systemic immune system (9). This activation of the mucosal immune system leads to a secretory IgA (SIgA) response. SIgA is extremely effective at protecting the body by doing the following: transporting into mucosal secretions, resisting proteolytic degradation, being produced at high amounts (>50 mg/kg body weight), inhibiting pathogen adhesion and invasion, and reducing inflammatory effects of other immunoglobulins. Clinical studies have shown immunological memory and protection develop from oral infection with pathogens such as Vibrio cholera further suggesting oral vaccination is a suitable approach to establish long lasting immunity (10).

Although oral vaccination appears to be capable of eliciting a more complete immune response, it has not dominated the market due to several critical challenges. One key hurdle is antigen degradation during transit through due to low pH and proteolytic environment in the stomach. The other major issue is that the antigens must cross through the gut lumen for antigen presentation. The two primary mechanisms for transit occur

through M cells and the less well understood transepithelium dendritic cells (DCs) (11-14). M cells are rare cells, found in the gastrointestinal tract (GIT) of adult humans at a rate of 1 in every 10,000,000 epithelial cells (15). These two factors coupled together result in very low bioavailability for oral vaccines. Another aspect to consider is the lack of a safe and well-understood mucosal adjuvant. Aluminum salts are generally regarded as safe (GRAS) and are the primary adjuvants used with commercial human vaccines (16). However, aluminum salts have not proven effective when employed with mucosal vaccines. New mucosal vaccines are being developed and studied such as bacterial toxins, CpG DNA, immune stimulating complexes (ISCOMs), virus-like particles (VLPs), compound 48/80, etc (17-19).

Only a handful of oral vaccines have demonstrated success in humans for targets such as Vibrio cholera, Salmonella typhi, rotavirus, and poliomyelitis (8). Low antigen presentation may be major limitation of subunit based oral vaccines. Live-attenuated vaccines have proven to be more effective due to their ability to replicate after crossing the epithelium barrier (20). This replication helps to not only increase the amount of antigen available for T and B cell recognition, but can also increase co-stimulation. However, live-attenuated vaccines possess the ability to mutate into a virulent strain. While strict screening of manufactured batches can help alleviate this concern, mutated vaccine excreted by the patients may go on to infect others.

In order to decrease safety concerns, acellular subunit vaccines are being developed. While these subunit vaccines are not capable of replicating and are therefore believed to be safer, their efficacy has been hindered by limited delivery to

immunomodulatory cells and a lack of adjuvanticity (21). To overcome these hurdles, efforts are being made to target antigens to certain regions in the GIT, incorporate antigens into delivery systems for protection during GIT transit, and/or promote uptake (9). The oral vaccination delivery system of choice has been antigens entrapped in micro and nano particles composed of poly(lactic-co-glycolic acid) (PLGA). PLGA is attractive due to its ability to slowly hydrolyze into nontoxic molecular components making it biocompatible. Optimization of PLGA formulations leads to particles that slowly release the entrapped antigen, which is capable of acting as a booster. Single intramuscular doses of antigen entrapped in PLGA have induced comparable antibody titers to repeated doses of antigen adsorbed to alum (6, 22). Many authors have demonstrated the quality of the antigen can be jeopardized during formulation by exposure to oil/water interface and during release due to low pH. The primary quality control concerns are denaturation, acylation, deamidation, and the formation of irreversible aggregates (23, 24). Adjusting the formulation method and including excipients that stabilize and buffer can address many of these concerns. However, successful immunogenicity has been achieved without such modifications.

MUCOSAL IMMUNE SYSTEM

Designing more effective oral vaccines involves a solid understanding of the mucosal-associated lymphoid tissue (MALT). Historically, the mucosal immune system has not been studied in as much detail as the systemic immune system, likely due to the same challenges associated with mucosal vaccinations. However, the mucosa is the front

line for pathogen as well as innocuous antigen encounters. The gut-associate lymphoid tissue (GALT) contains 70% of the body's lymphocytes and has co-evolved with commensal bacteria to produce balanced immune responses (25, 26). The GALT is composed of both organized tissue and lymphocytes scattered throughout the epithelium and lamina propria (connective tissue directly beneath the epithelium) depicted below.
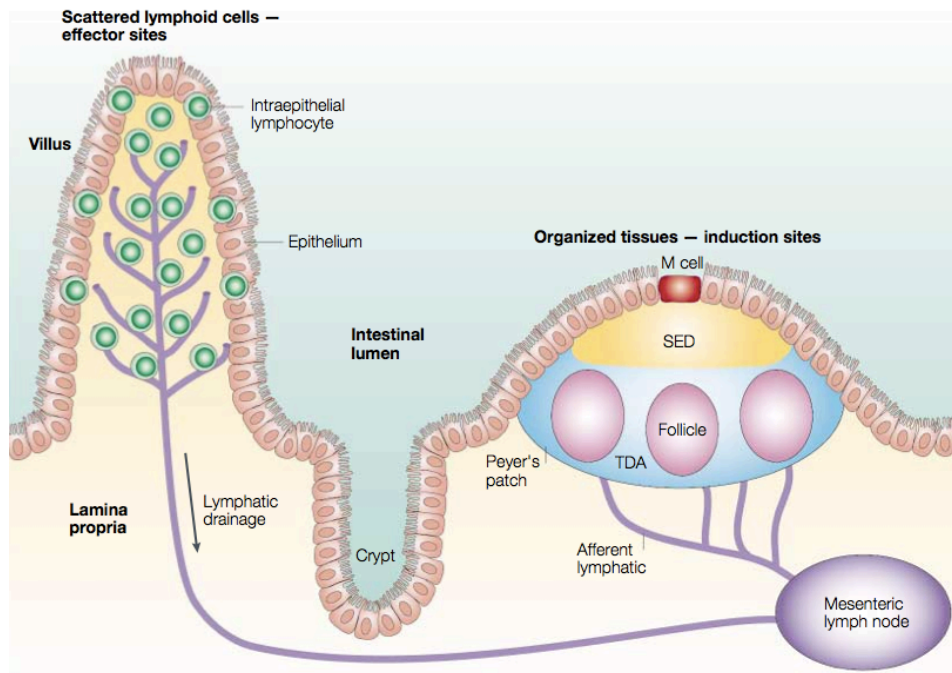
Figure 1.2: Representation of the GALT lymphatic system. This image was reproduced with permission (27).

The two organized tissues most important for initiating GALT related immune responses are Peyer's patches and mesenteric lymph nodes (MLNs). MLNs may play a critical role in bridging the mucosal and peripheral immune responses. The Peyer's patches are aggregated lymphoid regions just beneath the epithelium in the lower small intestine. These regions are composed of germinal centers and rich amounts of TGF-β and IL-10. In the absence of co-stimulatory signals these cytokines tend to promote the

development of regulatory T cells (Tregs) or a TH2 response, producing antigen specific IgA. In humans, Peyer's patches can be found in the GI tract as early as gestation all the way through adulthood, while reaching their peak (~250) during puberty (28, 29). They begin to appear in the jejunum, but are most frequently found in the ileum. Shown below is the luminal surface of a Peyer's patch, which appears as a macroscopic dome exhibiting a reduced brush border structure.
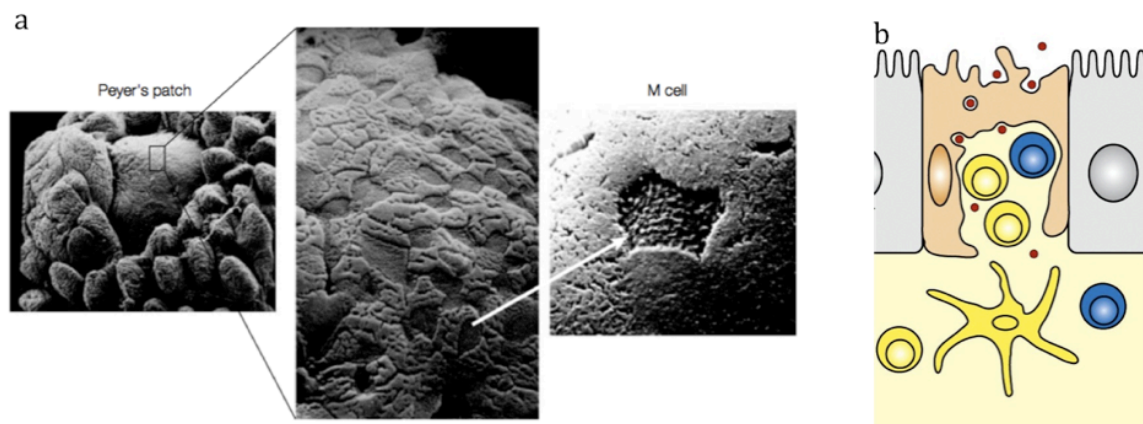
Figure 1.3: Structure of Peyer's patch and M cell. (A) SEM image of the luminal surface (27); (B) Schematic of the cross section of an M cell (1). These images were reproduced with permission.

The surface of Peyer's patches, also called the follicle-associated epithelium (FAE), can be distinguished by the presence of microfold (M) cells. The percent of M cells, compared to other cells, in the FAE is reported to be species dependent: ~50% in rabbits, ~10% in mice, and <5% in humans (30). While frequencies greater than 50% have been found in the caecum of humans, the extra M cells appear to have different characteristics (31). M cells are different from regular epithelial cells in that they do not possess microvilli, lack a mucus layer, do not express MHC class II molecules, have fewer lysosomes, and have an invaginated pocket where lymphocytes reside (27, 32). M

cells act as a channel for transporting antigens, particulates, viruses, and bacteria from the lumen to the Peyer's patch. The properties of the material to be transported, such as size, surface charge, and presence of ligands, controls the mechanism of transport by different processes such as phagocytosis, clathrin-mediated endocytosis, and macropinocyctosis (25). The endosome is then transferred to the basolateral surface where the material is released. The transcytosis process can occur in as little as 10 minutes (33). Once the transported material is acquired in the Peyer's patch, lymphocytes are able to interact with the material to gain acquired immunity or tolerance.

The importance of M cells in transcytosing material from the lumen to mucosal lymphocytes coupled with their scarcity illuminates the value of developing targeted vaccine systems. In order to target these cells, markers distinct from regular epithelial cells must be identified and exploited. Historically, it has been difficult to determine receptors specific to the apical surface of M cells, since no stable M cell line exists. Researchers have relied on two methods to study M cells: isolating sections of the ileum and an in vitro M cell model. While isolating ileal sections containing Peyer's patches may be the more ideal method, it relies on live animals or humans. The isolation of murine Peyer's patches led to research using lectins targeting of α-L-fucose. Unfortunately, it was later discovered that this receptor is not specific to M cells in humans. A human in vitro M cell model was first demonstrated in 1997 by culturing the human Caco-2 cell line in transwell plates and adding freshly isolated Peyer's patch tissue from mice to the basolateral chamber (12). While this method showed conversion from the Caco-2 cell phenotype to the M cells, it still relied on animals for the model.

9

Since then others have modified the model by using the Raji B cell line in place of

Peyer's patch tissue to make the model animal free, shown below (34). This model, while

difficult to work with, has led to increase understanding of the properties and expression

characteristics of human M cells.
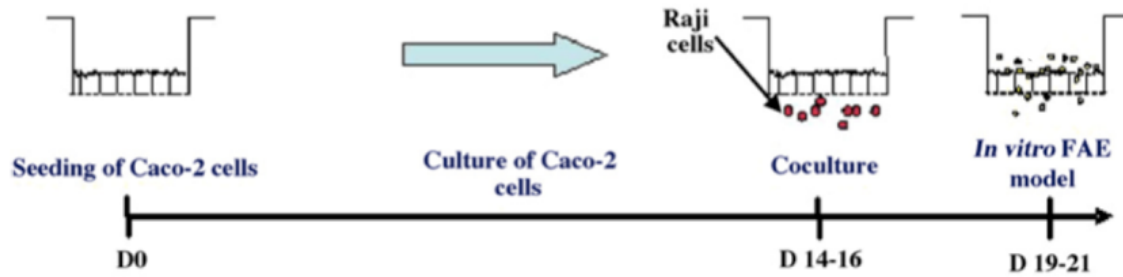
Figure 1.4: Development of the in vitro M cell model. This image was reproduced with permission (35).

While several markers have been discovered to be specific to apical M cell

expression, $\beta 1$ integrin stands out as a promising target as it has been verified in isolated

human tissue (36, 37). Further studies using the in vitro M cell model has revealed the

$\alpha 5\beta 1$ heterodimer is specific to the M cell apical surface and plays a role in transcytosis

(15). A naturally evolved bacterial ligand called invasin has been found to bind this

receptor with a K_d of 5.0 nM and 70 n M for the mutimeric and monomeric forms,

respectively (38). However, we believe this to be an underestimate of the affinity, which

will be discussed later. Another receptor specific to M cells in the GI tract is ganglioside

GM1. Cholera toxin B subunit (CTB), in its holotoxin form, has been identified as a high

affinity ligand binding with a K_d of 0.19 nM (39). This has led to CTB be being used as

the primary large molecule targeting ligand for oral vaccine development (39, 40).

However, it has also been shown that the SIgA and IgG can act as endogenous

competitors by also binding GM1, which is ultimately reduces CTB's effective affinity (41). The poor ability to express CTB coupled with the endogenous binding competitors makes invasin a more logical choice for a commercial oral vaccine targeting M cells. With the identification of molecular targets on M cells, researchers can begin to discover and develop ligands that target M cells with high affinity and specificity. Increased targeting and trancytosis have been demonstrated by controlling surface charge and/or receptor specific peptides (42, 43). However, the utilization of large targeting molecules, with increased surface area for binding, should greatly increase the efficacy by targeting M cells more efficiently.

While it is desired to induce protective immunity by vaccination, it is important to understand the natural tendency to develop oral tolerance. The human GALT has the very difficult task of maintaining a homeostatic balance of tolerance and immunity to the myriad of antigens, viruses, and microorganisms it encounters over its 100 m^2 of surface area (44). The gut has an estimated steady state population of 10^{14} commensal microbes (45). It is important for the GALT to maintain tolerance when appropriate to avoid conditions such as inflammatory bowel disease, Crohn's disease, and food allergies. The mechanisms that enable the identification of pathogens in the GALT are not clear. Some researchers have noticed a reduced role LPS is able to play on activation of intestinal lymph DCs, which likely aids in suppressing inflammation to commensal bacteria (46). Expanding on the "hygiene hypothesis," researchers have proposed that certain nonpathogenic microbial molecules, such as polysaccharide A, help balance the TH1/TH2 responses to minimize allergic reactions (47). The induction of acquired oral

tolerance is believed to occur at the T cell level. Large doses of an antigen is known to induce T cell anergy, while repeated low doses will initiate a regulatory T cell response (48, 49).

The means by which an APC presents an antigen is believed to direct T cell differentiation. DCs are considered to be the primary APC involved in T cell activation and several different DC subsets have been identified in the GALT. Some DC subsets are known to be spatially distinct inside the GALT, such as between intestinal epithelial cells (CX3CR1+) (50). Other DCs expressing CD103 are considered steady-state migrating lymph DCs (L-DCs), since they traffic from the Peyer's patch to the MLNs. CD4loCD172alo L-DCs are believed to maintain tolerance by carrying endocytosed fragments of apoptotic enterocytes to the draining lymph nodes (51). Plasmacytoid DCs have been implicated as playing a critical role in priming Tregs by upregulating the ICOS-L co-stimulatory molecule (52-54). Since different DC subsets can be found in different locations in the GALT, it is reasonable to hypothesize that the means in which an antigen is transported across the lumen may result in varied DC subsets presenting the antigen to T cells. This could ultimately determine whether T cells are directed towards a suppressive or stimulatory role. However, Milling et al. showed that different isolated L-DC subsets were not suppressive on their own, suggesting cytokines such as TGF-β, IL-10, and retinoic acid from other in vivo sources play an important role (51). It is known that several different Tregs exist in the GALT, some of which secrete TGF-β 26. The actions of natural Tregs and antigen specific Tregs is also not well understood, but likely play an important role in GALT immunomodulation. In short, in order to overcome the

natural propensity for tolerance, oral vaccines should possess some adjuvant activity. A
summary of identified GALT DC subsets is listed below.

Organ	Phenotype	Function
PP	CD11b$^+$ CD11c$^+$ cells	Produce IL-6 and induce IgA secretion
	CD11b$^+$ CD11c$^+$ cells	Produce high levels of IL-10 and low levels of IL-12, induce IL-4 and IL-10-producing CD4 T cells
	CD8α^+ CD11c$^+$ and CD11b$^-$ CD8α $^-$CD11c$^+$ cells	Produce IL-12p70
	CD11c$^+$ cells	Induce $\alpha_4\beta_7$ and CCR9 expression on B and T cells via RA
	IDO$^+$ CD11c$^+$ cells (from orally tolerized mice)	Induce CD4$^+$CD25$^+$Foxp3$^+$ T cells
	CD11b$^+$ CD11c$^+$ cells (from orally tolerized mice)	Generate CD4$^+$CD25$^+$ T cells
	pDC (B220$^+$ Gr1$^+$ CD11c^{int} cells)	Produce low levels of type I IFNs
MLN	CD103$^+$ CD11c$^+$ cells	Promote the generation of Foxp3$^+$ T cells via TGF-β and RA
	CD103$^+$ CD11c$^+$ cells	Induce $\alpha_4\beta_7$ and CCR9 expression on T cells
	pDC (induced by Flt3L: CD8α^+ B220$^+$ CD11c^{lo} cells)	Induce Tr1-like cells
	PDL2$^+$ (CD8α^-) CD11c$^+$ cells	Induce oral tolerance
	CD103$^+$ CD11c$^+$ cells (induced by cholera toxin)	Promote Th2 skewing via OX40
	CD11c$^+$ cells	Enhance TGF-β-dependent Foxp3$^+$ T cell differentiation by RA
	CD103$^-$ CD11c$^+$ cells	Promote the differentiation of IFN-γ-producing cells
LP	CD8α^- CD11b$^-$ CD11c$^+$ cells	Produce IL-12p40
	CD11b$^+$ CD11c$^+$ cells	Induce IL-17 production by CD4 T cells
	CD11c$^+$ cells (induced by Flt3L)	Express significant levels of IL-10 mRNA and low levels of IL-12p40 mRNA
	MHC class II$^+$ CD103$^{+/-}$ CD11c$^+$ cells	Promote the generation of Foxp3$^+$ T cells via TGF-β and RA
	$\alpha_v\beta_8$-expressing CD11c$^+$ cells	Induce Foxp3$^+$ T cells
	iNOS$^+$ CD11c$^+$ cells	Induce IgA production
	TLR5-expressing CD11c**hi** CD11b**hi** cells	Induce IgA production
Colon (human)	TSLP-treated CD11c$^+$ cells	Induce Th2-type responses

Table 1.1: Summary of subsets of dendritic cells in the GALT. This table was reproduced
with permission (55).

INVASIN: A NATURAL LIGAND FOR $\alpha5\beta1$ INTEGRIN

Although M cells have evolved to help the mucosal immune system sample the
contents of the lumen to distinguish pathogens from normal flora, pathogens such as
Salmonella typhimurium, *S. typhi*, *Yersinia pestis*, *Y. enterocolitica*, *Y.
pseudotuberculosis*, Enteropathogenic *Escherichia coli*, and *Shigella flexneri* are known
to selectively target M cells for infection (56). All three *Yersinia* pathogens possess a
chromosomal gene for a surface expressed protein called invasin, which has been
identified as a means for the pathogens to bind and increase translocation through

13

intestinal M cells (57). *Y. pseudotuberculosis* once translocated across M cells utilizes a type-III secretion system to inject effector proteins that compromise immune cell phagocytosis and recognition (58). The targeting of M cells is believed to be due to the interaction between invasin and apical M cell surface expressed α5β1 integrin (57, 59, 60). The specificity for α5β1 integrin, makes invasin an attractive targeting ligand for oral vaccines. The identification of invasin in 1987 by Isberg et al. has paved the way for research helping to understand the pathogenicity of several strains in the *Yersinia* genus (61). Unless specifically mentioned, "invasin" will refer to the variant from *Y. pseudotuberculosis*.

The incorporation of invasin on the surface of bacteria and inert particles has been shown to promote internalization by non-phagocytic cells (38). The mechanism of internalization appears to be linked to the ability to cluster β1 integrins and induce actin reorganization (62). Invasin is much more effective at inducing adhesion and internalization than the variant from *Y. enterocolitica* (63). The primary difference between these molecules is not due to affinity variations in the binding region, but the presence or absence of a domain that enables self-assembly. The extracellular region of invasin can be broken down into 5 domains, shown below.

D1	D2	D3	D4/D5
503-594	595-693	694-794	795-986
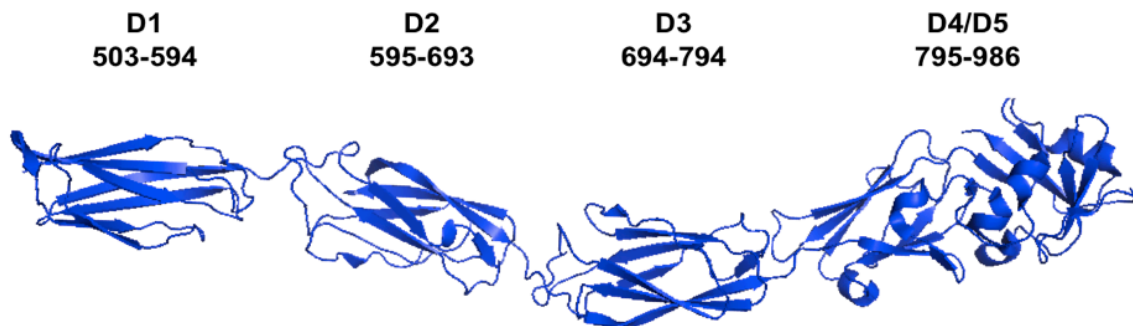
Figure 1.5: Crystal structure of the extracellular C-terminal region of invasin with domains defined by their amino acid range. This image was generated in Pymol using PDB entry 1CWV.

The D2 domain allows for the creation of dimers and tetramers, while the D4/D5 super domain is responsible for the binding event to certain β1 heterodimer integrins. Full-length invasin is 986 amino acids where the N-terminal 502 amino acids are used for translocation and localization to the outer membrane (62, 64). Portions of the extracellular region have been genetically fused to the C-terminal end of maltose binding protein (MBP) to produce soluble, stable, highly expressed protein (65). This has enabled protein-protein interactions to be studied, leading to a better understanding of critical sites and regions. Two cysteines, located at amino acid positions 907 and 982, have been shown to form a disulfide bond that is critical for receptor binding (66). Random mutagenesis, performed in strains harboring a mutazyme, and site-directed mutagenesis of invasin have revealed many residues that play a role in invasin's ability to facilitate adhesion and internalization (67, 68). The solvent exposed residues that appear to be most important are aspartic acid residues at positions 811 and 911 (66, 67).

Invasin has been shown to be capable of binding multiple heterodimers of β1 integrins, such as α3β1, α4,β1, α5β1, α6β1, αvβ1 (69, 70). However, invasin does not bind to α2β1 or the β2 forms of integrins. While α5β1 is the only known heterodimer to exist on the surface of M cells, the affinity for the other heterodimers may have resulted from an evolutionary pressure to aid infection after M cell translocation (71, 72). Integrins are known to play many roles both in cellular adhesion, differentiation proliferation, and survival. Once across the epithelium, many different cell types have

exposed integrins, which may be targeted. The endogenous ligand for α5β1 integrin is fibronectin, which contains the famous arginine-glycine-aspartic acid (RGD) sequence, exploited for different pharmaceutical targeting strategies. Interestingly, even though invasin does not possess an RGD peptide, it binds much tighter than fibronectin (73). The monomeric form of invasin (D2 domain deleted) and the multimeric form bind approximately 10 and 100 times tighter than fibronectin, respectively (38). Selective amino acid mutations on the β1 chain has further supported that both fibronectin and invasin utilize a similar β1 interface for binding (70). The mechanism of invasin-mediated invasion appears to be strictly due to affinity for α5β1 integrin, which initiates a zippering effect, shown below (38).
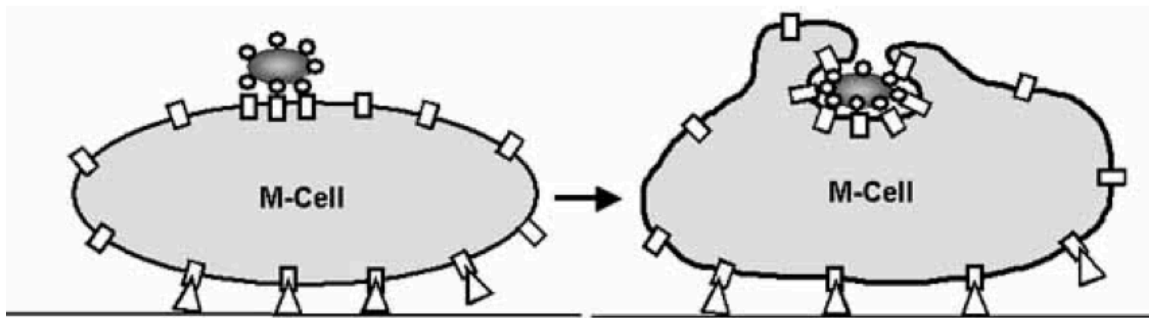
Figure 1.6: Zippering effect initiated by invasin. This image was reproduced with permission (74).

A positive correlation between integrin affinity and degree of internalization has been observed, using mAbs with varying affinities to α5β1 integrin (38). However, it has been shown that α5β1 integrin is able to alter its conformation from a relaxed state to a tensioned one (75). This has been shown to effect the affinity of fibronectin for α5β1

integrin. It is believed that fibronectin may bind in a two-step process, where one epitope (RGD) binds in the relaxed state and then upon mechanical tensioning the synergy site is engaged. This tensioning may be linked to the integrin clustering effect, triggering an intracellular signal cascade leading to engulfment of particles. It is speculated that invasin has a comparable binding interface used to bind α5β1 integrin, which is further supported by RGD competitive inhibition of invasin (73). It should be noted that the sequence homology between invasin and fibronectin is quite low and are not likely to have evolved from the same origin.
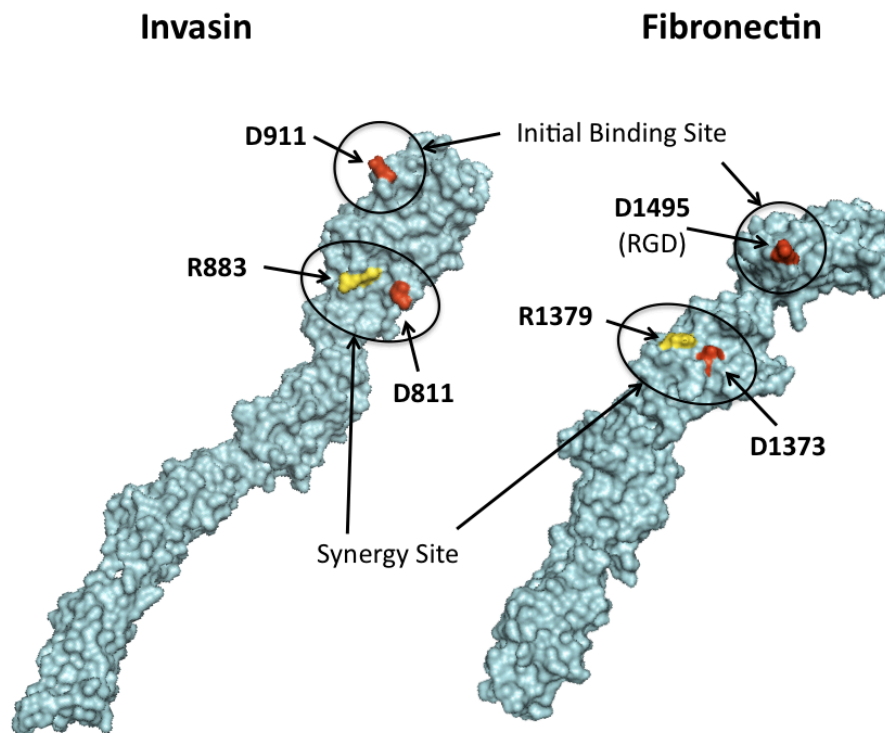
Figure 1.7: Comparison of the binding surfaces of invasin and human fibronectin.

Another interesting aspect of the invasin α5β1 interaction is the potential for adjuvant activity. The first evidence of invasin adjuvant activity was identified in 1993 by

co-immobilizing a monomeric MBP-invasin fusion with anti-CD3 on microplates and culturing isolated CD4+ and CD8+ human T cells (76). This study showed invasin was capable of mimicking co-stimulatory APC molecules by elevating cytokines such as interferon-γ (INF-γ) and tumor necrosis factor-α (TNF-α). Invasin was also able to activate CD8+ T cells to become cytotoxic effectors. By replacing invasin with different peptides from invasin, they were able to find the amino acids corresponding to 868-878 from invasin, were also able to stimulate adjuvant behavior. These effects were inhibited by the addition of anti-α5 integrin antibody, showing the adjuvant behavior was linked to integrins on the T cells. Particles coated with invasin from *Y. enterocolitica* are also able to induce IL-8 secretion from cultured epithelial cells (77). This behavior has been linked to a signal cascade triggered by clustering β1 integrins, shown below (78). This property means the utilization of invasion may serve dual purposes: targeting and immune stimulation. Therefore, an additional adjuvant may not be required to overcome oral tolerance and induce a protective immune response.
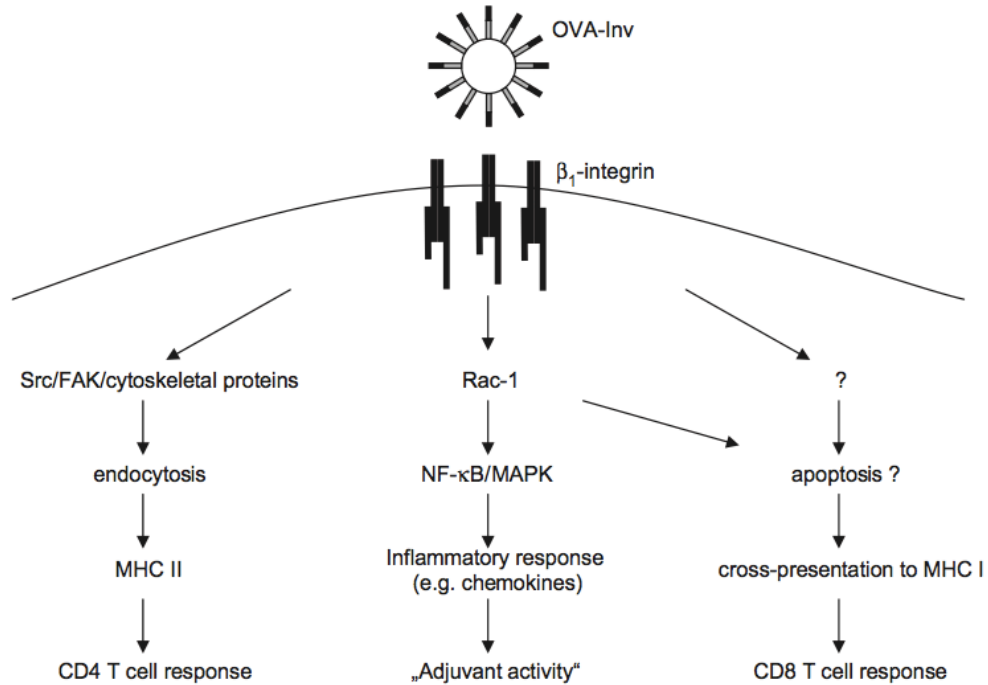
Figure 1.8: Potential signal cascade activation stimulated by invasin. This image was reproduced with permission (78).

Preliminary in vivo work testing invasin as a potential targeting molecule and immunomodulatory molecule has been successful. When carboxylated 0.5um fluorescent polystyrene particles were conjugated to invasin and orally administered to rats, approximately 13% of the particles were found in systemic circulation (79). This was a five-fold increase over controls with no enteric invasin protection mentioned. Another study tethered a fusion protein, consisting of c-terminal invasin and a fragment of ovalbumin (OVA), to carboxylated polystyrene particles (1um) and administered them by intraperitoneal injection (80). They were able to show a balanced TH1/TH2 response as well as CD8+ T cell stimulation using invasin. This supported the idea that invasin may have an ability to help promote cross-presentation which would not restrict its vaccine

targets to extracellular pathogens. Another study utilized live bacteria as a carrier, which expressed OVA, a protein to facilitate endosomal lysis, and invasin (81). These bacteria were orally administered and demonstrated suppressed growth of tumor cells expressing OVA. These examples provide promise for oral vaccines targeted by invasin.

Chapter 2: Engineering a Pathogenic Targeting Protein for Oral Vaccine Delivery

INTRODUCTION

Design of vaccines to induce mucosal immunity has been challenging (82), but are expected to confer robust protection since most infectious diseases gain entry via mucosal routes (4, 27, 83, 84). Oral vaccines are a promising approach due to their ease of administration and the option for solid dosage formulations with reduced cold-chain dependence. However, the only FDA approved oral vaccines have been live attenuated pathogens, including those for adenovirus, rotavirus, and typhoid. As live pathogens, these present safety concerns for their potential to revert to virulence, as observed with the Sabin live oral polio vaccine (85). In contrast, recent efforts have focused on particulate vaccines incorporating key proteins or epitopes from pathogens (86). While safer, these injectable formulations do not induce strong mucosal immune responses. Ideally, a vaccine would include recombinant subunits and be capable of inducing both mucosal and systemic immune responses.

An intriguing solution is the use of orally administered polymeric particles to protect a subunit vaccine during gastrointestinal (GI) transit, followed by targeting to lymphoid tissue in the gut (87). Vaccines targeting the rare M cells along the GI tract have shown improved immune responses, compared to untargeted formulations (40, 42). These M cells, which sample antigens and particulates in the GI tract, are believed to play a critical role in inducing immunity (88). They transport foreign material to underlying dendritic cells, B and T cell lymphocytes, which in turn initiate an immune response (27,

89). Because these cells are very rare, ~1 in every 10,000,000 human epithelial cells, vaccine potency may be increased by targeting M cells through a specific ligand-receptor interaction (4, 15, 29, 90). A variety of ligands appear promising in terms of increased IgG or IgA titers, IFN-gamma production and murine survival upon challenge, including the NKM 16-2-4 antibody, CKS9 peptide, UEA-1 lectin, and cholera toxin B subunit (40, 42, 71, 91-93).

Of these receptor-ligand pairs, the α5β1 integrin is unique to the human M cell surface, compared to other enterocytes (32, 57, 59). This receptor is also targeted by certain *Yersinia* bacteria, which present a surface-displayed invasin protein that adheres to the α5β1 integrin in order to facilitate infection (36, 61, 94). Bacteria expressing invasin increase the number of adherent bacteria ~10 fold and internalized bacteria ~2.5 fold in an in vitro M cell model, compared with bacteria not expressing invasin (36). When incubated with mouse intestinal loops, ~5 times more adherent and ~30 times more internalized bacteria were recovered from M cells for bacteria expressing versus not expressing invasin (57). Purified, adsorbed invasin is necessary and sufficient to mediate internalization of polystyrene beads into HEp-2 cells (62) and increases the systemic presence of particles 6.5-fold after oral dosing in mice (79).

The invasin from *Y. psuedotuberculosis* has been well-characterized, a large (107 kDa) protein anchored in the outer membrane by a beta-barrel transmembrane domain, with its five extracellular domains (D1-D5) forming an 18nm rod-like extension homologous to tandem type III fibronectin domains (Table 2.1) (95, 96). The domains D1-D4 are immunoglobulin-like while D5 is C-type lectin-like domain. The D2 domain

mediates self-assembly into dimers and tetramers, increasing the avidity of binding and efficiency of endocytosis (62, 96, 97). Receptor binding is mediated by the D4-D5 domains, containing two critical aspartic acids residues: D911 which is required for binding and D811 aids binding (Table 2.1) (67, 68). The orientation of these two residues suggests convergent evolution with the RGD and synergy sites of fibronectin, although this molecule has significantly weaker affinity for integrins (96). Invasin is efficiently expressed in E. coli as the intact, surface displayed protein, or as soluble protein when the D1-D5 or D4-D5 domains are fused to the c-terminus of maltose binding protein (MBP) (36, 73). In addition, invasin possesses adjuvant qualities, stimulating CD4 and CD8 T cell proliferation and cytokine release (76, 80). In the context of vaccine design, high intrinsic affinity for the α5β1 integrin and high invasin surface density on vaccine particles are expected to enhance immune responses to an oral vaccine (25, 29, 74, 90).

All studies to date have demonstrated a correlation between ability to target M cells and improve immune responses, suggesting M cell targeting/uptake has not yet been saturated and that higher affinity could enhance this effect. The potential for invasin to improve oral vaccine delivery led us to generate variants with enhanced α5β1 binding affinity and, presumably, enhanced M cell targeting in vivo. We first performed alanine scanning of eight invasin residues suspected to contribute to the binding interface, to aid in identification of regions to target with saturation mutagenesis. We identified four residues, which, when substituted with alanine for bacterial display, resulted in ~50% reduced binding to purified α5β1 integrin or ~50% reduction in Caco-2 cell invasion. Next, we constructed four site-directed saturation libraries targeting 31 residues within

the D4-D5 domains, followed by eukaryotic cell-based panning and FACS enrichment of bacterial-displayed libraries to identify affinity-enhanced invasin variants. We identified three mutations conferring increased affinity for α5β1, as measured by a flow cytometry-based assay and ELISA. Two of the substitutions created a novel RGD epitope surrounding the essential D911 residue that appears to mimic fibronectin's RGD epitope, while the third led to increased specificity and affinity towards the α5 subunit of the integrin complex. These results suggest invasin recognizes α5β1 in the same manner as fibronectin and may comprise a new targeting ligand for oral vaccines.

Domain	Residues	Function	Reference
SP	1-48	Translocation across inner membrane	(Fairman, 2012)
β	128-486	Outer membrane anchor	(Fairman, 2012)
D1	503-594		(Hamburger, 1999)
D2	595-693	Self-assembly	(Dersch, 1999), (Dersch, 2000), (Hamburger, 1999)
D3	694-794		(Hamburger, 1999)
D4/D5	795-986	Binding region	(Leong, 1991), (Hamburger, 1999)

Table 2.1: Important regions of invasin from *Y. psuedotuberculosis*

RESULTS AND DISCUSSION

Identification of four novel residues with reduced invasin-integrin binding upon alanine substitution

    Y. psuedotuberculosis invasin is a 107kDa adhesion protein embedded in the bacterial outer membrane with five extracellular domains extending outwards (96). The integrin binding interface is restricted to the terminal two extracellular domains (D4-D5), as determined by the ability of progressively truncated invasin variants to adhere to and

invade HEp-2 cells (65, 98). Subsequently, several key residues within the D4-D5 region were identified as key mediators of the binding interaction. Using a mutator E. coli strain to randomly introduce mutations into the invasin gene, followed by selection of clones no longer able to bind HEp-2 cells, the residues C907 and C982 were found to form a critical disulfide bond and the region spanning residues 903-913 was implicated in binding (68). A library of invasin variants, targeting the 903-913 region with mutagenic oligonucleotides, identified residue D911 as essential for integrin binding. Motivated by this result, all the aspartic acid and lysine residues in the D4D5 region were systematically substituted with alanine to identify additional key residues (67). The residue D811 was identified as an important residue, but less essential than D911. Finally, residues flanking D811 were substituted with alanine prior to analysis as soluble MBP fusion protein. Here, the F808A substitution was found to have a moderate effect in integrin binding, similar to that observed with the to D811A substitution.

Given this prior identification of several residues important for integrin binding, we chose construct targeted, saturation mutagenesis libraries, in which several adjacent residues are randomized to all other amino acid residues. This approach restricts the number of possible amino acid combinations present in each library, such that every protein variant can be analyzed. In addition to the D911 and D811 residues, we sought to identify additional residues on the invasin surface directly engaging α5β1 integrin to define regions likely to result in productive libraries. Due to their large size, restricted mobility, and ability to mediate electrostatic, hydrophobic, and hydrogen bonding interactions, solvent exposed tyrosine residues often contribute significantly to the

binding free energy of protein-protein interactions (99). Inspection of the invasin crystal structure revealed five solvent-exposed tyrosines in the D4-D5 region (Y860, Y863, Y878, Y885, and Y976), four of which had not been previously assessed for integrin binding activity (Figure 2.1A). The Y878 residue was previously implicated, as a decameric invasin peptide containing this residue engaged the α5β1 integrin on T cells (76).
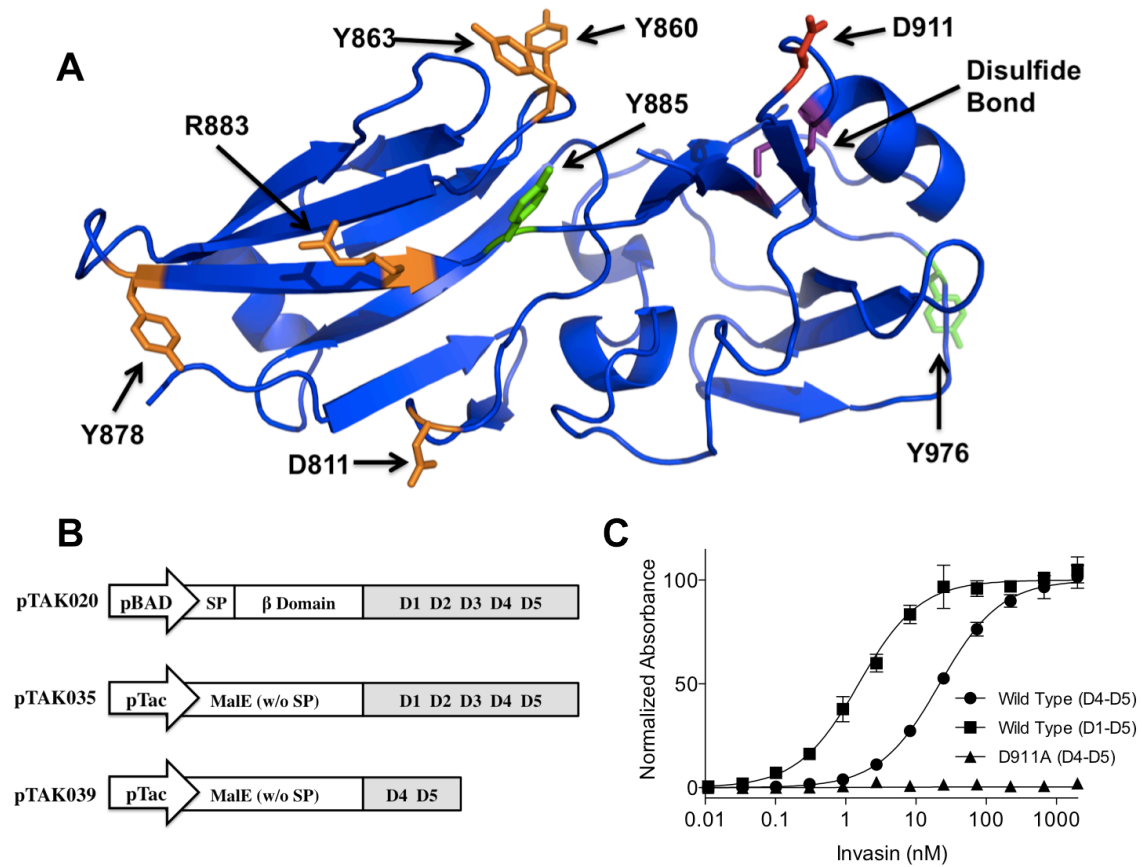
Figure 2.1: Integrin binding activity of purified invasin and D911A variant. (A) Structure of D4/D5 domains of invasin with residues color-coordinated based on relative importance to integrin binding or cell uptake. Green: minimal role; orange: moderate role; red: critical role. The single critical disulfide bond is shown in purple. The backbones for residues substituted in libraries are shown in cyan. From PDB entry 1CWV. (B) To display invasin on the surface of *E. coli* cells, the plasmid pTAK020 was constructed by inserting the complete invasin gene into the arabinose inducible pBAD30 plasmid. The entire 986 amino acid residue (107 kDa) protein is expressed, including the native translocation signal peptide (SP), outer membrane insertion region (β Domain), and five external domains (D1-D5). To produce soluble invasin, DNA encoding domains 1-5 (amino acid residues 503-986) or the minimal integrin binding domains 4 and 5 (residues 795-986) were introduced into the pMAL-c5x plasmid, for cytoplasmic expression as a c-terminal fusion to the *MalE* gene (encoding maltose binding protein, MBP) to create the MBP-D1D5 (93 kDa) and MBP-D4D5 (62 kDa) constructs, respectively. (C) ELISA demonstrating the impact of the D911A (▲) substitution on binding of MBP-D4D5 to immobilized α5β1 integrin, using anti-MBP for detection. For reference, the wild-type invasin sequence is shown for the multimeric MBP-D1D5 (■) and monomeric MBP-D4D5 (●) constructs.

This work utilized expression of the invasin gene in three different genetic constructs, consisting of bacterial surface display and soluble expression of the D1-D5 or D4-D5 domains as a fusion protein to MBP (Figure 2.1B). Using PCR-based mutagenesis, we introduced alanine residues to sequentially replace each of these five native tyrosines. We also generated alanine substitutions at residues previously found to contribute to binding, D811, D911, and the R883 residue which was postulated in Hamburger et al (96). Upon alanine substitution, the tyrosine side chain is reduced to a single methyl group, removing the hydrogen-bonds and hydrophobic interactions normally mediated by this residue, while minimally disturbing the native structure as alanines are highly represented in both alpha helix and beta sheet secondary structure elements. If a given tyrosine residue contributes significant free energy to stabilize the invasin-integrin binding interaction, we would expect to see a decrease in affinity or cellular invasion for the corresponding alanine variant. Regions adjacent to or encompassing these key residues would then be targets for mutagenesis to optimize the local interaction.

First, to measure invasin-integrin binding activity and to validate our work with existing data for the D911A variant (68), we developed an ELISA using recombinant soluble $\alpha5\beta1$ integrin as a coat protein and a soluble fusion protein of maltose binding protein (MBP) and the invasin D4-D5 domains (MBP-D4D5; Figure 2.1C). In this assay, wild-type invasin gave a strong response, while the D911A variant showed no response, consistent with prior reports. However, ELISA analysis requires time-consuming expression and purification of the soluble MBP-invasin fusion protein. In order to rapidly

screen large number of invasin variants, we developed two complementary assays based on bacterial display of invasin, followed by flow cytometry analysis or eukaryotic cell invasion. Full-length invasin was expressed in E. coli using an arabinose inducible promoter, resulting in translocation to and anchoring in the outer membrane. To confirm invasin presence on the cell surface, induced (+0.2% arabinose) cells were incubated with the invasin-specific monoclonal antibody 3A2 (65), followed by a fluorescent secondary antibody and analysis with flow cytometry. Bacteria expressing invasin exhibited a median fluorescence intensity (MFI) shift of several orders of magnitude (from ~0 to ~8000), compared to bacteria not expressing invasin (Figure 2.2A).
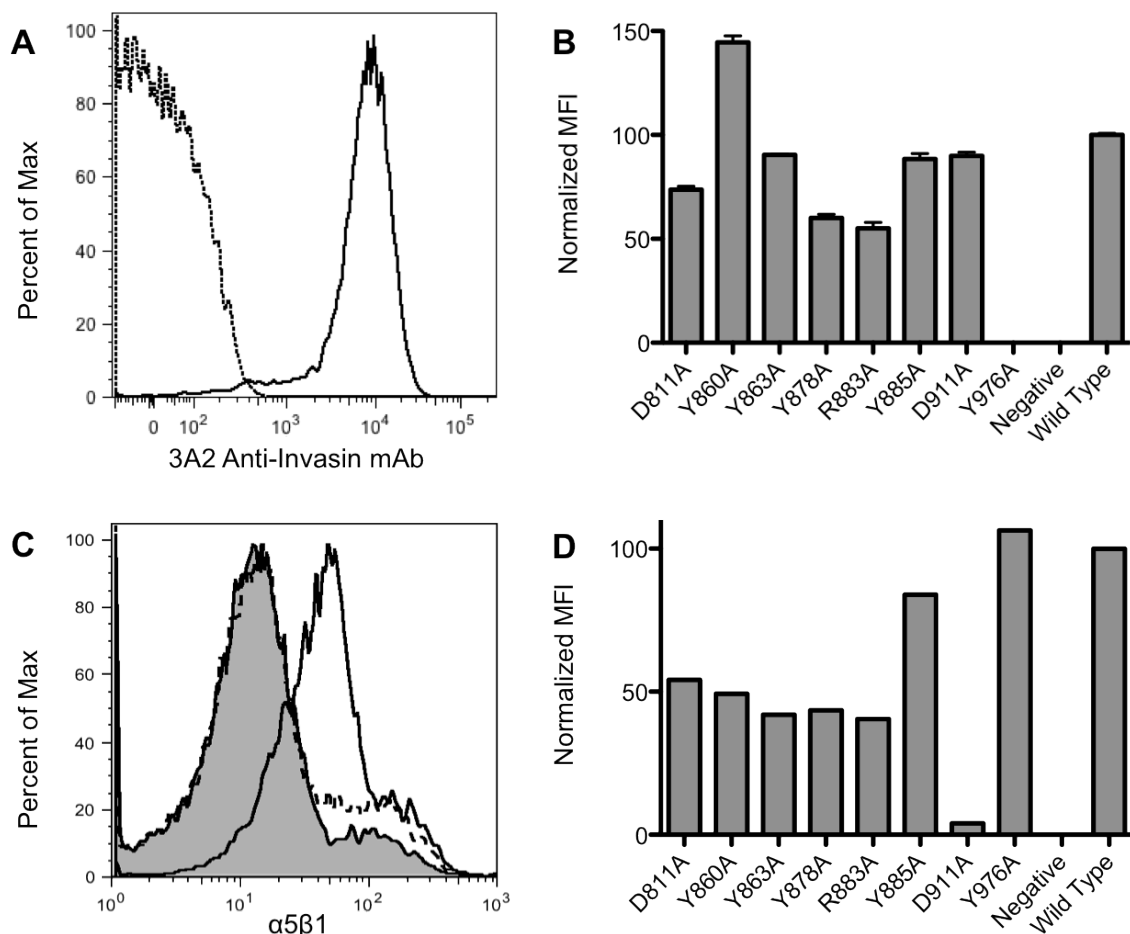
Figure 2.2: Alanine invasin variants exhibit a spectrum of integrin binding abilities. (A) Flow cytometry of *E. coli* displaying wild-type invasin as a histogram plot. Incubation with the 3A2 anti-invasin antibody and Cy5-labeled goat anti-mouse IgG results in a fluorescence shift for bacteria expressing invasin (solid line, MFI ~8,000) as compared to bacteria not expressing invasin (dashed line, MFI ~0). (B) Normalized MFI for the eight alanine variants and controls after incubation with the 3A2 anti-invasin antibody to assess differences in surface display levels. The Y976A variant appears to no longer bind the antibody. (C) Flow cytometry of E. coli displaying wild-type invasin after incubation with fluorescent, recombinant, soluble α5β1 integrin shows a fluorescence shift for bacteria expressing wild-type invasin (solid line, unshaded; MFI ~50) versus the non-binding D911A variant (dashed line, unshaded; MFI ~10), and bacteria not expressing invasin (solid line, shaded; MFI ~10). (D) Normalized MFI for the eight alanine variants and controls after incubation with fluorescent, α5β1 integrin demonstrate the effect of each residue change on integrin binding.

30

Having confirmed that invasin is present on the cell surface and accessible for ligand binding, we replaced the antibody with fluorescent, recombinant, soluble α5β1 integrin to monitor the protein-protein interaction of interest. The fluorescent integrin was prepared by coupling Alexa Fluor 647 to commercial extracellular α5β1, resulting in 5-15 fluorophores per protein. After incubation of cells with fluorescent integrin results in an increase in MFI for those expressing invasin (MFI ~40) versus those not expressing invasin or expressing the D911 variant (MFI~ 13; Figure 2.2C). Unfortunately, attempts to introduce a peptide tag into invasin to directly monitor the surface levels were unsuccessful (data not shown). We can thus only approximate changes in surface expression from 3A2 anti-invasin binding (Figure 2.2B).

Using bacterial FACS, MFI values were normalized such that cells expressing wild-type invasin were defined as 100 and cells not expressing invasin were defined as 0. (Figure 2.2D) The D911A variant again showed greatly reduced binding to the integrin (normalized value of 4), similar to bacteria not expressing invasin. The D811A, Y860A, Y863A, Y878A, and R883A variants all exhibit moderate reduction in integrin binding (normalized values of 40-55), suggesting these are less important or second-shell residues (stabilizing residues directly participating in the binding event), while Y885A and Y976A show wild type binding (normalized values between 84-106). Interestingly, the Y976A mutant, which is not recognized by the 3A2 antibody, retains wild-type affinity for integrin, suggesting that this residue is critical for antibody but not integrin binding.

Three residues with reduced integrin affinity also exhibit reduced Caco-2 invasion. The invasin-β1 integrin interaction is not just a simple binding event, but in the

context of a live cell, triggers an intracellular signaling cascade and actin reorganization, ultimately resulting in internalization of particles presenting invasin. While our primary concern is to increase the invasin affinity for α5β1 integrin, in order to enhance M cell targeting, it is also critical to retain the internalization abilities. Moreover, the integrin has been shown to exist in multiple conformations on the cell surface which may not be recapitulated by the soluble, recombinant α5β1 used above (75). Therefore, an orthogonal gentamicin protection assay was employed, to assess invasin-integrin binding and the resulting cellular internalization (81). Here, bacteria expressing surface displayed invasin variants and intracellular GFP were incubated with Caco-2 cells at a multiplicity of infection (MOI) of 70 for two hours, washed, then incubated with media containing gentamicin to kill extracellular bacteria. The next day, Caco-2 cells were analyzed by flow cytometry to monitor internalized bacteria via GFP fluorescence.

This assay provides a clear distinction between Caco-2 cells incubated with bacterial cells expressing invasin versus those lacking invasin. When incubated with bacteria harboring empty plasmid, the Caco-2 cells exhibit a single population with low fluorescence, while those incubated with bacteria displaying wild-type invasin devolve into low- and high-fluorescence populations (Figure 3.3A). Cells falling into the higher fluorescence window were defined as positive for invasion.
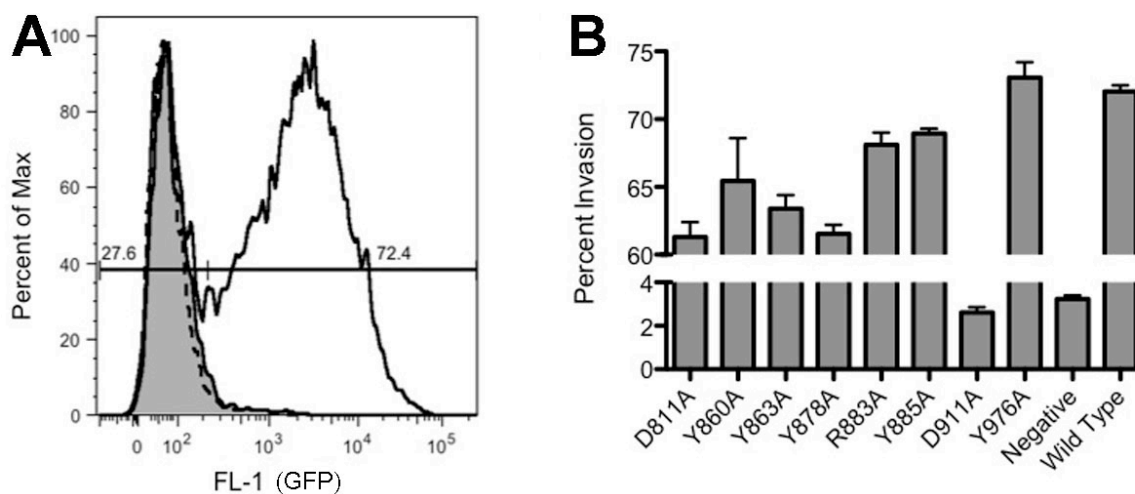
Figure 2.3: Alanine invasin variants confer a spectrum of cellular invasion abilities. (A) *E. coli* bacteria expressing intracellular GFP and displaying invasin are internalized by Caco-2 cells. After gentamycin treatment to kill extracellular bacteria following in vitro infection, the Caco-2 cells were analyzed for GFP fluorescence by flow cytometry. The histogram shows a population of Caco-2 cells with low-fluorescence after incubation with bacteria not expressing invasin (solid line, shaded) or those expressing the inactive D911A variant (dashed line, unshaded). Both low (27.6% of the total population) and high fluorescence populations (72.4% of the total population) are observed after incubation with bacteria expressing wild-type invasin (solid line, unshaded). All experiments were performed at an MOI of 70. (B) Bacteria expressing invasin alanine variants exhibit different Caco-2 invasion abilities. The percent of GFP-positive Caco-2 cells are presented to compare the effects of various alanine mutations. Percent invasion corresponds to the percent of cells in the high fluorescence population versus the total size-gated population.

Under optimized conditions, ~70% of Caco-2 cells incubated with bacteria expressing wild-type invasin were positive for invasion, while only ~3% of those incubated with bacteria lacking invasin (empty plasmid) or expressing the D911A substitution were positive for invasion (Figure 2.3B). Of the alanine variants, bacteria expressing the Y976A, Y885A and R883A invasin variants were able to infect Caco-2 cells at near-wild-type levels (68-73%), while the D811A, Y860A, Y863A, Y878A variants conferred reduced infectivity (all statistically significant differences from wild-

33

type P<0.001, but Y860A: P<0.01; 1-way ANOVA). This data is consistent with the direct binding analysis above, except for the R883A variant which showed moderately impaired binding in the FACS assay, but near-wild-type Caco-2 invasion.

Generation of four site-directed libraries targeting invasin hot spots

Given this structure-function knowledge of the invasin-integrin binding site, we chose to generate four site-saturation mutagenesis libraries surrounding key residues to fine-tune these specific interactions. Variants containing Y860A and Y863A were found to compromise both integrin-binding and Caco-2 cell invasion and are located on a single loop. Therefore, library 1 randomized ten residues: residues 858-865, which form the loop including Y860 and Y863 and residues F844 and N847, which are located on an adjacent loop with side chains oriented towards the 860-863 loop. Similarly, the Y878A and R883A substitutions moderately affect binding; library 2 targets these by randomizing the surface exposed residues on the beta sheet between positions 878-883. Library 3 surrounds the residue D811, targeting the surface loop between residues 809-814. Library 4 surrounds the essential residue D911, randomizing the 908-913 loop. Each library contained >10^7 unique transformants, which corresponded to greater than ten-fold more non-template sequences than the theoretical library size.

Identification of invasin variants with enhanced affinity for α5β1 integrin and Caco-2 invasion from site-directed libraries

Bacterial protein display in conjunction with FACS is well documented as a protein engineering tool allowing enhanced control over the selection process by providing single clone information in real time (100). However, flow cytometry alone is

unable to efficiently sort large libraries due to resolution and sorting rate limitations, restricting FACS enrichment to library sizes on the order of 10^7 (101). For larger libraries, pre-enrichment techniques, such as magnetic bead capture (102), can be used to reduce library sizes feasible for FACS enrichment. We chose a dual Caco-2 adhesion/ invasion and bacterial FACS selection platform, in which the Caco-2 step removes inactive or poorly active invasin variants while simultaneously rapidly reducing library size (Figure 2.4). Libraries were grown, induced and incubated with sub-confluent Caco-2 cells. After allowing time for bacteria to bind and invade, unbound bacteria removed by washing with retained and internalized bacteria recovered. The remaining library members were then subjected bacterial FACS with fluorescent integrin until the populations were enriched, as measured by a stable population MFI and sequence convergence.
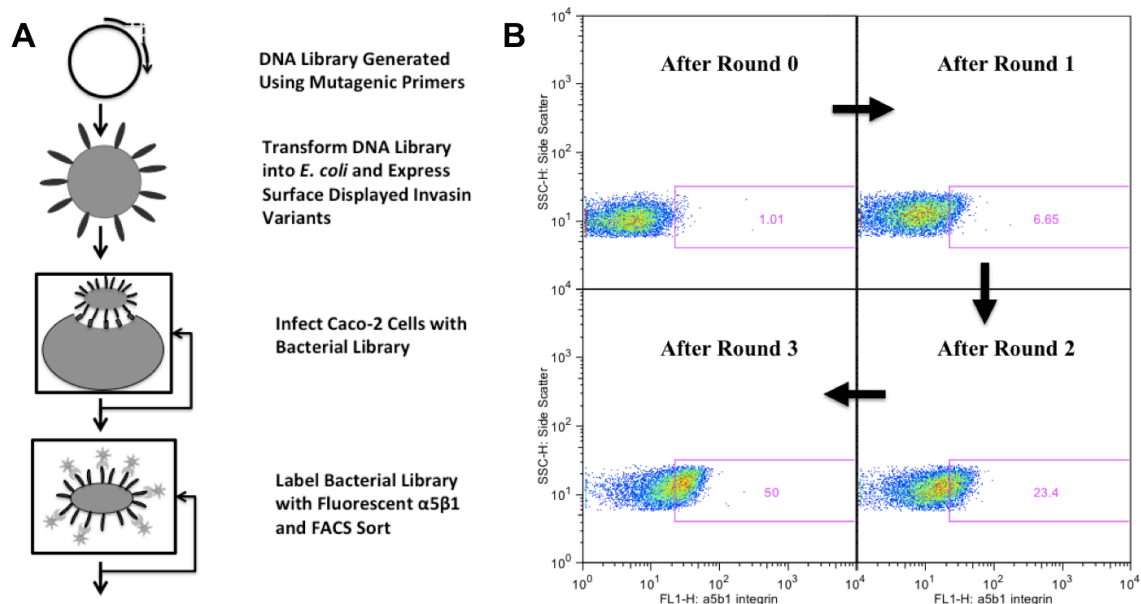
Figure 2.4: Selection of invasin variants from targeted libraries. (A) Overview of the invasin selection process. First, a targeted library is created using a single, degenerate, mutagenic primer, plasmid pTAK020 encoding the entire invasin gene with stop codons inserted in the mutagenic region, polymerase, and ligase before transformation into *E. coli*. Next, the library is enriched for functional invasin variants capable of mediating bacterial adherence to and invasion of bacteria into Caco-2 cells. Only internalized bacteria, harboring plasmid corresponding to the expressed invasin variant, are recovered. Last, recovered bacteria expressing surface displayed invasin are incubated with fluorescently labeled soluble α5β1 integrin and the more highly fluorescent clones enriched by multiple rounds of FACS to identify individual clones for more detailed characterization. (B) Representative data depicting the changing bacterial population during rounds of selection by FACS. Initially, the population as a whole is poorly fluorescent, with ~1% of events falling into the fluorescence gate for integrin binding. This population increases with each round of bacterial sorting until after three rounds, 50% of the population falls into this gate. Data shown for library one.

Each library was subjected to two rounds of Caco-2 selection and four rounds of bacterial FACS, followed by sequencing of individual clones (Figure 2.5). Clones are named for the library, sort round and isolate, i.e., isolate 2 analyzed from library 1 after four enrichment rounds is termed 1R4-2. For library 1, all positions were represented the most by the wild type amino acid, except for F844, at which position a tyrosine was

36

observed to be the most prevalent substitution (7 of 10 clones). Similarly, for library 2 only one position was represented the most by a non-wild type amino acid, S881V (8 of 10 clones). Library 3 did not exhibit sequence convergence although Y810P was present in six clones and the 814 position was restricted to the wild-type phenylanine (7 of 10 clones) or leucine (3 of 10 clones). Library 4, surrounding the critical D911 residue, exhibited sequence convergence more rapidly than the other libraries. All clones sequenced after two Caco-2 cell enrichment steps contained the wild-type D911 residue, while three of those sequenced after the first FACS sort further modified the D911 environment to include a RGD motif. Further rounds of enrichment and sequence analysis revealed the RGD to correlate with M912L and/or S913A substitutions.

A

Position	844	847	858	859	860	861	862	863	864	865
Wild Type	F	N	I	T	Y	Q	T	Y	S	E
Degenerate Codon	KHT	VAK	NTT	WMC	KHT	MAW	RSC	KHT	KHT	GAW
					Library 1					

B

Position	878	879	880	881	882	883	884	885	887	888
Wild Type	Y	S	V	S	Y	R	F	Y	N	R
Degenerate Codon	KHT	KHT	NTT	KHT	TMT	MRM	NTT	KHT	MAS	MRG
					Library 2					

C

Position	809	810	811	812	814
Wild Type	A	T	D	K	F
Degenerate Codon	NNS	NNS	NNS	NNS	NTT
			Library 3		

D

Position	908	909	910	911	912	913
Wild Type	Q	G	S	D	M	S
Degenerate Codon	NWW	NNC	NNC	KHT	NNS	KMT
			Library 4			

Figure 2.5: Sequence convergence observed in libraries after selection. The distribution of observed amino acid residues are shown as WebLogo frequency plots. Underneath, the residue's number, wild-type amino acid identity and the degenerate codon used for library generation. Six positions converged to a non-wild-type residue and are highlighted in yellow (F844Y, S881V, G909R, S910G, M912L, S913A).

Individual clones from each library were analyzed for increased integrin affinity by bacterial flow cytometry with fluorescent α5β1. The post-sort libraries 1, 2, and 4 each resulted in clones exhibiting increased MFI compared to bacteria expressing wild-type invasin (151, 179, and 132 normalized MFI values, respectively)(Figure 2.6A).

Based on the three variants analyzed from library 2, the S881V substitution was observed in both variants yielding increased MFI and was further suggested to be important by sequence homology in following the next round of FACS enrichment. The post-sort library 3, which did not exhibit sequence convergence, also did not exhibit an MFI greater than wild-type invasin. Library 3 was abandoned for further analysis due to the lack of clear sequence convergence and isolation of clones with poor performance in the bacterial flow cytometry assay.
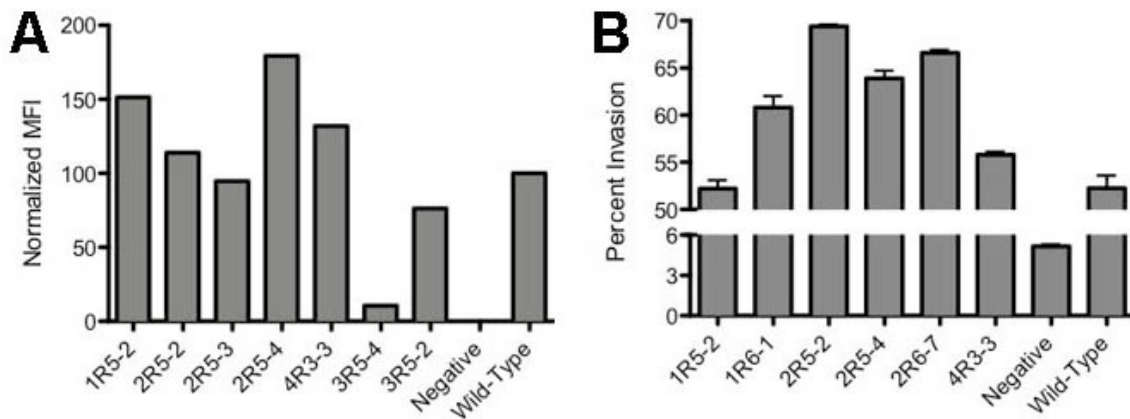
Figure 2.6: Invasin variants show enhanced integrin binding and cellular invasion. Non-homologous clones recovered from the last round of selection were analyzed by surface expression on *E. coli* cells followed by (A) incubation with fluorescent integrin prior to analysis with flow cytometry and (B) ability to invade Caco-2 cells.

Clone Name	Substitutions
1R5-2	F844A, N847H, I858V, Y863F, S864Y
1R6-1	F844Y
2R5-2	S879A, S881V
2R5-3	Y885S
2R5-4	S881V, R883K, Y885S
2R6-7	S881V
3R5-2	A809P, T810P, D811S, K812G, F814L
3R5-4	A809T, T810P, K812H, F814L
4R3-3	G909R, S910G, M912L, S913A
RGD	G909R, S910G
DLA	M912L, S913A
RGD844	F844Y, G909R, S910G

Table 2.2: Amino acid substitutions present in each clone, relative to c-terminal wild-type sequence. Clone nomenclature includes library, selection round and clone number, such that 1R5-2 is clone 2 from library 1 after round five.

Bacterial clones exhibiting a MFI higher than bacteria expressing wild-type invasin in the bacterial flow cytometry assay (Figure 2.6A), along with clones exhibiting sequence homology different from wild type were analyzed for Caco-2 cell invasion capability. Clones 1R6-1, 2R5-2, 2R5-4, and 2R6-7 all exhibited statistically significant improvements ($P<0.001$; 1-way ANOVA) for Caco-2 cell invasion, 52%, 69%, 64%, 67% respectively compared to 52% for wild type (Figure 6B and Table 2.2). Clone 1R6-1, including a single F844Y mutation, was selected for further characterization from library 1. All clones from library 2 shared a S881V mutation; for clone 2R6-7 this is the only change from wild-type sequence, leading to its selection as a lead from this library. While the 4R3-3 variant exhibited improved invasion, it was not statistically significant.

However, given its performance in both assays, along with the intriguing presence of an RGD epitope, it was also selected for further analysis.

The combination of three amino acid substitutions produces a nine-fold improvement in affinity to α5β1 integrin

Three lead candidates, based on bacterial flow cytometry and Caco-2 invasion screening (Figure 2.6), were sub-cloned into pTAK039 for expression as a soluble MBP-D4D5 fusion protein followed by ELISA to assess relative binding affinities for integrin. After cytoplasmic expression, amylose affinity and size exclusion chromatographic steps resulted in highly pure protein at the expected 62kDa size, based on amino acid sequence (Figure 2.7A). Purified protein yields were approximately 100 mg per liter culture volume for all variants. The 2R6-7 variant (S881V) from library 2 exhibited a higher EC_{50} than wild-type, indicating weaker binding (data not shown). This substitution may result in increased expression rather than increased integrin affinity. The lead candidates from libraries 1 (1R6-1) and 4 (4R3-3) exhibited statistically significant EC_{50} shifts, compared to wild-type (95% confidence intervals for EC_{50} shifts relative to wild-type: (1.8-2.4) and (3.2-4.1), respectively (Figure 2.7B).
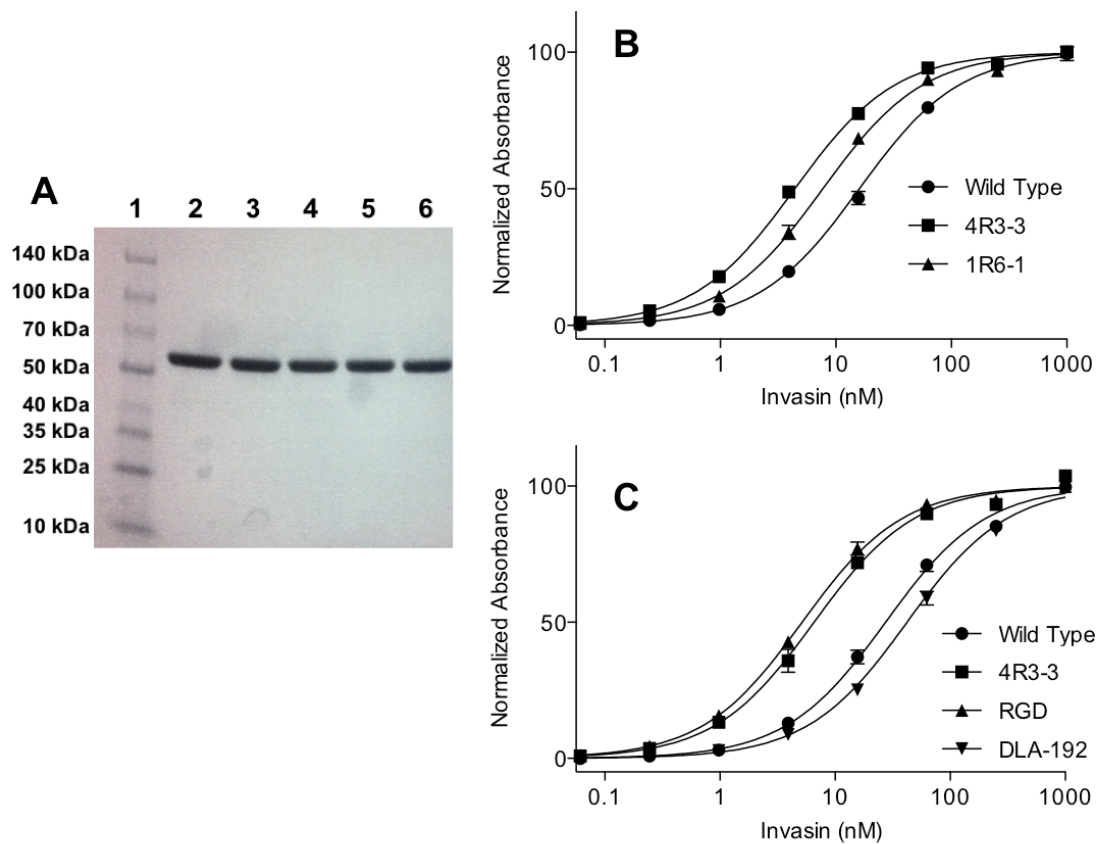
Figure 2.7: Contributions of individual amino acid substitutions in selected variants to integrin binding. Two lead candidates (4R3-3 and 1R6-1) were selected for further analysis on the basis of high fluorescence in the flow cytometry assay and high Caco-2 invasivity. As 4R3-3 contains multiple substitutions (GSDMS to RGDLA at positions 909-913), two additional variants were constructed to determine the contributions of the RGD and DLA motifs surrounding the essential D911 residue. The D4-D5 domains for all four variants were expressed and purified as MBP-D4D5 proteins from pTAK039. (A) Non-reducing SDS-PAGE depicts purified protein of the expected molecular weight (62 kDa). Lanes contain 1: Spectra Multicolor Broad Range Protein Ladder, 2: wild-type invasin, 3: clone 4R3-3, 4: clone 1R6-1, 5: variant with RGD, 6: variant with DLA. (B) ELISA comparing binding of clones 4R3-3 (■) and 1R6-1 (▲) with wild-type invasin (●) to α5β1 integrin. (C) ELISA comparing binding of clone 4R3-3 (■) with the RGD (▲), DLA (▼) variants and wild-type (●) invasin to α5β1 integrin. ELISA plates were coated with soluble α5β1 integrin and bound invasin detected with anti-MBP-HRP.

While the both invasin and fibronectin both bind integrin, invasin has a much

higher affinity for α5β1integrin: invasin K_d = 5 nM, while the fibronectin K_d = 800

42

nM)(73). Interestingly, while invasin also presents an aspartic acid residue essential for binding (D911), it lacks the classic RGD epitope found in fibronectin, which is necessary and sufficient to support integrin binding (67, 73, 74). From library 4, we isolated a variant (4R3-3) containing an RGD sequence surrounding D911, which bound $\alpha5\beta1$ more tightly than wild-type invasin (~four-fold decrease in EC_{50}). This 4R3-3 variant is composed of four substitutions between C-terminal residues 909-913 (GSDMS to RGDLA). To assess whether the GSD $\rightarrow$ RGD and DMS $\rightarrow$ DLA changes each contribute to increased affinity, we made a series of site-directed variants to assess the specific contributions of each set of changes. We found the DMS $\rightarrow$ DLA substitutions to actually decrease binding while the GSD $\rightarrow$ RGD substitution increase binding (Figure 2.7C).

Given that both the F844Y substitution and the RGD epitope individually confer increased affinity, we constructed a variant containing both sets of substitutions and analyzed its behavior as a bacterial cell surface displayed protein and as a soluble MBP-D4-D5 fusion protein. This protein, along with wild-type and the individual site mutation variants were expressed and purified as before to produce highly pure protein (Figure 2.8A). After ELISA analysis against $\alpha5\beta1$, we found our optimized invasin variant, RGD844, to have a lower EC_{50} than variants with either F844Y or the RGD epitope alone (Figure 2.8B). This resulted in a nine-fold increase in affinity, compared to wild-type invasin (Figure 2.8C). We then compared these variants on their ability to bind $\alpha3\beta1$ (Figure 2.8D). We found the variants containing the RGD epitope to also exhibit increased affinity [95% confidence intervals for EC_{50} shifts relative to wild-type: RGD

43

(1.39-2.73) and RGD844 (1.31-2.56)]. However, the F844Y substitution had little effect on affinity to $\alpha3\beta1$ (95% confidence intervals for EC_{50} shifts (0.516-1.01), relative to wild-type).
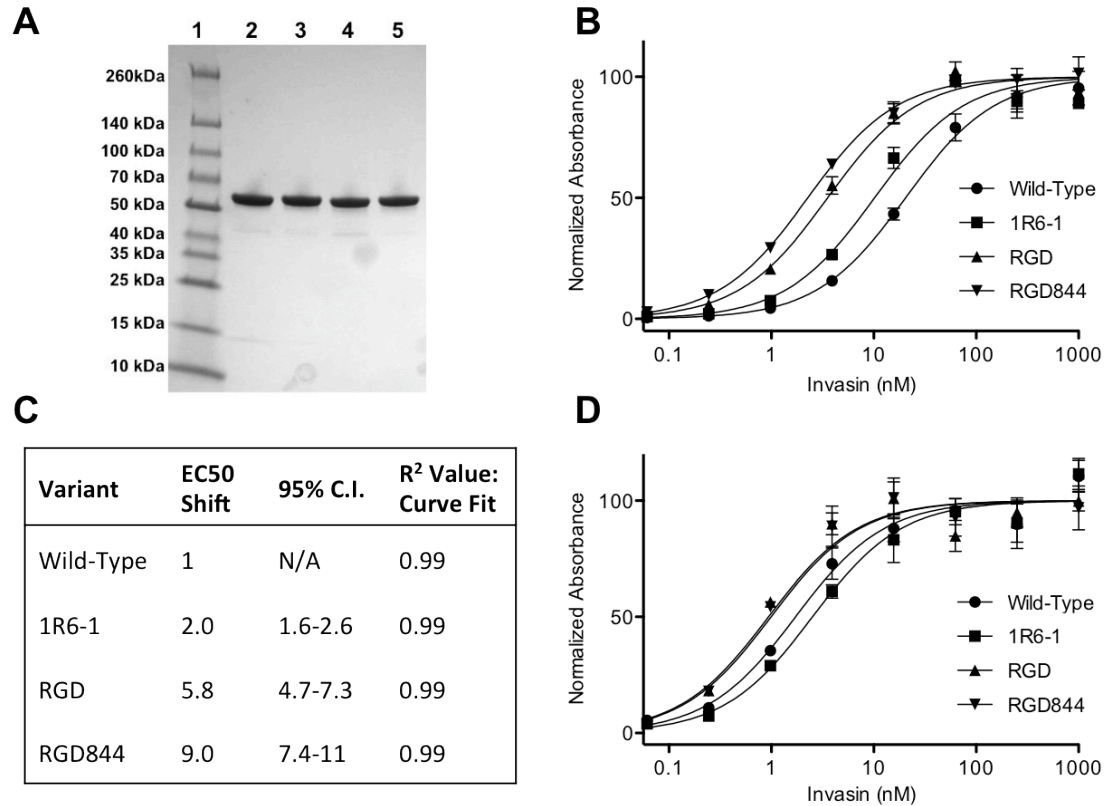
Figure 2.8: Lead invasin variant, RGD844 shows enhanced affinity and specificity for $\alpha5\beta1$ integrin. To determine whether the RGD motif and F844Y synergistically enhance invasin binding to integrin, they were introduced into invasin in the pTAK035 and pTAK039 plasmids for purification as MBP-D1D5 and MBP-D4D5 fusion proteins, respectively. (A) Non-reducing SDS-PAGE depicts purified protein of the expected molecular weights (94 kDa). Lane 1: Spectra Multicolor Broad Range Protein Ladder, 2: wild-type invasin, 3: RGD844, 4: RGD, 5: 1R6-1. (B) ELISA comparing binding of wild-type invasin (●) and the 1R6-1 clone (■) with the RGD (▲) and RGD844 (▼) variants to $\alpha5\beta1$ integrin. (C) Table detailing the changes in binding to $\alpha5\beta1$ integrin as changes in the relative EC_{50}. (D) ELISA comparing binding of wild-type (●) invasin and the 1R6-1 (■) clone with the RGD (▲) and RGD844 (▼) variants to $\alpha3\beta1$.

RGD844 variant exhibits improved affinity as MBP-D1D5 construct

Binding of soluble invasin to both integrin and eukaryotic cells is enhanced by inclusion of the D2 domain, responsible for increased avidity through self-association (Figure 2.1C)(62, 96, 97). Therefore, we introduced the substitutions identified in our optimized invasin variant RGD844 (F844Y, G909R, and S910G) into an MBP-invasin fusion protein encompassing all five extracellular invasin domains (MBP-D1D5) in vector pTAK035. The purified proteins (Figure 2.9A) were analyzed by ELISA with soluble integrin as described above (Figure 2.9B). As expected, invasin variant RGD844 in this construct exhibited a decreased EC_{50} compared to the monomeric MBP-D4D5 version (95% confidence intervals for EC_{50} shifts (1.84-3.05), relative to wild-type). Also, the optimized invasin in the MBP-D4D5 construct demonstrated a lower EC_{50} than the wild type sequence in MBP-D4D5, showing the beneficial substitutions outweigh the effect of incorporating the D2 domain (95% confidence interval for EC_{50} shift (3.32-5.67), relative to wild-type).
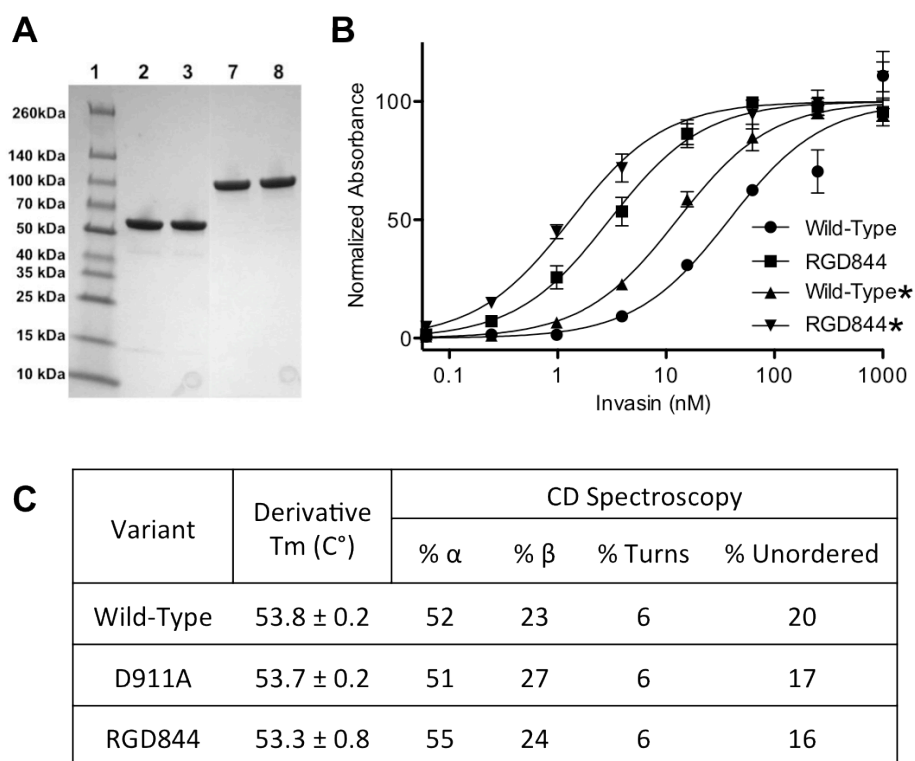
Figure 2.9: Comparison of wild-type and RGD844 invasin binding to integrin as MBP-D1D5 and MBP-D4D5 constructs. (A) Non-reducing SDS-PAGE depicts purified protein of the expected molecular weights (62 and 93 kDa). Lane 1: Spectra Multicolor Broad Range Protein Ladder, 2: wild-type (MBP-D4D5), 3: RGD844 (MBP-D4D5), 7: wild-type (MBP-D1D5), 8: RGD844 (MBP-D1D5). (B) ELISA comparison of wild-type (●, ▲) and RGD844 (■, ▼) invasin binding to α5β1 integrin as MBP-D4D5 and *MBP-D1D5 constructs. (C) Structural characterization of three variants (MBP-D1D5 format) with notable binding differences for integrin: wild-type, D911A, and RGD844 by circular dichroism and thermal melting temperature.

To determine whether the key amino acid substitutions affect invasin structure, we measured the apparent thermal unfolding transition temperature (Tm) and circular dichroism (CD) spectra using the MBP-D1D5 constructs. The Tm for the wild type, D911A, and RGD844 variants, determined with a high-throughput fluorescent assay, were all within error, near 54°C (Figure 2.9B). The secondary structure of these variants, from CD spectra, also exhibited similar features between variants (51-55% alpha helix,

23-37% beta sheets, 6% turns, and 16-20% unordered), suggesting an absence of major structural changes (Figure 2.9C).

The *Y. psuedotuberculosis* invasin protein has received considerable attention and has been proposed as a targeting molecule for oral vaccines (57, 61, 62, 64, 68, 79, 81, 96). However, its affinity for the α5β1 integrin present on intestinal immune M cells is only moderate (K_d ~5 nM) and previous studies have shown that increased affinity of M cell ligands translates to enhanced immune responses for oral vaccines (42, 93). Using alanine scanning mutagenesis, we identified four previously unidentified surface residues involved in integrin binding (Y860A, Y878A, R883A, Y885A). Next, using directed evolution and four site-directed libraries, we show for the first time, that the presence of an RGD epitope surrounding the essential D911 residue, in conjunction with an F844Y substitution, enhances the affinity of invasin nine-fold for the α5β1 integrin and Caco-2 cell invasivity without compromising specificity. This engineered invasin molecule, RGD844, may be valuable to oral vaccines as both an M cell ligand and a natural adjuvant (78, 103).

Invasin RGD sequence is not observed in *Yersinia* strains

The template invasin for our library comes from the *Y. psuedotuberculosis* bacteria, as this is the best-characterized variant. Comparing among the available sequences, we noticed that two of the three beneficial amino acid substitutions naturally occur in other invasin strains (Table 2.3). Both F844Y and G909R are present in the invasin expressed by *Y. enterocolitica*, indicating that the substitutions are well-tolerated and that our in vitro evolution process may have mimicked natural evolution.

Nevertheless, since the presence of the RGD motif dramatically enhances invasin affinity for the α5β1 integrin and thus would be expected to confer an evolutionary advantage, it is interesting that it is not present in *Y. pseudotuberculosis*. Notably, invasin is not the only adhesion employed by *Yersinia* species; it assists the YadA adhesion and thus would be expected to be more tolerant to sequence drift (104). However, introduction of the RGD motif does require a series of DNA base pairs changes, which may need to occur in a specific sequence. Out of 25 sequenced clones from library 4, only two clones had amino acids other than serine or glycine position 910. All 12 clones containing the S910G change were accompanied by G909R, although clones with G909R did not require S910G (3/25 observed). This suggests that *Y. psuedotuberculosis* invasin can only acquire the S910G substitution if it has already acquired a G909R substitution. Furthermore, the codon change from serine to glycine requires changing two nucleotides, one of which is a T->G substitution, which are believed to occur much less frequently than other mutations in bacteria (105).

| 845-860 Region/ Library 1 | | | | | | | | | |
| KHT | VAK | NTT | WMC | KHT | MAW | RSC | KHT | KHT | GAW |
844	847	858	859	860	861	862	863	864	865

	KHT 844	VAK 847	NTT 858	WMC 859	KHT 860	MAW 861	RSC 862	KHT 863	KHT 864	GAW 865
Y. psuedotuberculosis	F	N	I	T	Y	Q	T	Y	S	E
Y. entericolitica	Y	S	I	A	Y	K	T	Y	S	T
Y. pestis	F	N	I	T	Y	Q	T	Y	S	E
RGD844 Variant	**Y**	N	I	T	Y	Q	T	Y	S	E

	911 Region/Library 4					
	NWW 908	NNC 909	NNC 910	KHT 911	NNS 912	KMT 913
Y. psuedotuberculosis	Q	G	S	D	M	S
Y. entericolitica	Q	R	T	D	F	T
Y. pestis	Q	G	S	D	M	S
RGD844 Variant	Q	**R**	**G**	D	M	S

Table 2.3: Invasin amino acid comparison between *Yersinia* strains

RGD844 combines fibronectin and invasin binding functions

When the crystal structure of invasin was first revealed, the integrin D4D5 binding domains were compared to the endogenous human α5β1 integrin ligand, fibronectin (70, 96). Fibronectin type III repeats 9-10 interact with α3β1, α4β1, α5β1, α8β1, αVβ1. αVβ3, and αVβ6 integrins (106), while invasin binds α3β1, α4β1, and α5β1, suggesting functional if not structural homology (69). Moreover, invasin and fibronectin bind the same region of α5β1, based on competitive binding and integrin mutational studies (70, 73). Notably, in the absence of sequence homology, the structural comparison identified a remarkable structural similarity between fibronection's RGD epitope and synergy site and invasin's essential D911 and key D811/ R883 residues, respectively (Figure 2.10). The D811 position also seems to behave in a manner suggesting it lies in synergy site, like that observed in fibronectin type III repeats 9 and

10 (67, 70). In spite of this structural homology, fibronectin binds with a K_d over two orders of magnitude lower (73) and is a poor facilitator of inducing internalization of particulates (62, 98).

Invasin D1-D5

Fibronectin III 7-10

D911 and RGD Sites
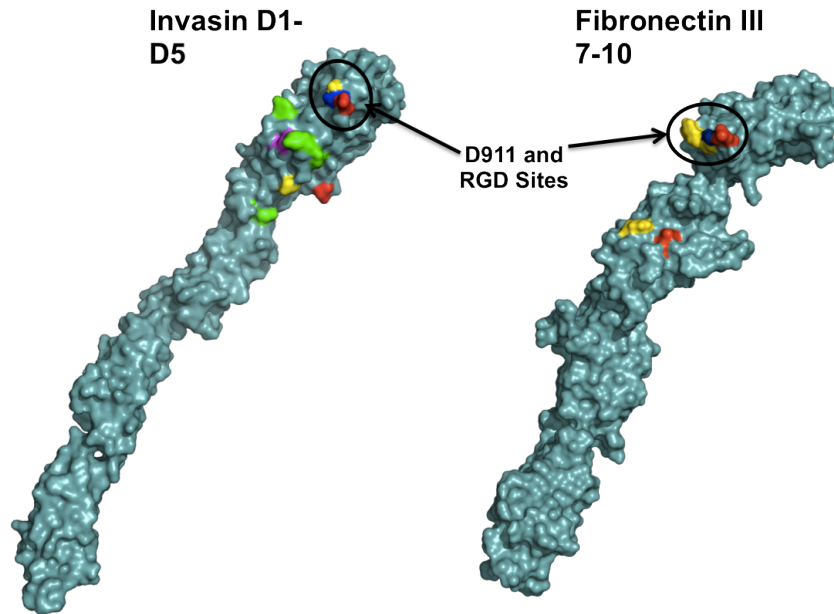
Figure 2.10: Structural comparison of wild-type invasin (D1-D5) with fibronectin III repeats 7-10. The critical aspartic acid residues (D911 in invasin and the RGD motif for fibronectin) and synergy sites are highlighted for comparison with the color code Asp (red), Arg(yellow), Gly(blue), Tyr(green), invasin F844Y (purple).

Considerable work with the fibronectin with α5β1 integrin interaction has revealed the complexity and difficulties in studying α5β1 binding (75, 107, 108). These difficulties lie in the fact that α5β1 is a membrane bound protein, difficult to express and purify, and both molecules convert between multiple physical states. Since the initial invasin protein structure/function work by Isberg and others, it has been shown that α5β1 integrin is a highly dynamic heterodimeric molecule that exists in at least three different conformations: relaxed, extended, and tensioned (75). The switch of an integrin complex from its relaxed to extended state is necessary for ligand recognition and integrin

clustering (109), and is linked to the enhanced cellular uptake of particulates coated with α5β1 ligands (62).

From the current work and others, it is apparent that a broad surface of invasin in the D4-D5 domains interacts with α5β1 integrin. Comparisons between the D911 of invasin with the RGD epitope found in fibronectin are further supported by our data (70, 96). The RGD epitope, especially the aspartic acid residue(110), of fibronectin is believed to primarily engage the β1 subunit of the integrin receptor, while the synergy site is thought to engage the α5 subunit (75). When we compared binding of our RGD invasin variant to the α5β1 and α3β1 integrins, we observed increased binding to both receptors compared to wild-type invasin, suggesting the RGD substitution enhances binding to the shared b1 subunit. In contrast, the additional F844Y substitution located near invasin's proposed synergy site (R883), exhibits increases affinity towards α5β1, but not α3β1, suggesting this change affects interactions with the α5 subunit.

The engagement of the fibronectin synergy site in the tensioned state of α5β1 has been shown to provide up to 90% of the adhesion strength in cell binding assays (75). We find invasin's synergy site to play a role in role in integrin binding, but not significantly, compared to D911, in our bacterial flow cytometric analysis. This suggests that the recombinant α5β1 in our work behaves more similar to the extended state, rather than either the relaxed or tensioned states. The tensioning of α5β1 is easily understood in the context of mechanical stress-strain interactions between mammalian cells and their extracellular matrix (ECM)(111-114). From an evolutionary standpoint, the incredible structural similarity of the synergy site of invasin to that of fibronectin might suggest that

51

pathogens expressing invasin also undergo a stress-strain relationship with mammalian cells upon infection. It is hard to imagine systemically infected bacterial cells partaking in shear forces similar to those involved with the ECM. However, invasin expressing pathogens gain systemic entry through M cells via the luminal surface of the GI tract (58). Also, *Y. pestis* encodes a disrupted invasin gene and does not invade its host as an enteropathogen, suggesting invasin's primary role is along the GI tract (115). It is believed that the peristaltic motion of the GI tract results in tissue stresses and strains within the small intestine (116-118). These mechanical forces may have provided the selective pressure to produce the unique structure similarity between invasin and fibronectin.

CONCLUSIONS

The invasin protein from *Y. psuedotuberculosis* has been studied in great depth and has been lauded as a potential targeting molecule for oral vaccines (57, 61, 62, 64, 68, 79, 81, 96). Here we show, for the first time, that the presence of an RGD epitope along with another mutation further enhances the affinity of invasin for α5β1 integrin. By incorporating three substitutions in the D4-D5 region, we decreased the EC_{50} value by nine-fold, measured by ELISA against α5β1 integrin. This affinity maturation may aid vaccines systems beyond simple targeting, by also potentially increasing the adjuvanticity by signaling intracellular pathways and increasing the number of M cells, mediated through β1 integrins (78, 103). In this report, we furthered the understanding of how invasin engages α5β1 integrin and applied this knowledge to engineer invasin for higher

affinity, which may yield improvements in oral vaccines using invasin as a targeting agent.

MATERIALS AND METHODS

Display of invasin on *E. coli* surface

To facilitate rapid screening and analysis of invasion variants, a vector was constructed in which the intact invasion gene is presented on *E. coli* outer membrane, where it is accessible for ligand (integrin or anti-invasin antibody) binding and able to mediate invasion of cells expressing the α5β1 integrin. The full-length invasin gene was PCR amplified from plasmid pRI203 (61) using primers TAK43 and TAK45 (Table 2.4), digested with restriction enzymes XbaI and SphI (NEB) and ligated into similarly digested pBAD30 vector (119) to create plasmid pTAK020 (Figure 2.1B). Individual alanine substitutions at positions D881, Y860, Y863, Y878, R883, Y885, D911 and Y976 were introduced using a modified QuickChange procedure. Off-set complementary primers annealing to pTAK020 and introducing a single alanine substitution were used in a PCR reaction with high fidelity polymerase PFU Ultra II (Agilent). The PCR product was digested with DpnI and transformed into *E. coli* MC1061 cells. DNA sequencing confirmed the presence of only the desired mutation.

Primer Name	Nucleotide Sequence
TAK43	taactgacgatctagaactttaagaaggagatataccatgatggttttccagcc
TAK45	tacgatgtctaatgtatgcatgctcaattattcattatattgacagcgcacag
TAK46	agctatcgagctcgaactcattcacattgagcgtc
TAK47	cgtcattataccatggctagttaatcattatattgacagcgcacagag
TAK139(Library 1)	gccgtcacagccacwtcadmadmgsywtkadmgkwaancgtcacctgaccctgatcgttaaccgatacmtbgggtgtadmtgacgacgaccactc
TAK140(Library 2)	cgccatcgtatatccacykstkcggadmaankykakaadmaanadmadmacttgggaattttttacttttcgc
TAK141(Library 3)	gcgtttttaaagatcgttttcggaangccsnnsnnsnnsnngaaattttgcccgttaacc
TAK142(Library 4)	gcacgtgaggattcaagaaccgcakmsnnadmgnngnnwwngcattgtctgctggcctcgag

Table 2.4: Primer sequences

Fluorescent labeling of soluble α5β1 integrin

In order to monitor the ability of cells displaying invasin variants to bind the α5β1 integrin ligand in a high-throughput manner, we employed a FACS-based assay with fluorescently labeled integrin. To label the integrin, Alexa Fluor 647 (Invitrogen A20006) was dissolved in acetonitrile at 1mg/ml, aliquoted in 50ul fractions, dried and stored at -20°C. A 50 ug aliquot of α5β1 integrin (R&D Systems, Inc 3230-A5 Lot OOJ2510121), was adjusted to 100 mM sodium bicarbonate and combined with 20 ul dye solution (prepared from 50 ug Alexa Fluor 647 dissolved in 5 ul of dimethylformamide plus 45 ul of 1 M sodium bicarbonate). The reaction was allowed to proceed for 1.5 hours with rotation at room temperature, after which the solution was dialyzed against integrin buffer (50 mM HEPES, 200 mM NaCl, 2 mM MnCl$_2$ pH 7.5) using a 20K MWCO dialysis cassette (Pierce 66005) to remove unreacted dye. To prevent photobleaching, all steps proceeded in the dark.

Analysis of single invasin variants via flow cytometry

Bacterial strains with plasmids encoding full-length invasin variants for surface display were grown overnight in LB with ampicillin (150 ug/ml) at 37°C, then diluted into fresh media at an OD_{600} =0.05. Cells were allowed to grow for two hours (OD_{600} ~0.4-0.8) at 37°C, at which point arabinose was added to 0.2% and expression proceeded for an additional two hours. Samples for FACS analysis (1 x 10^8 cells) were pelleted, media removed and cells resuspended in 25 ul integrin buffer (50 mM HEPES, 200 mM NaCl 2 mM $MnCl_2$ pH 7.5) with 4% BSA. Next, 25 ul of a 200 nM Alexa Fluor labeled α5β1 solution in integrin buffer, was added to each cell sample and allowed to equilibrate for 30 minutes at room temperature with periodic gentle agitation, placed on ice for 5-15 minutes and centrifuged as above. The cell pellets were stored on ice until just prior to flow cytometric analysis when they were resuspended in 1 ml of integrin buffer and diluted 1:10. For labeling with the 3A2 anti-invasin antibody (65), cells were resuspended in 100ul of PBS with 1ul of a 1mg/ml stock antibody solution after the initial harvest. After 30 minutes equilibration, cells were pelleted and incubated in 100 ul PBS with 1 ul of Cy5-labeled goat anti-mouse IgG (H+L) (Invitrogen A10524) for an additional 30 minutes, prior to a final resuspension in PBS prior to analysis. Cells expressing alanine variants were scanned on a FACSCalibur (Becton-Dickinson), while cells expressing variants selected from libraries were analyzed on an LSRFortessa (Becton-Dickinson). Data was analyzed using FlowJo software, in which a size gate including ~90% of the collected events was determined and the median fluorescence intensity (MFI) within this gate reported.

Analysis of invasin variant activity by Caco-2 invasion

The Caco-2 invasion assays were performed similarly to those described by Critchley-Thorne et al. (81). Briefly, BL21(DE3) cells were co-transformed with two plasmids: (1) pTAK020 encoding full-length invasin variants for surface-display and (2) a pET28 plasmid encoding green fluorescent protein (GFP) as a reporter molecule to track bacterial internalization. Bacterial cultures were grown as for FACS analysis, but diluted to an OD_{600}=0.1 with kanamycin (50 ug/ml) and 1 mM IPTG to support the pET28 plasmid and a 4-hour expression period, induced upon dilution. Simultaneously, Caco-2 cells (P23-P33, 5-10 passages after receipt from ATCC) were seeded at a density of 5 x 10^4/cm^2 in complete media [DMEM (Mediatech, Inc 15-013) supplemented with MEM nonessential amino acids (Mediatech, Inc 25-025-CL), penicillin/streptomycin (Gibco 15140-122), GlutaMAX (Gibco 35050-061), and 10% serum (Gibco 26140-079)] and placed in a CO_2 incubator (5%) at 37C overnight.

Immediately prior to infection, the Caco-2 cells were washed twice with DMEM without supplements, then provided complete infection media without penicillin/streptomycin or serum, but with ampicillin, kanamycin, arabinose, and IPTG at the concentrations listed above. Bacteria were added to the cultures at a multiplicity of infection of 70, based on seeded Caco-2 cell numbers, using the relationship 1 OD_{600}=1 x 10^9 cells/ml and allowed to incubate for two hours at 5% CO_2 and 37°C. At this point, the Caco-2 monolayer was washed again and placed in complete infection media without penicillin/streptomycin and with gentamicin (20 ug/ml) to kill extracellular bacteria. The next day, the Caco-2 cells were trypsinized, washed in PBS and stored on ice in PBS +

1%FBS prior to scanning with an LSRFortessa (Becton-Dickinson) and analysis as above. The populations clearly divided into a bimodal distribution. The percentage of the higher fluorescence population, compared to the size-gated total, is reported as the percent of Caco-2 cells with high fluorescence, indicating the presence of internalized GFP-expressing bacteria.

Generation of site-directed libraries

Four libraries were created each with a theoretical library size of ≤3-6x10^6 in order to allow for complete experimental sampling of the library. This was achieved by randomizing a small number of residues in each library (ten or fewer) and by using a soft randomization procedure to preserve physicochemical properties, which may be important for folding or stability. For example, F884 has a hydrophobic side chains and faces towards the center of the D4-D5 domains, likely contributing to hydrophobic interactions. This residue was mutated using the degenerate codon NTT that encodes hydrophobic residues (F, I, L V). Libraries affecting fewer residues utilized degenerate codons that sampled larger number of amino acids, such as the NNS codon that samples all natural amino acids. All libraries were designed to allow for sampling of the wild-type sequence of invasin, using the primers shown in Table 2.4. Library 1, with a theoretical library size of 3.98x10^6, was created using the following degenerate codons corresponding to their c-terminal amino acids: 844(KHT), 847(VAK), 858(NTT), 859(WMC), 860(KHT), 861(MAW), 862(RSC), 863(KHT), 864(KHT), and 865(GAW). Library 2, with a theoretical library size of 5.31x10^6, was created using the following degenerate codons: 878(KHT), 870(KHT), 880(NTT), 881(KHT), 882(TMT),

883(MRM), 884(NTT), 885(KHT), 887(MAS), and 888(MRG). Library 3, with a theoretical library size of 4.19×10^6, was created using the following degenerate codons: 809(NNS), 810(NNS), 811(NNS), 812(NNS), and 814(NTT). Library 4, with a theoretical library size of 3.15×10^6, was created using the following degenerate codons: 908(NWW), 909(NNC), 910(NNC), 911(KHT), 912(NNS), and 913(KMT). The number of actual transformants was at least 10-fold greater than the theoretical size for each library.

Libraries were generated using a modification of the protocol described by Sidhu and Weiss (120). Briefly, we created inactive invasin templates by introducing stop codons or frame shift mutations into the regions targeted for mutagenesis. The templates were transformed into *E. coli* strain CJ236 and infected with M13KO7 helper phage in media with uridine to isolate uracil-containing single-stranded plasmid DNA (dU-ssDNA). Four separate libraries were created with mutagenic primers (Supplementary Figure 1). The primers were added to dU-ssDNA templates with T4 ligase and T7 polymerase to generate a double-stranded heteroduplex with a complementary strand containing the mutagenic primer and dTTP. Libraries were generated by transforming heteroduplex DNA into electrocompetent MC1061 cells. In all cases, the number of transformants was 10-fold greater than their predicted library sizes of $3\text{-}6 \times 10^6$. Colonies were scraped from plates, the cell concentration was measured by absorbance at 600 nm and recorded, adjusted to 15% glycerol and frozen at -80°C.

Caco-2 based selection of invasin variants

In order to select for invasin variants able to both target and invade M cells, we employed a dual selection approach using bacterial cells with surface-displayed invasin: first, a cell-based invasion protocol similar to that described above, followed by a FACS-based selection employing fluorescent α5β1 integrin. Each library underwent two rounds of Caco-2 cell panning, followed by 2-4 rounds of FACS based selection with fluorescent integrin, using sequence convergence based on analysis of 6-10 clones per round to assess the enrichment process.

For the two rounds of Caco-2 based cell panning, the first recovers bacterial cells adhering or internalized by Caco-2 cells, while the more stringent second round uses gentamycin to kill extracellular bacteria, and only propagate clones which have been internalized. Caco-2 cells (P23-P33) were seeded into two T-75 flasks using the complete media described before, one at 5×10^4 cells/cm^2 and one at 1×10^4 cells/cm^2, and allowed to adhere overnight. Bacterial cultures were grown as above, using a 100 ul aliquot of frozen library cells to seed a starter culture, followed by growth and expression in a 20 ml culture (101). The Caco-2 cells seeded at 5×10^4 cells/cm^2 were washed and prepared as described earlier, with complete media containing ampicillin and arabinose, before 3×10^9 bacteria (MOI ~800) were added for a two hour incubation at 5% CO_2, 37°C. Next, the Caco-2 cells were washed several times with DMEM base media to remove extracellular bacteria. To lyse Caco-2 cells and recover internalized bacteria, ~6 ml of LB with ampicillin (150 ug/ml) and 1% Triton X100 was added to the flask for 10 minutes. The flasks were then scraped and the contents transferred to microfuge tubes, pelleted

and resuspended to remove Triton X-100, and transferred to 20 ml of TB with ampicillin and 2% glucose for overnight growth at 37°C.

The following day, 1×10^9 bacterial cells from the overnight culture were inoculated into 20 ml of fresh LB with ampicillin, for expression and infection as above using the other T-75 flask seeded at 1×10^4 cells/cm^2 two days prior. After 2 hours of infection at an MOI ~800, the flask of infected Caco-2 cells, were washed with DMEM base, followed by DMEM supplemented with MEM nonessential amino acids, GlutaMAX, 10% serum, ampicillin, arabinose, and gentamycin for overnight incubation. Bacterial cells were recovered as described above and fractions (<1%) of the recovered cells were plated for sequence analysis. Overnight cultures were either subcultured or frozen for subsequent FAC-based selection rounds.

FACS-based selection of invasin variants

After Caco-2 cell panning, libraries were grown and expressed as previously described for Caco-2 panning. After expression, cells (~1×10^8) were labeled with fluorescent α5β1 (100nM-250nM) as described earlier and stored on ice. The concentration of the label was reduced during subsequent rounds of sorting. Cells were diluted in integrin buffer such that they could be sorted at rates between 1,000-5,000 events per second. The forward scatter and side-scatter thresholds were adjusted to remove debris in the FACS buffer, which improved the electronic abort rate. A size gate was set to encompass ~90% of events. Initial sorting rounds were less stringent and sorted 3-5% of the most fluorescent events, while later sorting rounds became more restrictive, collecting only the top 0.5-1%. Sorted cells were collected in 15 ml conical

tubes holding ~2 ml of cold LB with ampicillin and glucose. Fractions of collected cells were plated after each round to analyze cell viability and sequence convergence. The remaining collected cells were grown overnight for subsequent rounds of sorting and freezing of aliquots from each round.

Expression & purification of soluble invasin variants

To compare the integrin binding abilities of different invasin variants, a soluble version of invasin consisting of the minimal receptor binding domains (D4-D5, residues 795-986) was expressed in the *E. coli* cytoplasm. To enhance expression levels and solubility, these domains are expressed as a c-terminal MBP fusion, as performed previously (68). To generate this construct, the D1-D5 domains were first amplified from plasmid pRI203 using primers TAK46 and 47 and cloned into vector pMAL-c5x (NEB) using SacI/NcoI restriction sites to generate plasmid pTAK035 (MBP-D1D5)(Figure 2.1B). Domains D1-D3 were deleted using PCR-based plasmid mutagenesis, as above, to create plasmid pTAK039 (MBP-D4D5)(Figure 2.1B). Invasin variants selected from mutagenic libraries were either sub-cloned into pMAL-c5x or generated by site-directed mutagenesis of pTAK039.

The pTAK035 plasmid was transformed into *E. coli* strain Origami B to support formation of the lone di-sulfide bond in the D4-D5 region during cytoplasmic expression (EMD Chemicals). To further enhance expression levels, the 17 kilodalton (Skp) chaperone was co-expressed from a compatible expression vector, pAR3-Skp without its native periplasmic leader sequence (121). Starter cultures grown in LB with ampicillin (150 ug/ml), chloramphenicol (34 ug/ml), kanamycin (15 ug/ml), tetracycline (12.5

ug/ml), 0.2% glucose were sub-cultured into 250 ml of Terrific Broth (TB) containing the same additives. After ~16 hours growth at 37°C, the cells were harvested and resuspended in fresh TB with antibiotics, but without glucose, and shaken at 25°C and 225 RPM. After 30 minutes, arabinose was added to a final concentration of 0.2%, after another 30 minutes, IPTG was adjusted to 1 mM, and expression continued for ~4-5 hours. Cells were then harvested and frozen at -80°C, resuspended and lysed via French Press with a standard cell (Thermo Electron). To minimize degradation, complete protease inhibitor tablets (Roche Diagnostics) were immediately added and the cell lysate clarified via centrifugation at 4°C for 45-60 minutes at 20,000 RPM and syringe filtered through 45 μm PVDF filter (Millipore). The protein were purified using an MBPTrap HP (5 ml) column on an ÄKTA FPLC system followed by size exclusion chromatography using a HiLoad 16/600 Superdex 200pg column (GE Healthcare). Protein purity was analyzed by non-reducing SDS-PAGE, in which samples were heated in loading buffer without DTT and run on a Mini-PROTEAN electrophoresis cell (Bio-Rad) using a 4-15% TGX Gel (Bio-Rad).

ELISA analysis integrin binding by soluble MBP-INV

ELISAs were used to assess the relative affinity of different invasin variants for relevant integrins. ELISA plates (96 well high-binding plates; Costar) were coated with recombinant, soluble versions of the extracellular α5β1 or α3β1 integrin domains (R&D systems 2840-A3-050 and 3230-A5-050) in PBS at ~3 ug/ml overnight at 4°C. Coated plates were blocked with 5% milk in PBS and washed with binding buffer (50 mM HEPES, 200 nM NaCl, 2 mM $MnCl_2$, 0.05% Tween20). Purified MBP-invasin variants

were added to the plates in a 1:3 dilution scheme from 1000 nM in blocking buffer (50 mM HEPES, 200 nM NaCl, 2 mM $MnCl_2$, 1% milk) and allowed to equilibrate for 1.5 hours. The addition of 2 mM $MnCl_2$ was found to enhance invasin-integrin binding (data not shown)(67). Plates were washed again, followed by anti-MBP antibody-HRP conjugate (New England BioLabs E8038S) at a 1:3333 dilution in blocking buffer for 1 hour. All incubation steps were performed at room temperature with shaking. The plates were washed a final time prior to the addition of TMB substrate (Pierce 34021), quenching with 1N HCL and the absorbance measured at 450 nm. All statistical analysis was performed using Prism 5 (GraphPad Software, Inc.). ELISA data was fit using a 3-parameter nonlinear curve fit with the bottom parameter shared between curves.

Melting Temperature and Circular Dichroism Measurements

The melting temperature of purified protein was assessed using protein solutions (3.2 mg/ml) and Sypro Orange (1:6,000 dilution). The solution temperature was gradually increased (1 degree C per minute) and fluorescence was recorded using a ABI 7900HT Fast Real-Time PCR System. As the protein denatures, the Sypro Orange is able to access hydrophobic regions of the protein, resulting in fluorescence activation. The inflection point of temperature, fluorescence plots is reported as the derivative Tm. Circular Dichroism (CD) measurements were made using a Jasco-J815 CD Spectrometer from 260 nm to 185 nm (1 nm increments) in a 5 mM phosphate buffer.

ACKNOWLEDGEMENTS

Chapter 3: Polymeric Antigen Delivery System Formulation and Characterization

INTRODUCTION

Oral administration is the preferred route for any therapeutic agent. Beyond simple administration benefits, vaccination via the oral route can lead to the induction of mucosal immune responses, such as secretory IgA (122). Antigen specific IgA in mucosal compartments can prevent pathogens from gaining entry into systemic circulation. Unfortunately, oral delivery of subunit vaccines is extremely challenging due to the proteolytic environment of the GI tract and the small number of intestinal cells capable of transporting antigenic material to lymphoid tissue in the lamina propria (9, 88). The cells that are responsible for transporting particulate matter for immune processing are termed M cells. These M cells have become the primary target for oral vaccine delivery systems (9, 88, 90).

Researchers have improved immune responses to oral subunit vaccines by targeting M cells using a variety of targeting molecules (40, 42, 71, 92, 93). The methods used to target M cells have relied on identifying ligand-receptor pairs that preferentially target M cells, including the NKM 16-2-4 antibody, CKS9 peptide, UEA-1 lectin, and cholera toxin B subunit, with varying effects on the ultimate immune responses (91). For instance, while UEA-1 effectively targets M cells in the mouse model, in humans, goblet cells also express the targeted receptor, reducing the specificity of that molecule (123). Several studies have demonstrated protein engineering techniques that yielded ligands targeting M cells (91, 93). Nochi et al. generated a rat IgG2c that specifically recognizes

mouse M cells and when utilized in an oral vaccine formulation results in a protective immune response. However, it was determined that the receptor recognized is α(1,2) fucose, which is also present on mouse goblet cells (123). The specificity of this antibody to murine M cells over goblet cells may be due to glycosylation differences between α(1,2) fucose on these two cell types, a difference which may not be preserved in humans. Last, a phage displayed peptide library was used to identify a nonameric peptide binding a human in vitro M cell model (124). While this was identified with human cells and targeting validated in the rat intestine, peptides typically exhibit weak affinity due to their small size and may not be as useful.

Given the expression variations across species, developing vaccines using ligands binding known markers on the M cell surface of multiple species (including humans), such as α5β1 integrin would be advantageous (32, 57, 59). Using such ligands may show better correlations between preclinical and clinical studies. Reports targeting α5β1 integrin using RGD peptides improved immune responses, compared to particles without ligand (42). The invasin ligand discussed in depth in Chapter Two is another potential ligand for targeted oral vaccines.

In addition to its adhesion activities, invasin also possesses adjuvant activity, rendering it more attractive as targeting ligand for oral vaccine formulations (74, 90). Invasin can directly stimulate T cells when immobilized on a plate (76). Incubation of HeLa cells with 1μm polystyrene beads coated with an ovalbumin-invasin fusion protein resulted in increased IL-8 secretion, which is an innate immune system chemoattractant (80). After intraperitoneal injection of the same beads, systemic increases in CD4 and

CD8 T cells and splenocyte production of IL-4 and INF-γ was observed (80). When *E. coli* co-expressing invasin, ovalbumin, and listeriolysin O were orally administered to mice prior to challenge with an ovalbumin-expressing tumor, final tumor volumes were ~25% the size of unvaccinated mice, indicating the presence of a strong anti-ovalbumin immune response (81).

In order to facilitate efficient oral vaccination, polymeric microparticles were designed to entrap antigen and be decorated with the invasin targeting protein. These microparticles should transit through the stomach and small intestine, upon which they will encounter rare M cells. The targeting protein, invasin, should then specifically engage α5β1 integrins on the apical M cell surface and trigger phagocytosis. The microparticles should then be transcytosed through the M cells, being released in Peyer's patches where they would encounter lymphocytes that initiate immune responses directed against the entrapped antigen. This mechanism is shown in the schematic below (Figure 3.1).
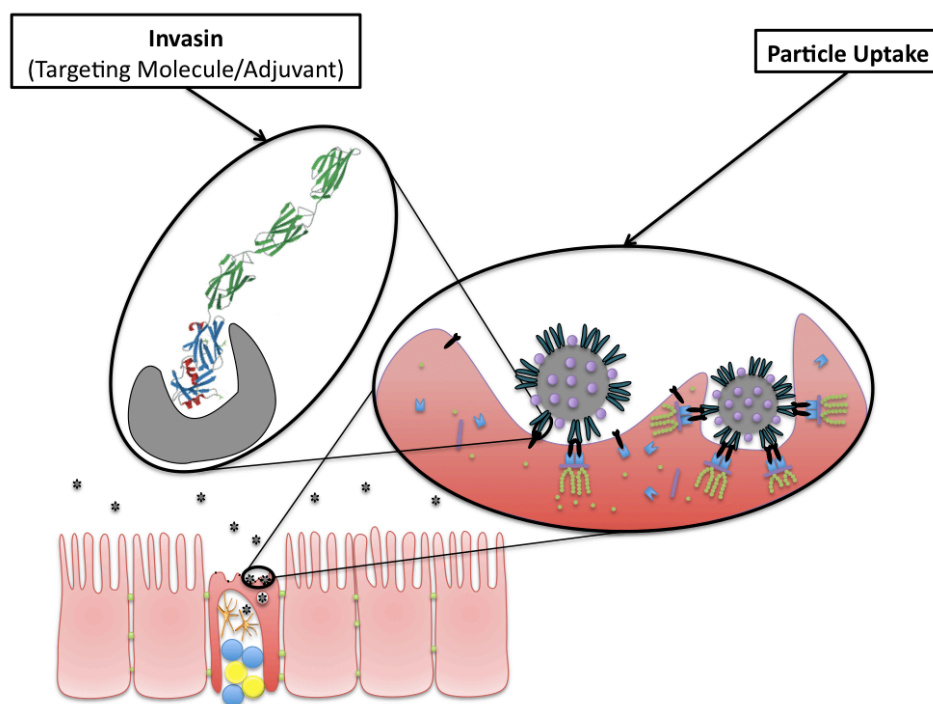
Figure 3.1: M cell targeting and particle uptake schematic

Poly(lactic-co-gycolic acid) (PLGA) is a biodegradable and biocompatible polymer that can be used to entrap water soluble molecules by forming a water-in-oil-in-water emulsion, followed by solvent evaporation (Figure 3.2). PLGA particles have been used in numerous oral vaccine studies, providing a good base to build upon for testing the benefits of targeting M cells using the invasin variants generated and discussed in Chapter Two (9, 87). During particle synthesis, soluble antigens can be loaded by incorporating them in the inner aqueous phase. This inner aqueous phase is emulsified with an organic phase, which is used to solubilize the PLGA polymer. This primary emulsion is then added to a secondary aqueous phase and emulsified again. This double emulsion has an aqueous continuous phase, suspending droplets of the organic solvent. The organic solvent droplets contain smaller droplets of the inner aqueous phase. This

68

double emulsion is allowed to stir for several hours, causing evaporation of the organic phase. This solvent evaporation step precipitates the PLGA polymer, generating particles entrapping the protein in the inner aqueous phase.
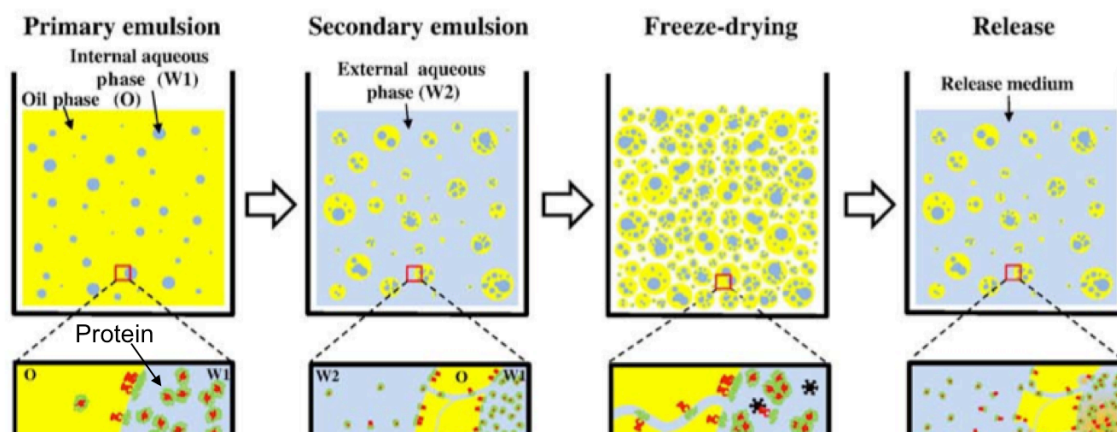
Figure 3.2: Water-In-Oil-In-Water emulsion process for encapsulation and release of proteins (modified and reproduced with permission)(24) Primary emulsion: water phase with solubilized protein is dispersed in oil phase with solubilized PLGA. Some protein is denatured at the interface, where hydrophic regions lie in the oil phase and hydrophilic regions are maintained in the water phase. Secondary emulsion: droplets from the primary emulsion are dispsersed in a second water phase. Some protein is leaked from the inner water phase through channels formed during emulsification. Freeze drying: during freezing and lyophilization, proteins can become denatured and aggregated. Release: once rehydrated, protein diffuses through pores in the PLGA particles. Over time the PLGA is hydrolyzed, causing bulk erosion, which expands the porosity of the particles.

RESULTS AND DISCUSSION

Particle Morphology Effects Due to Antigen/Excipient Loading

The designed oral vaccine delivery system relies on encapsulation of antigen in the PLGA microparticles by incorporating antigen, ovalbumin, as a soluble molecule within the inner water phase of the double emulsion. PLGA microparticles were initially synthesized using a previously described protocol to entrap siRNA in the inner water

69

phase (7). The protocol was modified by substituting a different emulsifying surfactant (PEMA), shown to increase the amount of protein able to be coupled to the particle surface (detailed discussion in the following section). Upon incorporating ovalbumin within the inner aqueous phase, we observed changes in particle morphology. At low ovalbumin concentrations, there was increased size and polydispersity. At higher concentrations, spherical morphology was lost (Figure 3.3).
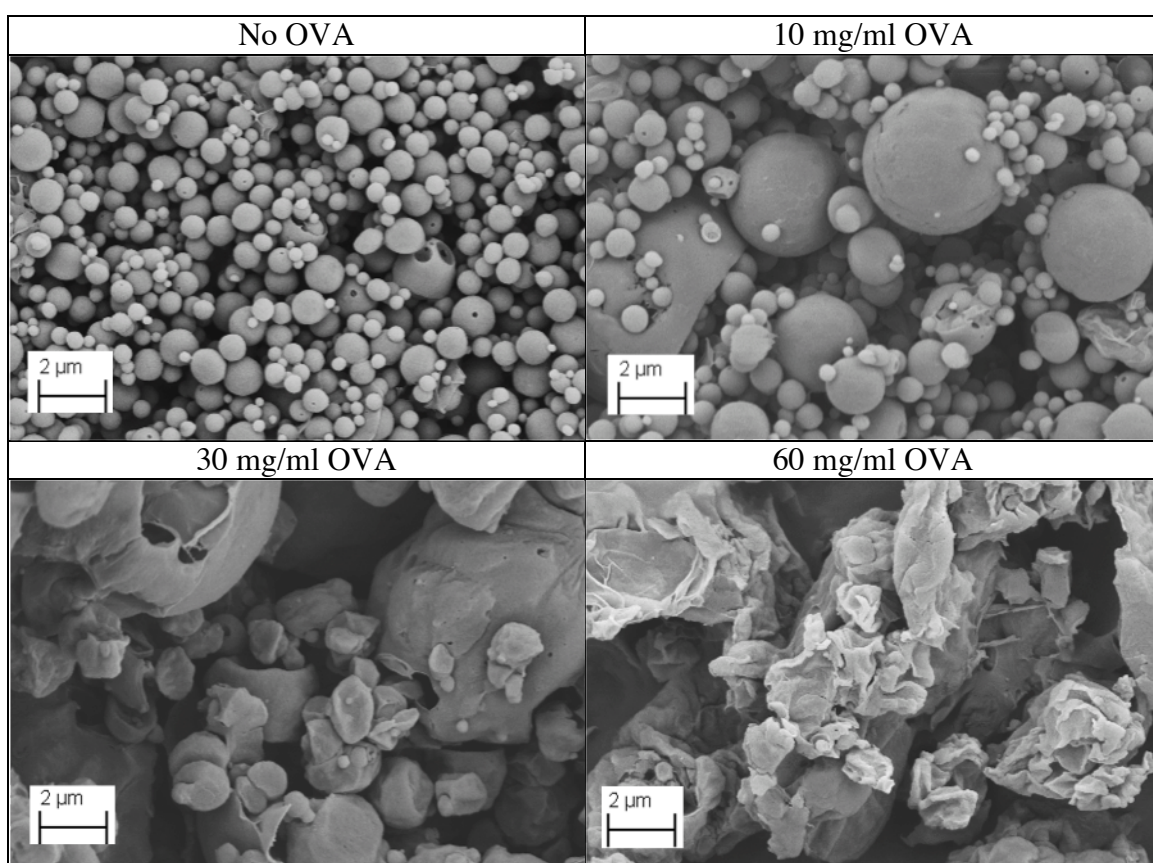
Figure 3.3: SEM images of particle morphology effects due to antigen loading. Lyophilized PLGA preparations were sputter coated with Pt/PD and imaged via SEM. As the concentration of ovalbumin is increased in the inner water phase, polydispersity is increase and the spherical morphology is lost.

While ovalbumin could be encapsulated at low loading concentrations, in order to achieve the desired dose (100 ug of antigen) the particle concentration suitable for oral

murine trials would be too high for forming a well behaved suspension. Along with trying to increase antigen loading, we wanted to ensure high quality antigen is loaded. Protein encapsulated within PLGA particles are known to undergo chemical and physical changes during the emulsion process as well as release (24). These changes can alter the epitopes recognized by B and T cell receptors, potentially producing irrelevant immune responses. Emulsification causes the protein to become exposed to oil-water interfaces, which can result in protein denaturation. To circumvent this interaction, researchers have added protein-stabilizing molecules to formulations. Trehalose has been shown to result in more complete protein release and recognition by antibodies in ELISA assays (24, 125, 126). $Mg(OH)_2$ has also been able to improve release profile and neutralize the acid environment generated during PLGA hydrolysis (24, 126, 127). However, the addition of these agents result in increased osmotic pressure, producing particles with large pores and poor encapsulation efficiency.

An alternative method to stabilizing proteins in PLGA particles is to avoid the inner oil-water interface by adding the protein directly to the oil phase, being termed solid/oil/water (S/O/W) emulsion (24, 128). Protein addition directly to the oil phase kinetically traps the protein in its native structure, assuming the protein is not soluble in the organic solvent used (23). While this method works well to form larger particles (>10 um), this process relies on the protein to be present in the organic phase at sizes smaller than the desired polymeric particle size. The ovalbumin we used to create particles is commercially provided as a lyophilized powder with large particle sizes. Therefore, the protein was micronized by solubilizing with the trehalose at a 1:2 mass ratio, frozen by

the spiral-wound in-situ freezing technique (SWIFT) method described in Chapter Five, and lyophilized. A powder was generated, with features much smaller than the commercially provided material (Figure 3.4).

Commercial OVA	SWIFT Prepared OVA
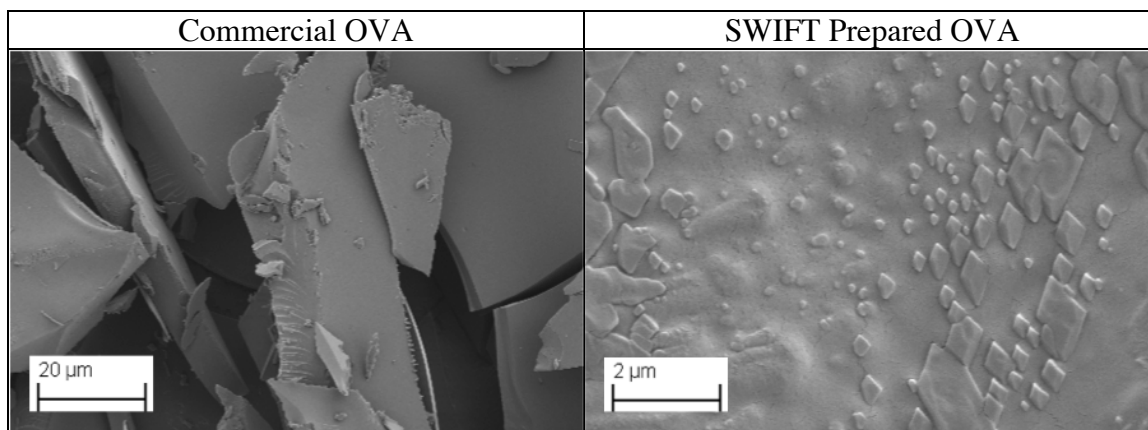
Figure 3.4: SEM images of micronized of ovalbumin powder. Protein powder were sputter coated with Pt/PD and imaged via SEM. Commercial Sigma Grade V ovalbumin powder (left) has particle sizes much larger than 10 um, while SWIFT prepared ovalbumin has characteristic lengths less than 5 um.

The SWIFT prepared OVA was added to oil phase and attempted to be made into a dispersion along with $Mg(OH)_2$. However, presence of the SWIFT powder, containing OVA, greatly reduced the ability to form spherical particles (Figure 3.5.)

S/O/W (No OVA)	S/O/W (w/ OVA)
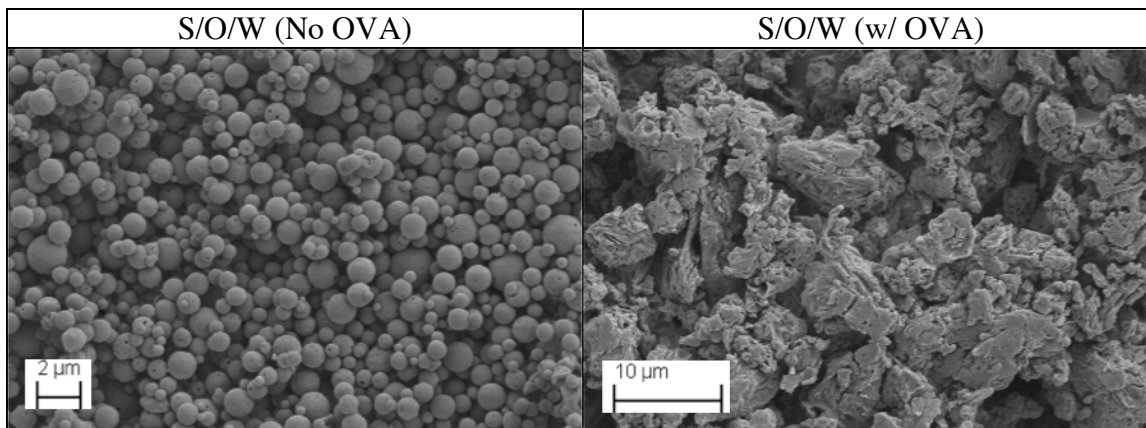
Figure 3.5: SEM images of S/O/W preparation with and without OVA. Lyophilized PLGA preparations were sputter coated with Pt/PD and imaged via SEM.PLGA particles were synthesized without an inner water phase (left). Micronized OVA was added directly to the oil phase, resulting in loss of uniform particle formation (right). Both formulations contained the same excipients except for the addition of ovalbumin.

The S/O/W process was unable to effectively encapsulate ovalbumin to form particles smaller than 5 μm. The lack of spherical PLGA particle formation from this process is likely due to two factors: protein powder particle size relative to PLGA particle size and protein localization at the oil-water interface. The latter factor is likely to be the primary concern for ovalbumin. When PLGA particles encapsulating ovalbumin are dissolved in DCM and then mixed with an aqueous phase, there is a relatively small amount of protein able to be extracted to the aqueous phase (compared to other proteins such as BSA and lysozyme) (129). We also observed an inability to efficiently extract ovalbumin from DCM into an aqueous phase after extended mixing, measured by size exclusion HPLC (data not shown).

Given the lack of particle formation using the S/O/W process, efforts were directed towards stabilizing the particles formed by the W/O/W double emulsion process.

Prior literature has shown the inclusion of solute, such as sucrose or NaCl, into the outer aqueous phase increases protein encapsulation efficiency (130, 131). This effect may be driven by balancing the osmotic pressure between the inner and outer aqueous phases and/or altering the electric double layer of the droplets. It is likely that the external phase additives stabilize emulsion droplets, preventing coalescence. Therefore, we tested several conditions incorporating various solute amounts to the external aqueous phase during the W/O/W double emulsion process (figure 3.6).

| No External Phase Additive | 5% Sucrose | 5% NaCl |
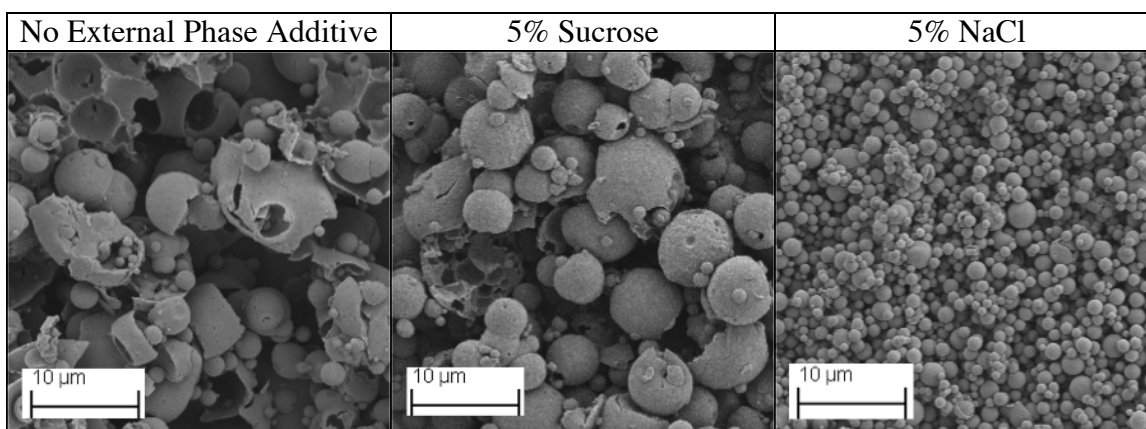
Figure 3.6: SEM images comparing morphology effects of external aqueous phase additives. Lyophilized PLGA preparations were sputter coated with Pt/PD and imaged via SEM. PLGA particles formed without any external phase additives (left) were highly porous and lacked spherical morphology. The addition of 5% sucrose w/v to the external aqueous phase (center) exhibited an improved morphology, while still showing high polydispersity and porosity. Particles formed when 5% NaCl w/v was added to the external aqueous phase (right) revealed no observable porosity and showed reduced size and polydispersity.

While the addition of 5% sucrose exhibited a slight improvement on particle morphology, the addition of 5% NaCl had a dramatic effect. Particles formed by the addition of NaCl were not porous, considerably smaller, and less polydisperse. All of the above formulations were produced with the same amount of $Mg(OH)_2$ added to the organic phase, and both trehalose and ovalbumin added to the inner aqueous phase.

Adjusting the NaCl concentration from 2.5% to 7.5% had no noticeable changes in morphology (data not shown). The final formulation consisted of a 1.25:1.00 trehalose:ovalbumin mass ratio in the inner aqueous phase and a 2.1% w/w $Mg(OH)_2$/PLGA concentration.

SEM images did observe occasional patches of particles that appeared to exist within a continuous phase. By reducing the amount of PEMA in the aqueous phase during the solvent evaporation step from 1% to 0.3% w/v particle size and morphology was unaffected, but the continuous phase observed by SEM was considerably less. Incorporating more rigorous washing steps after solvent evaporation, such as vortexing and water bath sonication, further reduced this continuous phase. The optimized formulation exhibiting high quality particle morphology is shown below in Table 3.1.

Phase/Excipient	Amount
Inner Aqueous Phase	300 μl
Ovalbumin	40 mg/ml
α,α Trehalose	50 mg/ml
Oil Phase	8 ml
PLGA	350 mg
$Mg(OH)_2$	7.5 mg
External Aqueous Phase (pH 7.5)	50 ml
PEMA	1% w/v
NaCl	5% w/v
Solvent Evaporation Solution (pH 7.5)	100 ml
PEMA	0.3% w/v
NaCl	5% NaCl

Table 3.1: Optimized PLGA particle formulation recipe

When this optimized formulation is used with the traditional emulsifying surfactant PVA instead of PEMA, a noticeable difference in morphology is observed. While the particle size is similar, the surface of PVA prepared particles is considerably

more ruffled, shown in Figure 3.7. This ruffling effect in the PVA formulated particles is

not seen when OVA, Mg(OH)$_2$, trehalose, and NaCl are added to the formulation.

PEMA	PVA
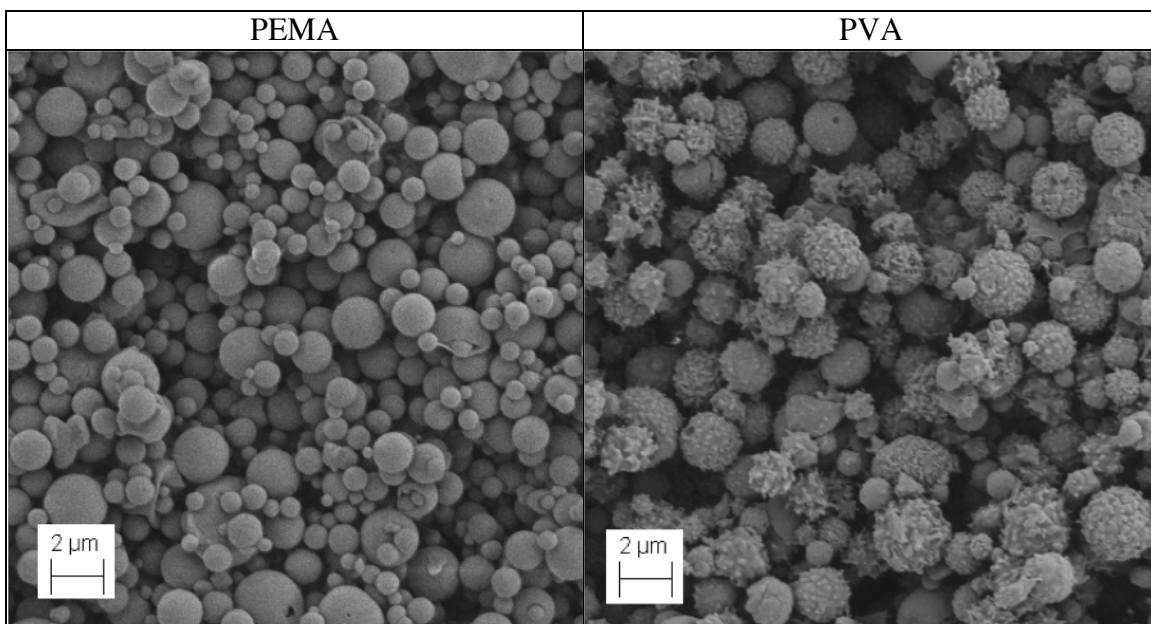
Figure 3.7: SEM images of morphology effects in optimized formulation due to surfactant. Lyophilized PLGA preparations were sputter coated with Pt/PD and imaged via SEM. Particles formed using PEMA show a smooth surface, while particles formed with PVA exhibit a highly ruffled surface.

Particle Display and Encapsulation of Protein

The above formulation was used to analyze the ability to display proteins on the

particle surface. Employing acid end-capped PLGA in the synthesis process results in

free carboxylic acid groups on the particle surface, which can then be used to generate

amid bonds with molecules possessing primary amine groups (such as those found on

lysines and the n-terminus of proteins). However, it has been shown that the emulsifying

surfactant can become embedded at the particle surface, which may block accessibility to

the PLGA carboxylic acid groups (132). The synthesis protocol was modified by

switching the emulsifying surfactant from poly(vinyl alcohol) (PVA) to poly(ethylene-

alt-maleic acid) (PEMA) used in the outer aqueous phase, previously shown to increase the amount of molecules able to be coupled to particle surface (133). PEMA contains carboxylic acid groups, which support additional sites for amide bond formation. The chemical structures for acid-end capped PLGA, PVA, and PEMA are shown below in Figure 3.8.

| Acid End-Capped PLGA | PVA | PEMA |
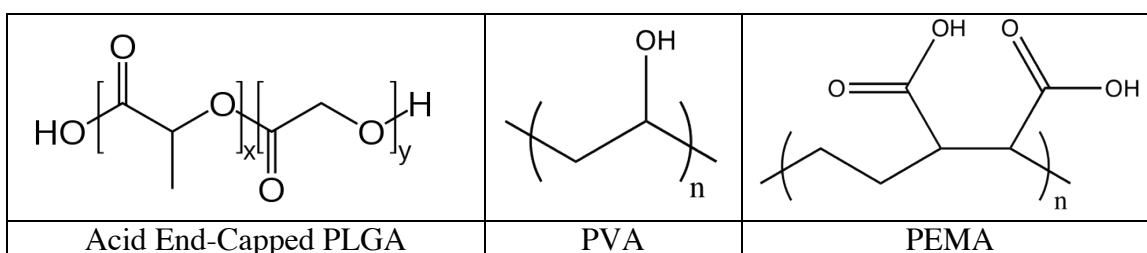
Figure 3.8: Chemical structures of polymers used for particle synthesis

In order to test the effects of emulsifying surfactant substitution, we used 1-Ethyl-3-[3-dimethylaminopropyl]carbodiimide hydrochloride (EDC) and N-hydroxysulfosuccinimide (Sulfo-NHS) chemistry to conjugate MBP-497 to the particle surface. We then measured coupling efficiency by labeling the particles with a mouse anti-invasin antibody, followed by a fluorescent anti-mouse antibody, then analyzed particles by flow cytometry. The amount of coupled MBP-497 is greatly influenced by the emulsifying surfactant. This surfactant substitution resulted in a ~20 fold increase in fluorescence signal for particles coupled to a fusion protein consisting of maltose binding protein and the c-terminal 497 amino acids of invasin (MBP-497)(Figure 3.9). Lengthening the reaction time, from 2 hrs to 21 hrs, increases the amount of coupled protein by ~3 fold when using PVA. However, when PEMA is used the increased time

only increases the fluorescence shift by ~1.2 fold. These relative differences in the amount of conjugated protein are likely affected by the amount of carboxylic acid groups found on the particle surface and the amount of MBP-497 added to the reaction (0.3 mg/ml).

	SAMPLE ID	Median:FL2-H
	PVA (-)	1.86
	PEMA (-)	2.13
	PVA 2 hour	47.8
	PVA 21 hour	167
	PEMA 2 hour	866
	PEMA 21 hour	1037
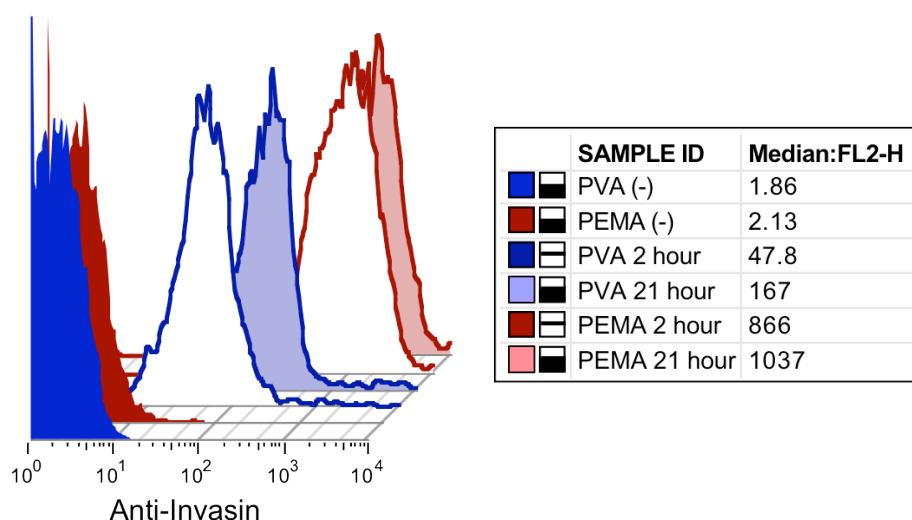
Figure 3.9: Flow cytometry histogram plots showing amount of coupled protein can be tuned using emulsifying surfactant. PLGA particles were either formed with PVA (blue) or PEMA (red). The particles were then labeled with 3A2 mouse anti-invasin mAb, followed by a fluorescent anti-mouse antibody. The solid color profiles without a bold border correspond to particles not conjugated to MBP-INV. Particles undergoing a 2 hr reaction with MBP-INV are shown as profiles with only a bold color border. Overnight (21 hrs) reaction coupling reactions are shown as shaded profiles with a bold color border.

The MBP-497 protein used consists of maltose binding protein genetically fused to the extracellular 5 domains of invasin. The D4-D5 domains are responsible for receptor binding, while the D2 domain facilitates self-association forming dimers and tetramers (96). We compared the ability of an anti-invasin antibody to recognize the D4-D5 binding domain of particles coupled to MBP-INV fusion proteins containing all 5

extracellular domains or just the D4-D5 domain (MBP-192). While the MBP-497 version is known to produce increased avidity, MBP-192 has a smaller molecular weight (62 kDa vs. 93 kDa). Thus, it was postulated that a smaller molecular weight protein might be able to pack more efficiently on the particle surface, increasing effective avidity when immobilized to the particle surface. We also compared the use of EDC/Sulfo-NHS and EDC alone in the coupling reaction (Figure 3.10). The Sulfo-NHS is able to stabilize the activated carboxylic acid groups, but is considerably more costly than EDC. It is recommended to increase the activation time when Sulfo-NHS is employed, to increase the number of carboxylic acid groups that become activated. In the EDC/Sulfo-NHS reaction, the activating molecules were allowed to react for two hours prior to their removal and addition of MBP-INV. In the EDC reactions, the amount of EDC utilized was doubled and the activation period was terminated after 30 minutes, to reduce the time unstable activated carboxylic acids are in solution.
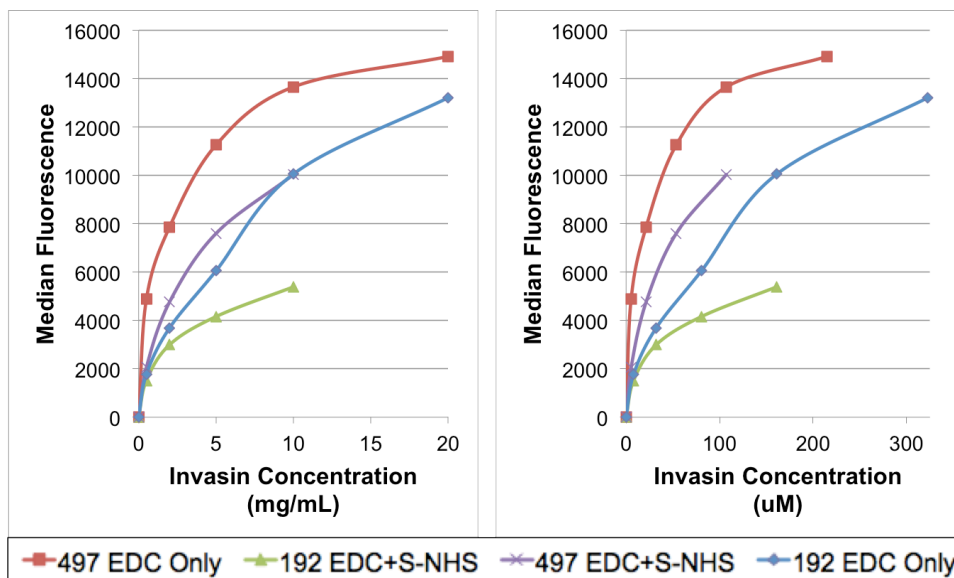
Figure 3.10: Conjugation of MBP-INV to PLGA particles effects based on reaction conditions. The MFIs of anti-invasin labeled particles are plotted as a function of protein concentration in reaction conditions, mass concentration (left), molar concentration (right). MBP-INV in with the c-terminal 497 amino acids of invasin (D1-D5) are shown in red and purple, while the c-terminal 192 amino acid version (D4-D5) are shown in green and blue. Reactions were carried out with either EDC alone (red and blue) or EDC and sulfo-NHS (green and purple).

The MBP-497 version exhibited higher amounts of anti-invasin recognition in both EDC only and EDC/Sulfo-NHS reactions, compared to MBP-192. The EDC only reactions also displayed higher fluorescence compared to EDC/Sulfo-NHS reactions. These results led to future preparations to be formulated in reactions with the MBP-497 version and without the addition of Sulfo-NHS. The MBP-497 version with EDC only begins to show saturation near 10 mg/ml, which is critical for achieving optimal receptor binding. Preparing formulations near this saturating concentration is also important for reducing batch-to-batch variability, since the relative amount of coupled protein is less affected by the protein concentration.

During the process of optimizing the reaction conditions for coupling protein to the particle surface, we attempted to use ovalbumin in proxy of MBP-INV, due to it being readily available and inexpensive. However, we were unable to detect significant changes in flow cytometry fluorescence after conjugation, using an anti-ovalbumin antibody as a primary label. We found significant amounts of ovalbumin to be present on the particle surface after encapsulation, before conjugation (Figure 3.11). Even after conjugation of MBP-INV, a large fluorescence shift specific to OVA was observed, relative to particles not encapsulating OVA. This shift was much more marked in particles formed using PEMA, rather than PVA (while total OVA loading levels were similar: 21 and 16 ug OVA/ mg particles, respectively). The reason for higher surface displayed OVA in particles formulated with PEMA, compared to PVA, is likely due to OVA preferentially interacting with PEMA during the emulsification process.

Surfactant	PEMA	PVA	PEMA	PEMA
OVA Loaded	No	Yes	Yes	Yes
MBP-INV Conjugated	No	Yes	Yes	No
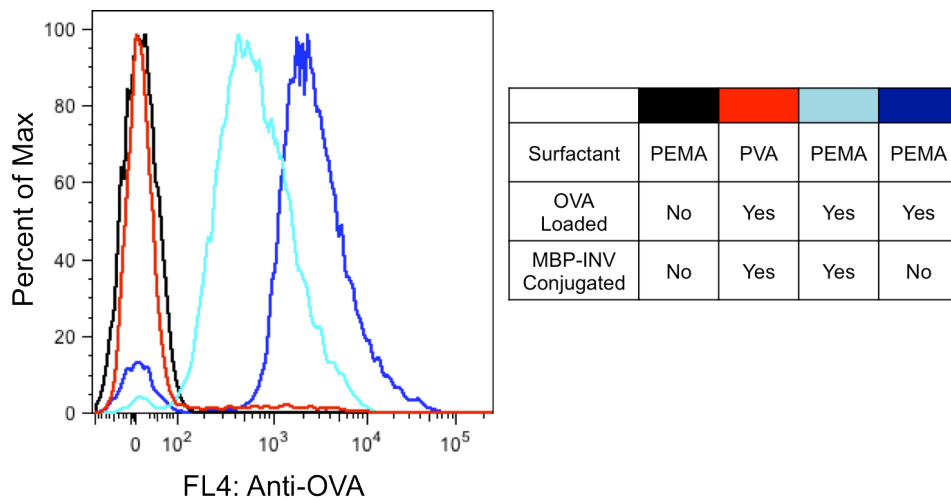
Figure 3.11: Flow cytometry histogram plots of surface displayed OVA after encapsulation. Particles were labeled with a mouse anti-OVA mAb, and fluorescent secondary anti-mouse antibody, followed by flow cytometry analysis (left). The formulation conditions are shown in the legend (right). The MBP-INV used for conjugation was wild-type in the D1-D5 construct.

In order to claim *in vivo* immune response differences between particles (conjugated to different MBP-INV variants) are due to the affinity, it is important to measure the relative amount of protein on the particle surface as well as the activity of the variants. We employed the flow cytometric analysis techniques used above to measure these properties. The variants of interest are: a version that has greatly reduced binding capability via a single amino acid substitution (D911A), the wild-type invasin sequence, and the optimized invasin variant engineered in Chapter Two (RGD844). Since the 3A2 anti-invasin antibody used to stain MBP-INV binds the D4-D5 domain, where the variants' substitutions are located, it was possible the anti-invasin antibody has altered affinity towards the MBP-INV variants. Therefore, an anti-MBP antibody was used to bind a region of the MBP-INV that is constant between the variants, along with the anti-

invasin (Figure 3.12). All samples were analyzed after resuspension of a lyophilized

powder.
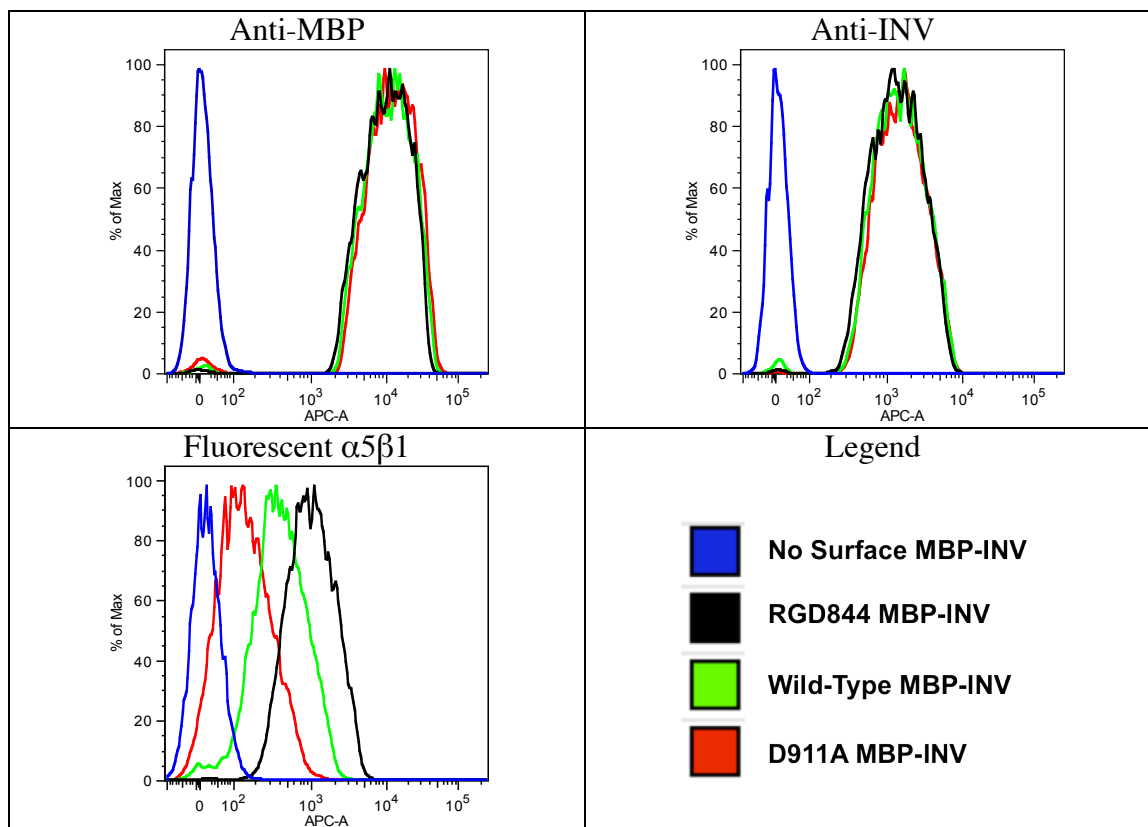
Figure 3.12: Characterization of MBP-INV variants on particle surface via flow cytometry. PLGA particles were conjugated to MBP-INV (D1-D5 version) with either the D911A substitution (red), the wild-type sequence (green), or the optimized $\alpha5\beta1$ integrin binding variant RGD844 (black). Unconjugated particles are shown in blue. To measure the relative amount of surface conjugated protein, the particles were labeled with anti-MBP (top left) or anti-invasin (top right), followed by a fluorescent secondary antibody, and analyzed via flow cytometry. The relative activity of the conjugated MBP-INV variants was measured by labeling particles with fluorescent $\alpha5\beta1$ integrin (bottom left). Color-coded legend is shown in the bottom right.

The fluorescence profiles measuring the presence of different MBP-INV variants

show no discernible difference and also indicate that the 3A2 anti-invasin antibody

binding is unaffected by the substitutions in the D911A and RGD844 variants. However,

there is considerable difference between the fluorescent signatures of particles labeled

with the fluorescent α5β1 integrin. The fluorescence shifts due to integrin recognition agree with those expected due to binding ability of the variants measured in Chapter Two (RGD844 has the highest fluorescence, followed by wild-type, and then D911A). This indicates that differences observed by any *in vivo* immune responses are not due to variability in the amount of targeting protein coupled to the particle surface, but rather their ability to target M cells and/or increase adjuvanticity.

In Vitro Costimulation of Antigen Presenting Cells

Prior literature has shown invasin derived from *Yersinia* to have adjuvant properties. One study demonstrated a peptide from invasin directly engages integrins on the surface of T cells, resulting in proliferation and cytokine release (76). Another study has shown IL-8 release from HeLa cells when stimulated by particles with invasin on their surface (80). This adjuvanticity is believed to be caused by clustering of integrin receptors, leading to activation of the Rac-1 pathway (78). We sought out to test whether invasin was capable of upregulating costimulatory molecules on antigen presenting cells expressing α5β1 integrin, RAW 264.7 macrophage cells (134). Therefore we added particles conjugated to MBP-INV to cultures of RAW 264.7 cells and measured changes in the surface costimulatory molecules CD-40 and CD-86 via flow cytometry (Figure 3.13). The presence of MBP-INV was found to be significantly different from unconjugated particles and the relative amounts of D911A and wild-type variants found to be similar, measured by anti-invasin and flow cytometry.
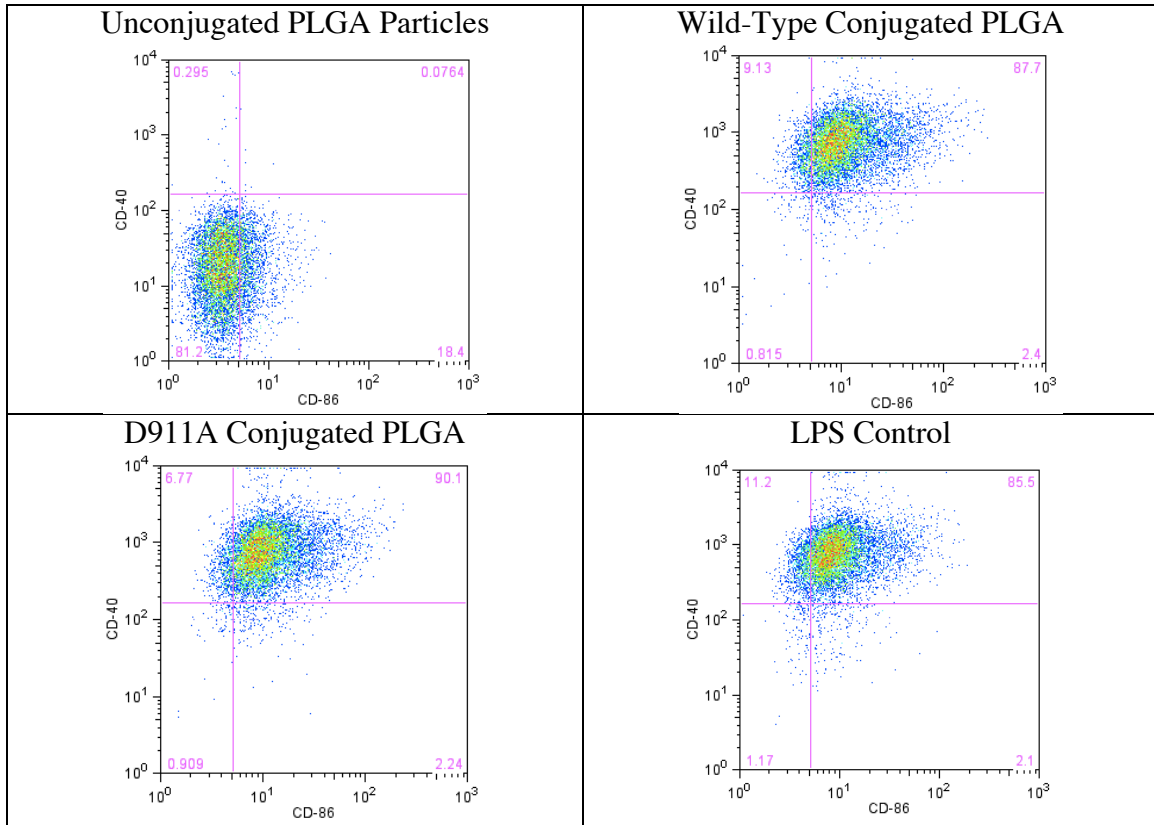
Figure 3.13: Flow cytometry co-stimulation analysis of RAW 264.7 cells incubated with MBP-INV conjugated PLGA particles. RAW 264.7 macrophage cells were incubated with PLGA microparticles overnight, stained with fluorescent anti-CD40 and anti-CD86 antibodies, then analyzed via flow cytometry. Analysis of cells incubated with 100 ng/ml LPS (no particles) is shown in the bottom right.

Overnight incubation of PLGA particles conjugated to wild-type MBP-INV induced significant increases in CD-40 and CD-86 expression on RAW 264.7 cells, compared to unconjugated particles. However, the D911A version, which has a substantially diminished ability to bind integrin receptors also showed the same marked increase in costimulation. This same effect was also observed in our LPS control, which is a well known adjuvant that upregulates costimulation via interaction of TLR-4 (135). Since the MBP-INV protein was prepared from bacteria the upregulation of costimulatory molecules in the RAW 264.7 cells is likely due to LPS contamination.

85

Traditionally, vaccine formulations avoid the presence of endotoxins such as LPS, due to the inflammatory responses induced by MyD88 activation. However, responses to LPS by intestinal immune cells is muted in order to accommodate colonization of commensal bacteria in the GI tract (50). Given that any oral vaccine is likely to become contaminated by LPS via transit through the GI tract and the lack of its ability to activate TLR-4 in intestinal immune cells, the LPS contamination is not a concern. However, this LPS contamination did impede our ability to investigate the ability of invasin to activate RAW cells via integrin engagement. Therefore we attempted to remove LPS from the MBP-INV preparations using an established procedure of washing the protein with a detergent, Triton-X114 (136). The RAW activation assay was carried out as above, but using particles conjugated to protein washed with Triton-X114 (Figure 3.14).
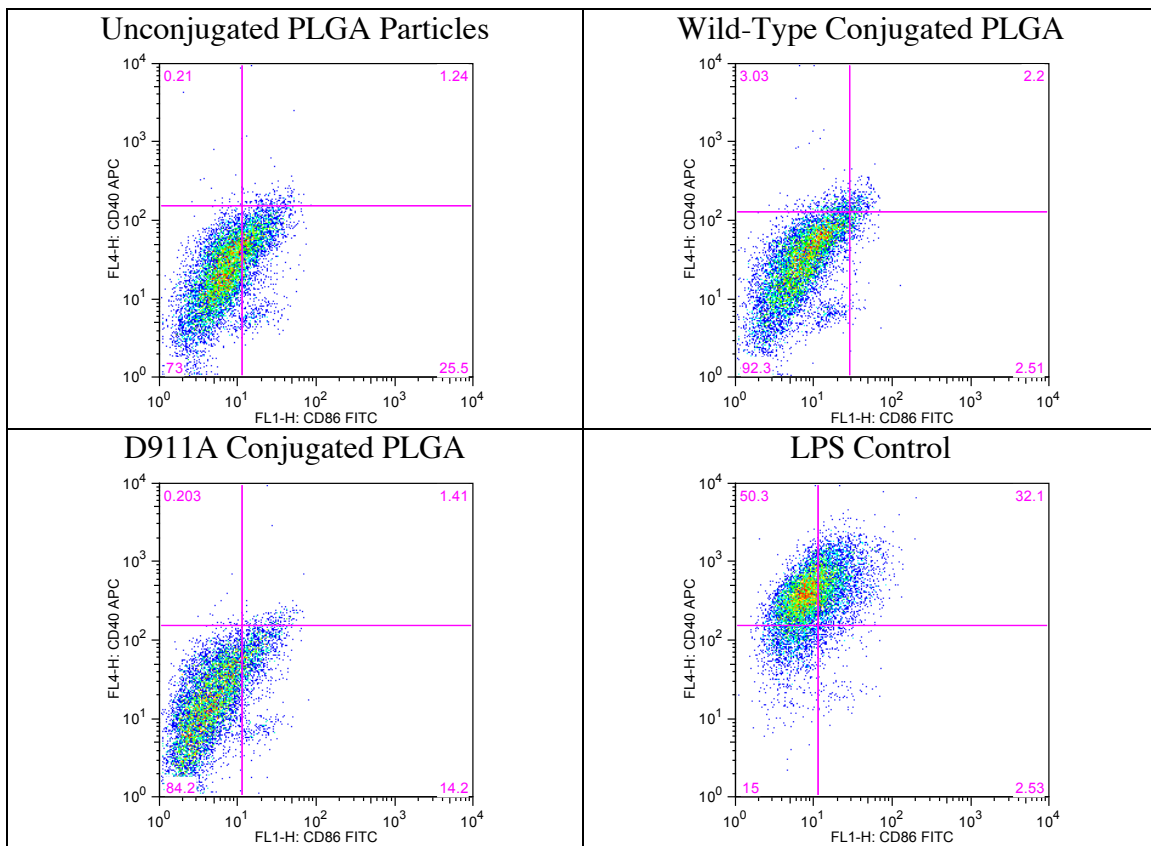
Figure 3.14: Flow cytometry analysis of co-stimulation using particles conjugated to protein treated with Triton-X114. RAW 264.7 macrophage cells were incubated with PLGA microparticles overnight, stained with fluorescent anti-CD40 and anti-CD86 antibodies, then analyzed via flow cytometry. The wild-type and D911A MBP-INV protein was washed with Triton-X114 prior to conjugation to the PLGA particles. Analysis of cells incubated with 100 ng/ml LPS (no particles) is shown in the bottom right.

After the Triton-X114 treatment both the D911A and wild-type particles produce similar responses to the unconjugated microspheres and untreated cells (not shown). The presence of MBP-INV was found to be significantly different from unconjugated particles and the relative amounts of D911A and wild-type variants found to be similar, measured by anti-invasin and flow cytometry (data not shown). While the activity of the conjugated wild-type MBP-INV variant was not measured, short invasin peptides have

been shown to stimulate T cells through α5β1 integrin (76) and denatured invasin has been shown to mediate cell adhesion (68). While our data does not show invasin costimulatory activation in RAW 264.7 cells, activation may be observed in more representative APCs, such as primary bone marrow derived dendritic cells.

Protection of Invasin after Conjugation to PLGA Particles

In order to demonstrate vaccine efficacy due to M cell targeting, it is important to characterize the capacity of invasin to recognize α5β1 integrin after processing, storage, and transit through the GI tract. Therefore, we investigated various storage and lyophilization excipients on their ability to maintain protein activity and protection from proteolytic cleavage. Lyophilization of proteins is known to increase the stability of proteins, by maintaining the formulation in a dry kinetically trapped state (137). This prevents aggregation caused by collisions between partially denatured proteins. However, lyophilized protein can result in activity loss due to the freezing, dehydration, and rehydration prior to administration. A major factor contributing to this activity loss is believed to be caused by destabilization due to loss of the hydration shell around proteins, during drying (137). The addition of trehalose is able to act as a lyoprotectant that stabilizes solvent exposed polar amino acids, by replacing water molecules (138). Therefore, we added trehalose to the particles prior to lyophilization to evaluate its effect on improving α5β1 integrin recognition (Figure 3.15). The particles were resuspended and labeled with fluorescent α5β1 integrin and analyzed by flow cytometry.
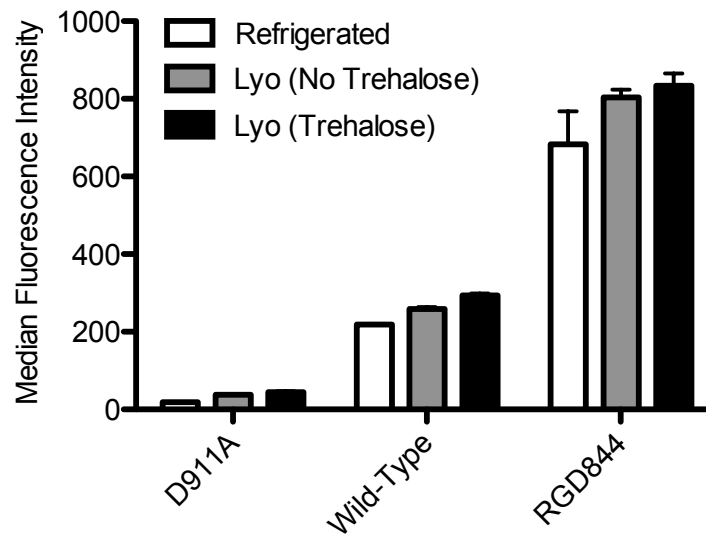
Figure 3.15: Flow cytometry analysis of surface immobilized MBP-INV activity loss due to freezing/lyophilization conditions. PLGA microparticles were conjugated to either the D911A, wild-type, or RGD844 variant of MBP-INV (D1-D5 version) and subjected to either 4-day refrigeration as a suspension (white bars), freezing/lyophilization in 5 mM HEPES pH 7.5, or freezing/lyophilization in 5 mM HEPES pH 7.5 plus 10 mg/ml trehalose. The particles were then labeled with fluorescent α5β1 integrin and analyzed via flow cytometry. MFIs for samples prepared in parallel are shown.

The three variants (D911A, wild type, and RGD844) were evaluated for α5β1 recognition after storage as a liquid at 4°C for 4 days, compared to two freezing/lyophilization conditions. All samples were frozen and resuspended, or stored (refrigerated sample), in 5 mM HEPES at pH 7.5 at 10 mg/ml. For the trehalose condition, the ratio of trehalose to particles prior to freezing in liquid nitrogen was adjusted to 1:1 mass ratio. There were only slight differences in variations between storage/lyophilization conditions. The total signal variation between the refrigerated samples and samples frozen without trehalose was calculated to be 1.1% (Two-way ANOVA, P value=0.0137). While this variation is not dramatic, it is expected to increase

as storage time lengthens. The refrigerated particles clearly sedimented after storage and this condition exhibited the least α5β1 recognition. This sedimentation is likely to lead to increased protein denaturation by increasing the probability of collisions between partially denatured proteins. The difference between samples frozen with and without trehalose was even less, yielding a value of 0.2% (Two-way ANOVA, P value=0.0222). Therefore, we concluded the addition of trehalose as a lyoprotectant was unnecessary.

Another potential loss of invasin activity is *in vivo* denaturation and degradation during transit along the GI tract. The GI tract is designed to degrade proteins to destroy pathogens and promote digestion, which is likely to affect a protein based oral targeting vaccine (139). Oral infection of bacteria has shown proteolytic degradation to be concern for invasin, primarily mediated by serine proteases (140). Efforts have been made to protect proteins during GI tract transit, via formulation with polymers that are insoluble or collapsed at low pH, which dissolve or expand at more neutral pH (141). The pH increases along the length of the GI tract in humans, ranging from below pH 5 in the stomach then increases to 6.5 in the duodenum and becomes neutral in the colon (142). These formulations shield proteins from the acidic pH and pepsin found in the stomach, then release the encapsulated payload in the small intestine. The invasin-conjugated microparticles could be simply granulated and enteric coated using a fluidized bed to enable protection during GI tract transit. However, the pellet size of particles needed for fluidized bed coating would be too large to pass through pylorus of a rodent, our initial *in vivo* model to measure immune responses.

In order to form enteric coated particles suitable for oral rodent delivery, we investigated microencapsulation of the PLGA microparticles with a methacrylic copolymer via spray drying. Peyer's patches, containing M cells, are more prevalent in the distal small intestine (143). Therefore, we choose Eudragit S100 as an enteric polymer, since it is designed to release in the ileum. A previously published microencapsulation spray dying protocol was modified, by substituting the enteric polymer S100 in place of L100-55 and the plasticer triethyl citrate (TEC) in place of Tween-80 (144). This process relies on the dissolution of the enteric polymer, by the addition of NaOH, resulting in a neutral pH solution. Uncoated particles are added to the solution, along with plasticer, and the suspension is then spray dried. The drying process collapses a film of enteric polymer around the particles. Microparticles formed by this process, without the addition of PLGA microparticles, is shown below (Figure 3.16).
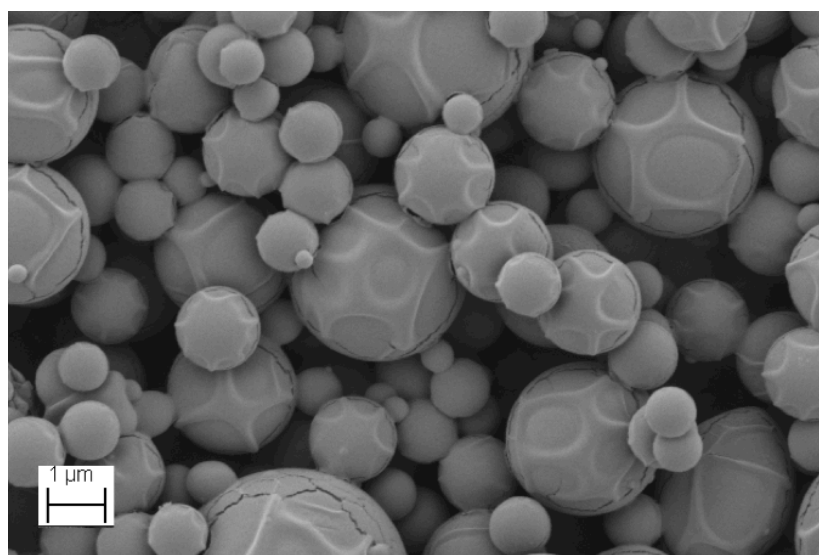
Figure 3.16: SEM image of spray dried EUDRAGIT L100. Solubilized EUDRAGIT S100 was spray dried with 10% TEC, sputter coated with Pt/Pd and imaged via SEM.

This process was able to form particles in the size range expected to effectively coat the PLGA microparticles, while still being small enough to pass through the pylorus of a rodent. However, this process relies on the use of dissolved polymer. Since the polymer was dissolved by the addition of NaOH prior to spray drying, it is expected that the polymer would remain deprotonated in the final dry state. In order to effectively dose the particles with an intact enteric film coating, the powder would need to be resuspended in a sufficiently buffered acidic solution. This buffered solution may then decrease the pH of the fluid in the small intestine, resulting in incomplete dissolution and blocking the invasin-integrin interaction. Also, recovery yields from this small batch process was on the order of 10%, due to powder coating the glass chambers throughout the spray dryer apparatus. Given the lab production scale of MBP-INV, 10% recovery of conjugated particles was not acceptable.

We then investigated an alternative process to incorporate enteric polymer protection. While the S100 polymer is designed for dissolution in the ileum, concerns regarding incomplete dissolution led to future preparations with a polymer designed for dissolution in the human duodenum, L30D-55. Here, the aqueous dispersion of enteric polymer was added directly to the suspension of particles encapsulating OVA, shown to be displayed on the particle surface (Figure 3.11). The suspension was then frozen and lyophilized as above. The result was a matrix powder where the enteric polymer blocks protease access to the particle surface. This powder was resuspended and incubated in the USP simulation gastric test fluid, containing pepsin. The volumetric ratio of resuspension solution and simulated gastric fluid were scaled to represent our dosage volume relative

to the mouse stomach volume (145). The particles were then washed in PBS and analyzed for the presence of surface displayed OVA, using anti-OVA mAb and flow cytometry (Figure 3.17).
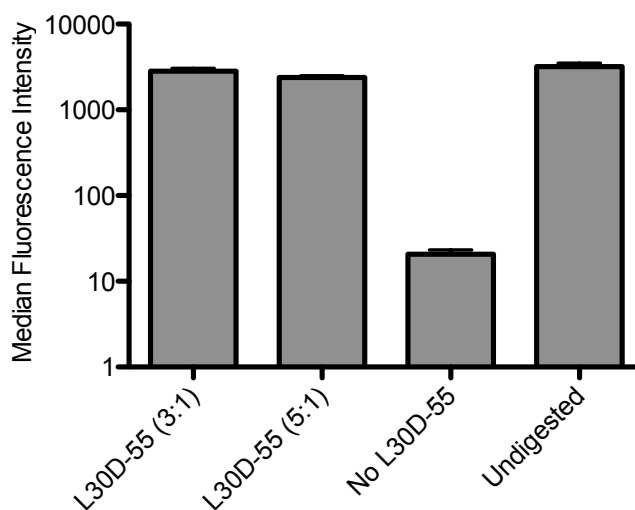
Figure 3.17: EUDGRAGIT L30D-55 protection from simulated gastric digestion measured by flow cytometry. Particles were lyophilized with or without L30D-55 (10% TEC w/w) and subjected to digestion in simulated gastric fluid, with pepsin. Two mass ratios of L30D-55 to particles were used (3:1 and 5:1). Particles were then labeled with a mouse anti-OVA mAb, followed by a fluorescent anti-mouse antibody, and analyzed via flow cytometry. MFIs for separate digestion reaction are shown.

3:1 and 5:1 mass ratios of L30D-55 to PLGA particles were tested. The particles lyophilized with the L30D-55 showed a dramatic reduction in pepsin degradation on the particle surface. The 3:1 formulation showed slightly higher residual anti-OVA recognition compared to the 5:1 formulation, 88% and 74%, respectively. While the minimum film forming temperature (MFT) of L30D-55 is 25°C, the addition of 10% TEC (acting as a plasticer) is able to reduce the MFT to 0°C. The formulation temperature was maintained at or below room temperature during freezing/lyophilization

and resuspension. It is likely the addition of 10% TEC to the suspension had a pronounced affect on creating a pepsin impermeable matrix powder, protecting the particles. This formulation may provide sufficient protection of targeting proteins for oral administration in species exhibiting a stomach pH below 5.5 and an intestinal pH above 5.5. While the rat model has been used as a preclinical model for oral delivery of enteric coated formulations, we chose to use the mouse model, given its more characterized responses and available reagents for immunological experiments (146). However, the pH gradient in the mouse GI tract is not as dramatic as those observed in the rat model and humans, further raising concerns for incomplete dissolution and accessibility of invasin for integrin recognition (145).

In order to ensure the invasin binding domains are able to engage M cells, we investigated formulation excipients that would interfere directly with the protease activity, rather than shielding the particle surface. First, we examined the ability to inhibit intestinal digestion of serine proteases using the USP simulated intestinal test fluid, containing pancreatin. Particle suspension volumes and simulated intestinal fluids were scaled to match our dose volume and mouse intestinal fluid volume (145). MBP-INV conjugated PLGA particles were used for digestion for 75 min at 37°C. Particles were then washed, labeled with the 3A2 anti-invasin mAb, followed by a fluorescent anti-mouse secondary, then analyzed via flow cytometry (Figure 3.18).
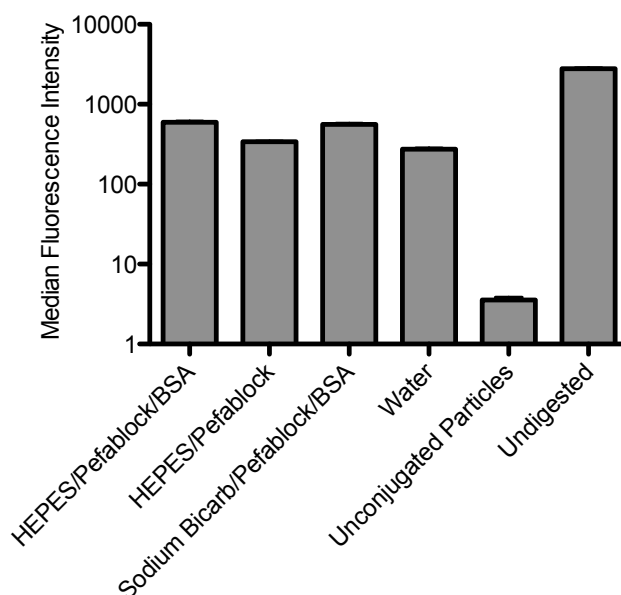
Figure 3.18: Simulated intestinal fluid digestion of surface immobilized MBP-INV analyzed via flow cytometry. Wild-type MBP-INV (D1-D5) PLGA particles were resuspended in potential dosage buffers and incubated with simulated intestinal digestion fluid, containing pancreatin, for 75 min at 37°C. Samples were then labeled with the 3A2 anti-invasin mAb, followed by a fluorescent anti-mouse antibody, and analyzed via flow cytometry. MFIs are shown on a $\log_{10}$ scale for multiple sample digestions. HEPES buffers were 50 mM with 200 mM NaCl, pH 7.5. Sodium bicarbonate buffers were 5% w/v. Pefablock, an serine protease inhibitor was used at 12 mM. Dosage buffers with BSA were 2% w/v. MFIs are shown on a $\log_{10}$ scale for multiple sample digestions.

Pefablock SC Plus (Roche) is advertised as an effective serine protease inhibitor, with low toxicity and inhibition of protein-protein interactions. Since this formulation was being evaluated for *in vivo* dosage, the low toxicity was an important factor for its consideration. In order to balance efficacy, while maintaining low toxicity, 12 mM was chosen as a test concentration, 100-fold below the LD_{50} and above the concentration shown to support strong protease inhibition (4 mM). While Pefablock is not able to inhibit pepsin degradation, pH neutralizing dosage buffers (5% sodium bicarbonate) can inactivate pepsin. However, pH solutions above 8.0 are known to rapidly hydrolyze

Pefablock. Therefore, two buffers were evaluated, 50 mM HEPES (pH 7.5) and 5% sodium bicarbonate (pH 8.3). The HEPES solution with only Pefablock resulted in less than a 3% improvement on anti-invasin recognition on the particle surface, compared to resusupension in ddH$_2$O. Given the potential hazards and side-effects of administering a protease inhibitor, this improvement was not sufficient to justify its use for oral administration. However, the addition of 2% BSA increased the anti-invasin recognition by over 10% in both the HEPES and sodium bicarbonate solutions, compared to water. Recently, is has been shown that administration of bystander protein, such as BSA, may help protect oral vaccine targeting ligands (147). This effect may be more pronounced in the fasted state, when there are fewer targets for gut proteases. Therefore, BSA was chosen as the preferential excipient to protect invasin during transit through the small intestine. It should be noted that even with 2% BSA, only ~20% residual recognition was observed, compared to unconjugated particles. However, our experimental conditions simulated particles transiting the entire length of the GI tract before analysis for digestion. In reality, some particles will interact with α5β1 integrin during gut transit, so the actual percent of invasin available for recognition should be higher than tested in our experimental conditions.

As mentioned above, pepsin becomes inactive at pH's above 5 and irreversibly inactivated at pH's above 7 (148). Therefore, we sought to measure the residual presence of the D4-D5 domain on the particle surface in simulated gastric conditions, utilizing 5% sodium bicarbonate to neutralize the pH of the stomach (Figure 3.19).

96
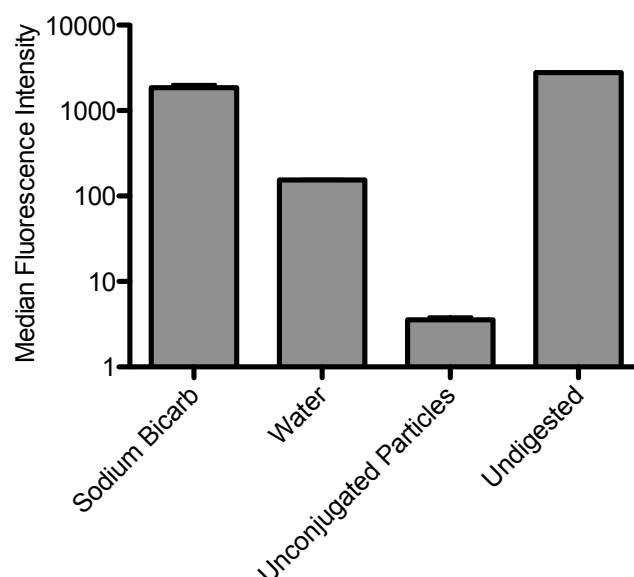
Figure 3.19: Simulated gastric fluid digestion of surface immobilized MBP-INV analyzed via flow cytometry. Wild-type MBP-INV (D1-D5) PLGA particles were resuspended in either water of 5% sodium bicarbonate and incubated with simulated intestinal digestion fluid, containing pepsin, for 75 min at 37°C. Samples were then labeled with the 3A2 anti-invasin mAb, followed by a fluorescent anti-mouse antibody, and analyzed via flow cytometry. MFIs are shown on a $\log_{10}$ scale for multiple sample digestions.

The pH of 5% sodium bicarbonate solutions was measured to be 8.3, which is above that needed to inhibit and inactivate pepsin. There was greater than 60% improvement in anti-invasin recognition using 5% sodium bicarbonate, compared to water. This represents >65% of signal retention, compared to unconjugated particles. Given this information, the final dosage buffer was chosen to be 5% sodium bicarbonate with 5% BSA, in order to inactivate pepsin and competitively inhibit serine protease activity. This dosage formulation does not rely on any polymer-based protection, which may preclude accessibility of invasin.

In Vivo Formulation Characterization and Antibody Responses

In order to test our oral vaccine formulation, we tested our system in the mouse model (C57bl/6 strain). In addition to the optimized formulation discussed above, we added an adjuvant along with OVA to the inner water phase for several sample groups. The adjuvant selected, single-stranded CpG DNA, has been shown to be an effective mucosal adjuvant increasing total specific IgG responses, shifting helper T cell responses to the Th1 type, as well as boosting CD8 T cell responses (149-151). Historically, TLR9 activation has been thought to rely on recognition by unmethylated CpG motifs, while more recent studies have shown this to only be true when a phosphorothiate (PS) modified DNA backbone is used (152). The use of PS DNA was popularized because of increased resistance to nucleases, compared to phophodiester (PD) backbones. The PS backbone also helps enable endocytosis, where the adjuvant is then able to engage TLR9 within the endosome. However, once internalized, PD DNA is capable of TLR9 recognition in a less sequence dependent manner (152). Immune responses from particle-based vaccines have been shown to be enhanced by the addition of PD DNA (151). Therefore, we chose to incorporate a PD DNA sequence as an adjuvant, which has considerable less cost than the PS DNA alternative.

Particles were synthesized using the optimized formulation described above, with or without CpG DNA and used for conjugation to the MBP-INV targeting protein variants (D911A, wild-type, and RGD844), all in the D1-D5 format. These particles were then characterized via multiple biophysical methods (Table 3.2). Unfortunately, the encapsulation efficiency of the PD DNA was extremely low, ~0.01%. There was some

detection of ssDNA in the particles not loaded with CpG DNA, which is likely due to bacterial DNA associated with the MBP-INV protein used for conjugation. While there was over two-fold increase in measured ssDNA in PLGA particles synthesized with CpG DNA, the total amount is likely not sufficient to have an effect as an adjuvant. Typical murine vaccine studies use 2.5-10 ug of CpG DNA per dose, while our dose would contain <50 ng of CpG DNA (151, 153). This low encapsulation efficiency may be improved upon in the future by conjugating the CpG DNA to a soluble bulking agent, such as the protein antigen. Ovalbumin encapsulation efficiencies for particles loaded and not loaded with CpG DNA were 55% and 45%, respectively. The amount of OVA encapsulated could not be determined directly after conjugation due to interference of the MBP-INV in the micro BCA assay. However, performing "mock" conjugation reactions and release studies estimate on the order of 5% or less OVA loss during conjugation (data not shown). It is important to note that "mock" conjugation reactions where hydroxylamine was used to quench unreacted activated carboxylic groups resulted in a saturated micro BCA assay signal, after expedited hydrolysis. This effect may be due to the PEMA surfactant forming poly[ethylene-alt-(N-hydroxlmaleimide)](154), which could be recognized by the BCA assay. Therefore, the "mock" reaction conditions used to determine OVA losses during conjugation underwent the same washing conditions and reuspension time as the actual reactions, but did not have EDC or hydroxylamine steps. Release studies in 50 mM HEPES 200 mM NaCl 0.005% Trition-X100 also showed ~5% release in 6 hours, followed by no release up to one week (data not shown).

Sample	CpG Loaded	Hydrodynamic Diameter (nm)	Zeta Potential (mV)	Loading (ug OVA/ mg particle)	CpG DNA (ng DNA/ mg particle)
Preconjugation	Yes	1054 ± 18	-55.02 ± 0.66	24.3 ± 1.3	ND
D911A	Yes	1088 ± 22	-36.18 ± 0.57	ND	11.4 ± 0.13
Wild Type	Yes	1053 ± 17	-38.40 ± 0.63	ND	11.5 ± 0.20
RGD844	Yes	1097 ± 57	-39.82 ± 0.37	ND	10.4 ± 0.24
Preconjugation	No	759 ± 5.4	-44.16 ± 0.68	20.3 ± 2.3	ND
RGD844	No	764 ± 11	-38.29 ± 0.46	ND	4.57 ± 0.12

Table 3.2: Characterization PLGA particles used for in vivo administration. PLGA microparticles were characterized by dynamic light scattering (DLS), averages from multiple measurements fitted with CONTIN are shown. Zeta potential averages are shown for multiple measurements. The amount of OVA encapsulated was determined using a micro BCA assay after expedited hydrolysis. The amount of ssDNA encapsulating was determined using the Quant-iT RiboGreen assay kit after solvent extraction. ND= Not Determined

Prior literature has shown that differences in particle size and surface charge can lead to variations in the extent and type of immune responses, based on their transport and adsorption properties (43, 155-157). Therefore, it was important to determine if there were any significant size or charge differences between the samples groups. Multiple dynamic light scattering measurements were made for each sample and the correlation function for each measurement was fitted with CONTIN. The volume averages for each sample shown in Table 3.2 agree with SEM images of dry powder (not shown). The polydispersity and hydrodynamic diameter was slightly larger for the samples loaded with CpG DNA. This effect mimics the observations made above, showing increasing the solute of the inner aqueous phase results in larger and more polydisperse particles (Figure

3.3). However, spherical particle morphology was maintained in samples loaded with CpG DNA, likely stabilized by the addition of 5% NaCl to the outer aqueous phase. The surface charge of unconjugated PLGA microparticles was determined to be -55 and -44 mV in 0.5 mM KCl for particles loaded and not loaded with CpG DNA, respectively. This charge difference may be due to the presence of the negatively charged CpG DNA on the particle surface. After conjugation of MBP-INV variants to the particle surface, the surface charge becomes less negative. Prior to conjugation the particle surface is composed of many carboxylic acid groups, used for coupling to primary amine groups on the MBP-INV variants. Many of these carboxylic acid groups are replaced by MBP-INV, which have surfaces composed of mixtures of polar side chains with positive, neutral, and negative charges. This modification makes the surface more positive. The amount of MBP-INV was found to be the same for all samples, measured by flow cytometry using anti-MBP and anti-INV mAbs (Figure 3.12, top panels). The particles also exhibited flow cytometry offsets when labeled with fluorescent $\alpha 5\beta 1$ integrin, corresponding to their affinity (Figure 3.12, bottom left). Particles not loaded with CpG DNA (RGD844) are not shown in Figure 3.12, but track identically with the non-CpG loaded (RGD844) sample for all labels.

The sample groups used for *in vivo* studies are shown in Table 3.3. Mice were dosed on day 0, 14 and 28 days. Serum samples were collected prior to dosing, at 14 days, 28 days, and at day 47. Serum samples were analyzed by ELISA for total specific IgG (Figure 3.20). The OVA specific ELISA (Figure 3.20, left) shows anti-OVA responses for the "Free OVA" and "Alum" groups, while the other groups had no serum

IgG response to OVA. This indicates the designed targeted oral vaccine system was not able to induce a serum specific antibody response directed towards the encapsulated antigen, OVA. It is interesting to note that there was a clear response to soluble OVA orally administered, comparable to the positive control "Alum" group. This response was surprising given the body of literature that supports the need for advanced delivery systems needed for oral vaccination. The adjuvant, CpG DNA, was included as a soluble agent in the "Free OVA" formulation. However, it is not likely to have played a role, given the low dose and nuclease susceptible phosphodiester form used. The other two excipients present, sodium bicarbonate and BSA, may have played a strong role in protecting the antigen during GI transit. Even with this protection, the lack of adjuvant and potential for tolerance induction makes this result notable and surprising.

Group	Administration Route	OVA (ug)	Particle Based	Adjuvant	MBP-INV Variant
Naïve	Oral	0	No	None	N/A
Free OVA	Oral	100	No	CpG	N/A
D911A (CpG)	Oral	100	Yes	CpG	D911A
Wild-Type (CpG)	Oral	100	Yes	CpG	Wild-Type
RGD844 (CpG)	Oral	100	Yes	CpG	RGD844
RGD844	Oral	100	Yes	None	RGD844
Alum	S.C.	100	No	Alum	N/A

Table 3.3: *In vivo* immunization sample groups. Each sample group is shown by name along with distinguishing characteristics between them. Oral dosed samples were administered in 5% sodium bicarbonate/ 5% BSA, 250 ul per dose. Alum subcutaneous (S.C.) doses were administered by 100 ul injection behind the shoulder blades. Particle bases formulations use PLGA microparticles encapsulating OVA and were conjugated to the designated MBP-INV variant in the D1-D5 construct. The "Free OVA" group was prepared with soluble ovalbumin and 50 ng of CpG DNA. All groups were fasted for 6-8 hours prior to dosing and boosted at 14 and 28 days with the same formulation.
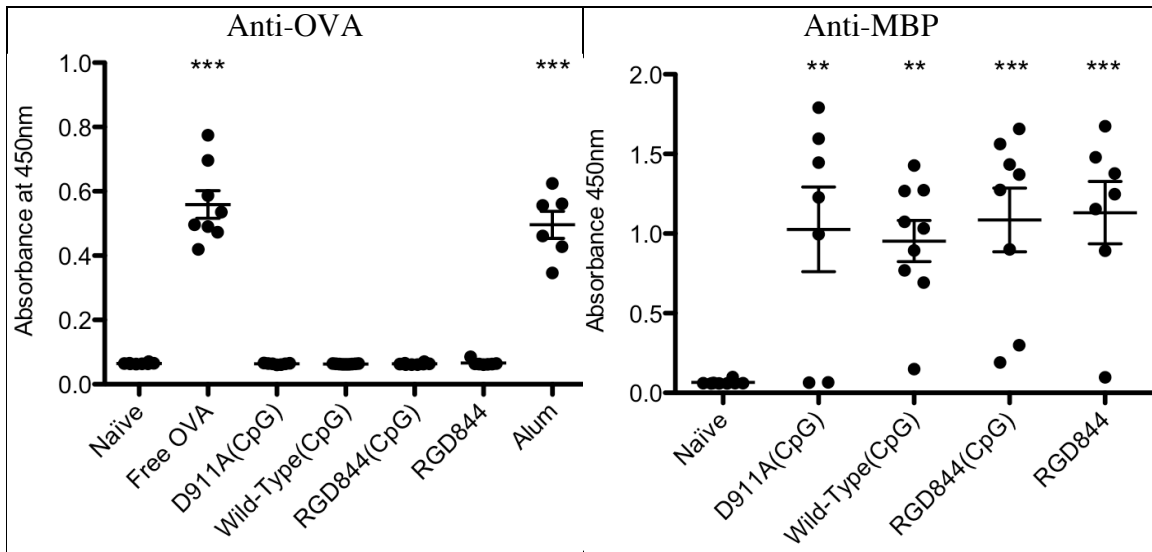
Figure 3.20: Specific total IgG responses. Total IgG responses were analyzed (1:200 dilution) at day 47, by coating ELISA plates with ovalbumin (left) or maltose binding protein (right). Each individual point represents the average signal from a single mouse measured in duplicate. (Significance relative to naïve group ** $P<0.01$, ***$P<0.001$, calculated using Dunnett's method of one-way ANOVA)

Serum from sample groups that utilized the MBP-INV targeting protein was analyzed for specific IgG responses directed towards MBP. These results showed significant differences compared the naïve group. However, the differences in responses between test groups were not significant, even at higher dilutions (1:1,000; 1:5,000, and 1:25,000). The lack of difference between the RGD844 groups with and without CpG DNA was not surprising, given the low amounts of CpG DNA loaded. The reason for lack of differences between targeted groups (D911A, wild-type, and RGD844) could be due to several factors. One potential reason is that the MBP-INV protein is sufficiently degraded during transit through the GI tract, leading to inefficient recognition of $\alpha5\beta1$ integrin. This reason would be supported by previous literature demonstrating that immune responses to M cell targeting vaccines were greatly enhanced when the particles were administered by intraduodenal injection, compared to oral gavage (42). However, in the Fievez et al. study there was not a significant difference in responses between free OVA and the naïve group. This indicates that the soluble OVA dosed in their "Free OVA" group was degraded, while ours was not. The addition of 5% sodium bicarbonate and 5% BSA may have also protected the MBP-INV, retaining some $\alpha5\beta1$ integrin recognition on the apical surface of M cells. Another potential reason for the lack of difference in anti-MBP responses between targeted groups could be due to saturation of M cell uptake. There is likely a dose response effect, where no response is observed at a low enough dose, a response dependent on the ability to target M cells in a mid-range dose, and saturation of responses at high doses. A future dose response study, with and without BSA, may help elucidate the reasons for the effects observed and determine an optimal dose for future studies.

The other major notable finding was the discrepancy between the anti-MBP and lack of anti-OVA responses for the PLGA particle groups. The presence of the serum IgG

response directed at MBP was not surprising, as it was fused to the invasin variants that were conjugated to the surface of the particles. The presence of OVA and MBP were both found to be present on the particle surface after conjugation, by staining the particles with anti-OVA and anti-MBP mAbs, respectively (Figures 3.11 and 3.12, top-left). Also, we previously found unconjugated PLGA particles encapsulating OVA to generate serum IgG responses when administered orally and subcutaneously, although this was tested as n=1 sample sizes and with extended times between boosts. Therefore, the lack of IgG responses directed towards OVA was surprising. In order to mount an effective antibody response, antigens must be processed, displayed by MHC molecules, and recognized by B cell receptors. Rather than being surface displayed after encapsulation (OVA), MBP was conjugated to the particles. The chemical conjugation process requires activation of carboxylic acid groups on the particle surface, which would include those found on ovalbumin. After conjugation the reaction was quenched by the addition of hydroxylamine, which could have modified T and B cell epitopes on ovalbumin. It appears that at least one B cell epitope recognized by the anti-OVA mAb (Santa Cruz Biotech 58820) was preserved after conjugation. It is also possible that the highly reactive surface of the particles formed with PEMA became hyper-cross-linked after conjugation, preventing efficient degradation and release of OVA. Digestion of surface exposed OVA after MBP-INV conjugation, using pancreatin, resulted in background levels of anti-OVA mAb recognition in flow cytometry (data not shown). While trypsin is not an endoprotease believed to be important for antigen processing in lysosomes, this experiment shows the surface displayed OVA can be degraded for subsequent peptide presentation on MHC molecules (158). It may also be important to note the MHC class II immunodominant T cell epitope for OVA most studied (ISQAVHAAHAEINEAGR) contains two glutamic acids, which have carboxylic groups. These groups are solvent

exposed in the crystal structure for ovalbumin (pdb file 1OVA) and would be potentially reactive for chemical modification during the conjugation of MBP-INV. Modifications to important T cell epitopes may diminish their ability to be displayed by MHC molecules, decreasing the ability of T cells to respond appropriately. Peptides could also be displayed by MHC molecules, but have modified residues interacting with T cell receptors (TCR). While an altered responsive TCR repertoire would be a concern for generating pathogen specific T cell responses, it should not affect the generation of a vaccine based antibody response. This is because the antibody response is indirectly linked to the T cell response, which proves useful for conjugate vaccines. The portion of the OVA trapped in the PLGA particles (not surface displayed) should be protected from chemical modification during coupling. The mechanism for the lack of response to OVA in the M cell targeted particle formulations is likely due to one or more of the factors discussed above. The simplest method to circumvent this issue is to co-couple OVA and MBP-INV on the particle surface. This would remove the processing differences between OVA and MBP, which should lead to anti-OVA antibody responses.

CONCLUSION

While there is tremendous importance in generating an oral subunit vaccine, many challenges prevent such delivery systems from modulating immune responses in a manner that will lead to protection from pathogens (9). One solution to improving oral vaccine delivery is to target M cells, in order to facilitate increased antigen presence in mucosal lymphoid tissue (88, 90). As discussed in Chapter Two, we generated and characterized invasin ligands capable of binding an apical M cell receptor, $\alpha 5\beta 1$ integrin, with various affinities. In this chapter, we designed a polymeric PLGA microparticle delivery system capable of testing the *in vivo* immune responses produced by using

106

invasin ligands with altered affinities toward α5β1 integrin. We were able to produce particles, encapsulating the antigen ovalbumin, and conjugate them to soluble forms of the invasin ligand. Substituting the emulsifying surfactant PVA to PEMA resulted in over an order of magnitude increase in the amount of protein displayed on the particle surface. The optimized microparticle delivery system showed α5β1 integrin recognition that was based on the affinity of the invasin ligand coupled to the particle surface. Upon *in vivo* administration, several notable observations were made: 1) soluble oral ovalbumin generated a serum ovalbumin specific IgG response; 2) the PLGA particles showed specific serum IgG responses to maltose binding protein, but not ovalbumin; 3) there were not significant differences in the serum IgG responses based on the invasin ligand used. While these results do not demonstrate a clearly effective oral vaccine system, they do provide valuable insights as to how the formulation may be modified to achieve successful oral vaccination in the future.

MATERIALS AND METHODS

Synthesis of Water-in-Oil-in-Water (w/o/w) double emulsion microparticles

Poly(ethylene-maleic anhydride) was hydrolyzed to poly(ethylene-alt-maleic acid) (PEMA) by heating polymer solutions and the addition of NaOH. PEMA solutions were cooled to room temperature then adjusted to either 1% or 0.3% (w/v) and 5% NaCl (w/v). The pH was then adjusted to 7.5. The inner aqueous phase was prepared with α,α-Trehalose 50 mg/ml, with or without ovalbumin (OVA) 40 mg/ml, with or without the 1826 phosphodiester oligonucleotide (TCCATGACGTTCCTGACGTT) 30 mg/ml, and filtered using a 0.2um PVDF syringe filter (Millipore). 350mg of Resomer and 7.5mg of $Mg(OH)_2$ was weighed out into a 50ml conical. 8ml of methylene chloride was added to

the conical and vortexed. 300ul of the inner aqueous solution was added to a conical and emulsified using a Silverson SL2 T homogenizer at full speed (~11,000 RPM) for 2 min and immediately transferred to 50ml of 1% PEMA-5% NaCl and emulsified again under the same conditions as before. The w/o/w emulsion was then added to 100ml of 0.3% PEMA-5% NaCl and solvent evaporation was carried out for 3.5 hours with stirring. The hardened microparticles were washed three times with ddH2O containing 0.005% Triton X-100 with vortexing and bath sonication used for resuspension in between washes. Washing was facilitated by centrifuging particles at 2,100xg for 20 min. After the last wash a batch was resuspended with wash solution to ~2.5ml, frozen in liquid nitrogen, lyophilized on an external manifold, then stored at -20°C.

MBP-INV Expression

The invasin (INV) targeting proteins were expressed as soluble maltose binding protein (MBP) fusion proteins (MBP-INV). The INV portion was composed of either the c-terminal 497 amino acids (MBP-497) or the c-terminal 192 amino acids (MBP-192) of invasin from *Yersinia pseudotuberculosis*. Three variants of INV were used: wild type (WT), a single amino acid substitution variant with greatly reduced binding affinity (D911A), and an optimized binding variant (RGD844). pMAL-c5x was used as the expression vector, which does not contain the signaling peptide for periplasmic transport. These proteins were co-expressed in Origami B cells (EMD chemicals), along with the Skp chaperone protein on pAR3-Skp, which lacks the native periplasmic signaling peptide. Overnight starter cultures were inoculated into Terrific Broth (TB) media,

containing glucose and antibiotics, and grown overnight at 37°C. The following day, cells were harvested and media was exchanged with fresh TB, without glucose, and was placed on a shaker at room temperature. After 20-30 minutes, arabinose was added to a final concentration of 0.2% to induce c-Skp expression. Then 20-30 minutes later, Isopropyl β-D-1-thiogalactopyranoside (IPTG) was added to 1mM and MBP-INV expression was carried out for 4-5 hours. Cells were then harvested and cell pellets were stored at -80°C until purification.

MBP-INV Purification

Harvested cell pellets were resuspended and lysed via a French Pressure cell (Thermo Electron Corporation). Complete protease inhibitor tablets (Roche Diagnostics) were immediately added to the cell lysate. Cell lysate was clarified via centrifugation and filtration. MBP-INV was purified using a MBPTrap HP (5ml) column on an ÄKTA FPLC system followed by size exclusion chromatography using a HiLoad 16/600 Superdex 200pg column (GE Healthcare). MBP-INV used for particles *in vivo* preparation was only purified using the MBPTrap columns to increase yields. To assess purity, purified protein was heated in loading buffer without DTT and run on a Mini-PROTEAN electrophoresis cell (Bio-Rad) using a 4-15% TGX Gel (Bio-Rad) at 120V until the loading dye ran through the gel.

Invasin Conjugation to Microparticles

Particles were washed once in 50mM 2-(N-morpholino)ethanesulfonic acid (MES) 50mM NaCl 0.005% Triton X-100 pH 5.5 and resuspended to 25mg/ml. Washing

steps for conjugation were facilitated by centrifuging particles at 3,300xg for 5 min. A freshly prepared stock solution of 140 mg/ml in cold MES buffer was added to the microparticle suspension, adjusting the final suspension concentration to 20 mg/ml and an EDC concentration of 28 mg/ml. Carboxylic acid groups on particles were activated for 20 minutes at room temperature while being rotated. After activation, particles were pelleted, supernatant removed, and resuspended to 20 mg/ml in 200mM HEPES 100mM NaCl 0.005% Triton X-100 pH 7.8. Solutions containing the invasin fusion protein (30 mg/ml) in 200 mM HEPES 100mM NaCl pH 7.8 were added to 1:1 to the particle suspensions. The reaction was carried out for 3.5 hours at room temperature while samples were rotated. Particles were then pelleted and resuspended to 10mg/ml in 50mM HEPES 200mM NaCl 40mM hydroxylamine 0.005% Triton X-100 pH 7.5 and incubated with rotation at room temperature for 30 minutes. Samples were then washed once in 5mM HEPES pH 7.5 and resuspended to 10 mg/ml in the same buffer. Samples were frozen in liquid nitrogen and placed on a precooled lyophilizer shelf (-40°C). Samples were lyophilized at -40°C 150 mtorr until visually dry (~48 hours). Samples were then ramped to 25°C over the course of 60 minutes and continued to be dried under vacuum (150 mtorr) until removed (~12 hours).

Scanning Electron Microscopy

Lyophilized particles were deposited on carbon discs placed on aluminum stubs (SPI Supplies). Samples were sputter coated with a 12-15nm Pt/Pd target using a

Cressington 208 Benchtop Sputter Coater. Coated samples were imaged using a Zeiss Supra 40 VP Scanning Electron Microscope (3-5kV).

Dynamic Light Scattering and Zeta Potential

Dynamic light scattering (DLS) was carried out using a Brookhaven ZetaPALS instrument with particle sizing capability. Each sample underwent multiple measurements. The correlation function from each measurement was fitted with CONTIN and the mean percent volume weighted diameter was reported. Zeta potential measurements were made in 0.5 mM KCl using a Brookhaven ZetaPALS instrument. Each sample was measured 10 times and the mean charge was reported, after outlier removal.

Protein Loading

Particles encapsulating ovalbumin were subjected to expedited hydrolysis in 0.1N NaOH, 5% sodium dodecyl sulfate (SDS) at particle concentrations 1-2 mg/ml, accurately weighed. The hydrolysis was carried out for ~16 hours at room temperature with rotation. The protein concentration was measured using a Micro BCA Protein Assay (Pierce, Rockford, IL). Protein standards were prepared by dissolving lyophilized ovalbumin in the hydrolysis solution. Empty microparticles were not significantly different from pure hydrolysis solution.

CpG Loading

After conjugation the amount of CpG DNA was quantified by PLGA particle dissolution in DCM (20 mg/ml) followed by extraction into Tris-EDTA (TE) buffer (2x DCM volume used). The amount of ssDNA present in solution was quantified by generating standards using empty unconjugated particles spiked with known amounts of CpG in the DCM, then analyzed by fluorescence with Quant-iT RIboGreen® RNA assay kit. Standard curve concentrations were made at 0, 1, 5, 10, 25, 50, 100, and 200 ng/ml, based on TE extraction volume. The standard curve was linear and spanned the test sample concentrations. A separate experiment was performed without the addition of empty unconjugated PLGA particles, to measure the interference of the PLGA particles. Fluorescence measurements showed values slightly above 0 ng/ml but below 1 ng/ml CpG DNA.

Flow Cytometry Analysis of Particles

To assess the accessibility of B cell epitopes and activity of MBP-INV on the particle surface flow cytometry was used in conjunction with antibodies (specific for ovalbumin, maltose binding protein (MBP), and/or the D4-D5 region of invasin) or fluorescent $\alpha 5\beta 1$ integrin. 50 µg of particles were labeled for each analysis in 50 µl. Primary antibody labels were incubated for 30 min at room temperature in 50 mM HEPES, 200 mM NaCl, 1% bovine serum albumin (BSA), 0.005% Triton X-100, pH 7.5 at a 1:100 solution: anti-ovalbumin (Santa Cruz Biotechnology, Inc sc-58820), anti-invasin (3A-2)(65) supplied as cell culture supernatant, and anti-MBP (New England

BioLabs, Inc E8032S). Cy5-labeled goat anti-mouse IgG (H+L) (Invitrogen A10524) was used as a secondary antibody also at a 1:100 dilution for 30 min at room temperature. To label the integrin, Alexa Fluor 647 (Invitrogen A20006) was dissolved in acetonitrile at 1mg/ml, aliquoted in 50 μl fractions, dried and stored at -20°C. A 50 ug aliquot of α5β1 integrin (R&D Systems, Inc 3230-A5 Lot OOJ2510121), was adjusted to 1mM sodium bicarbonate and combined with 20 ul dye solution (prepared from 50 ug Alexa Fluor 647 dissolved in 5 μl of dimethylformamide plus 45 μl of 1M sodium bicarbonate). The reaction was allowed to proceed for 1.5 hrs with rotation at room temperature, after which the solution was dialyzed in 50mM HEPES, 200mM NaCl, 2mM MnCl2 pH 7.5 using a 20K MWCO dialysis cassette (Pierce 66005. To prevent photobleaching, all steps involving a fluorophore were carried out in the dark. Particles were labeled with 100 nM concentration of fluorescent α5β1 integrin for 1 hr in 50 mM HEPES, 200mM NaCl, pH 7.5, 2 mM $MnCl_2$, 2% w/v BSA. Particles were washed in between labeling steps by centrifuging at 6,000xg for 2 min. After labeling, particles were resuspended in 1 ml of 50 mM HEPES, 200 mM NaCl, pH 7.5 (w/ 2 mM $MnCl_2$ for integrin labels) prior to analysis on a LSRFortessa (BD Biosciences). Samples were gated by size to isolate the main population using FlowJo (Tree Star, Inc) and greater than 9,000 events are reported for each plot or median fluorescence intensity (MFI).

Simulated Digestion

Simulated gastric and intestinal fluids were prepared as recommended by the U.S. Pharmacopeia for test solutions. Simulated gastric fluid was made by the combining 200

mg NaCl, 225 mg purified porcine pepsin (2,500-3,500 units/mg, Sigma P7012), 700 μl HCl and bringing the solution to 100 ml (pH measured to be 1.36). Simulated instestinal fluid was prepared by combining 680 mg of monobasic potassium phosphate, 7.7 ml 0.2N NaOH, 333 mg of 3XUSP pancreatin (MP Biomedicals 0210255825), pH adjusted to 6.8 and volume to 100ml. Simulated digestions were carried out to mimic *in vivo* dosing conditions, 25 μl particle suspension (10 mg/ml) added to 17 μl gastric test fluid or 33 μl intestinal fluid and incubated at 37°C with shaking for 75 min. After digestion, samples were washed with PBS and prepared for flow cytometry analysis described above.

In Vitro Costimulation

To measure upregulation of activation markers on professional antigen presenting cells, PLGA particles were incubated with RAW 264.7 macrophage cells. $1x10^6$ cells/well were seeded 6-well plates with 1.5ml Dulbeccco's Modified Eagles Medium (DMEM) supplemented with 10% fetal bovine serum (FBS) and grown at 37°C in 5% CO_2. The next day, media was exchanged and samples were added to wells for overnight incubation. The following day, cells were trypsinized and counted using a hemacytometer. $1x10^6$ cells were centrifuged at 500xg for 5 min and media was aspirated. Cells were then labeled with 1:100 dilutions of APC rat anti-mouse CD40 (BD Biosciences 558695) and FITC rat anti-mouse CD86 (eBiosciences 11-0862-81) in 100 μl PBS with 1% FBS for 30 min at room temperature in the dark. Cells were then pelleted

114

and resuspended in 1 ml PBS 1% FBS for flow cytometry analysis on a FACSCalibur (BD Biosciences), followed by FlowJo analysis (Tree Star, Inc).

Immunological Animal Studies

Female C57Bl/6 mice 6-8 weeks of age were purchased from Jackson Laboratories and cared for under approved The University of Texas at Austin Institutional Animal Care and Use Committee (IACUC AUP-2009-00086). All mice were deprived of food for 6-8 hours before dosing. Subcutaneous Alum-adjuvanted controls were dosed by injection of 100 µg of OVA mixed with alum in 100 µl. Oral dosing carried out by 250 µl oral gavage using a blunt-tip feeding needle. The carrier solution was 5% sodium bicarbonate and 5% bovine serum albumin (BSA), which the naïve group received. All other doses were adjusted such that 100 µg of OVA was dosed. Serum samples were prepared from blood collected from the tail via venipuncture technique.

Serum Sample Analysis

Serum samples were analyzed for presence of antigen specific antibodies via ELISA. The ELISAs were performed by coating 96 well plates with either ovalbumin (10 ug/ml) or maltose binding protein (5 ug/ml) by overnight incubation in a 50 mM carbonate buffer (pH 9.5) at 4°C. The plates were then washed and blocked in 3% fetal bovine serum (FBS), 3% bovine serum albumin (BSA), 0.05% Tween-20 in PBS overnight at 4°C. Each wash step consisted of four washes in PBS plus 0.05% Tween-20 (PBST). Serum samples were diluted as stated in the results section in PBST plus 3% FBS, 3% BSA for 1.5 hours at room temperature. Plates were then washed in PBST and incubated with a goat anti-mouse IgG (subclasses I+2a+2b+3), Fcγ fragment specific

(Jackson ImmunoResearch Laboratories, Inc. 115-035-164) for 1 hour at room temperature. Plates were then washed in PBST, followed by a PBS wash. Signal was developed using Pierce 1-Step Ultra TMB and was quenched after 15 minutes with 1N HCl. Absorbance at 450 nm was measured by a SpectraMax M5 plate reader.

Chapter 4: In Vivo Imaging Oral Vaccine Delivery System

INTRODUCTION

Semiconductor nanocrystal quantum dots can exhibit bright and stable fluorescence that can be tuned over a wide wavelength range by changing size and composition from visible to near-infrared (NIR) wavelengths. They have been explored for use in light-emitting diodes(159, 160), photovoltaics(161-163), and as fluorescent probes for bioimaging (164-166). Nanocrystals with NIR optical properties are especially of interest for biological applications, due to the relatively strong light absorption by tissue and water outside the 650-900nm spectral window (167). In addition, nanocrystals offer a wide excitation band compared to molecular dyes, which can be useful for multispectral imaging (168, 169). Recently, $Cu_{2-x}Se$ nanocrystals were synthesized with strong NIR absorbance due to a plasmonic resonance and demonstrated their potential for photothermal therapy (170).

We report the synthesis of copper indium sulfide-selenide (CISS; $CuInS_xSe_{2-X}$) quantum dots with size-tunable photoluminescence across visible to near-infrared (NIR) wavelengths with high quantum yield. NIR-emitting nanocrystals have been made, including binary compounds, such as lead chalcogenides(171, 172), CdTe(173), InAs(174), and Cd_3As_2(175), ternary and quaternary nanocrystals of $Cu(In_xGa_{1-x})Se_2$(162), $CuInS_2$, $CuInSe_2$(176), Cu_2ZnSnS_4(177) and NIR photoluminescence has been reported in I-III-VI ordered vacancy compound nanocrystals (178), and ZnS-coated chalcopyrite $CuInS_2$ (179). Tuan and coworkers synthesized CISS nanocrystals in gram scale quantities(180), however they did not observe photoluminescence in their study due

to the large size (>10 nm) of the particles synthesized in their study. Here, we utilize CISS nanocrystals with size-dependent photoluminescence in the visible to NIR and test their potential for use as a fluorescent probe for in vivo biological imaging. 2.4 nm diameter CISS nanocrystals were encapsulated in poly(lactic-co-glycolic acid) (PLGA) microparticles (0.5 - 2.0um) with an invasin protein coating to facilitate mucosal vaccine delivery. To our knowledge, this is the first report of cell-targeted optical imaging using fluorescent nanocrystals via oral delivery.

The band gap energy of CISS varies between 1.0 eV for x = 0 and 1.5 eV for x = 2.25 CISS nanocrystals should have tunable emission peaks from visible to NIR wavelengths by changing size and composition. Room-temperature photoluminescence is rarely observed from bulk CISS or other ternary I-III-VI compounds due to nonradiative recombination at defects (181). CISS is also attractive for in vivo biological imaging because it does not have toxic heavy metals (such as Cd, Pb, Hg, or As) and can be tuned to emit in the red/NIR transparent window of biological tissue.

RESULTS AND DISCUSSION

CISS nanoparticle synthesis and characterization

$CuInS_XSe_{2-}X$ nanocrystals were synthesized by arrested precipitation in hot octadecene with dodecanethiol serving as both a capping ligand and sulfur source. Tributylphosphine selenide (TBP:Se) was injected at 180°C to induce nucleation. Figure 4.1 shows TEM images of CISS nanocrystals isolated from the reaction after different times. The nanocrystals become progressively larger with increasing reaction time.

Particle size measured by small angle x-ray scattering ranged from 1.7 to 2.4 nm for reaction times of 5 and 90 minutes, respectively. After about 30 minutes, the particles increase in polydispersity, with a polydisperisity of 40% measured by small angle x-ray scattering. The lattice spacing in the CISS nanocrystals determined from high resolution TEM images are consistent with a sphalerite (cubic) crystal structure and a ~1:1 S:Se ratio. XRD (Figure 4.2) is consistent with sphalerite CISS and no other phases are present in the reaction product. Typically, CuInSe2 and CuInS2 have a chalcopyrite (tetragonal) crystal structure; however, peaks at ~17° and 35° corresponding to the (101) and (211) lattice planes are not observed. The sphalerite (111) peak lies between where the (112) peaks for chalcopyrite copper indium selenide and copper indium sulfide would be (JCPDS #97-006-892, 082-1702). This indicates that the nanocrystals are an alloy of the two. The average Cu:In:S:Se composition determined from EDS of fields of nanocrystals was 1.0:1.0:1.3.0.7. There was no significant compositional variation between areas on the TEM grid within the error of the EDS detector. Additionally, the nanocrystal composition did not change as a function of reaction time between 15 and 90 minutes. However, when the growth temperature was reduced to 200°C or less, the nanocrystals became richer in Se, indicating a lower reactivity of dodecanethiol as a sulfur source relative to the TBP:Se. These nanocrystals made at lower temperature exhibited significantly lower photoluminescence quantum yield. Overcoating with a thin layer of ZnS resulted in a 4x increase of PL quantum yield that was stable in air for several months.
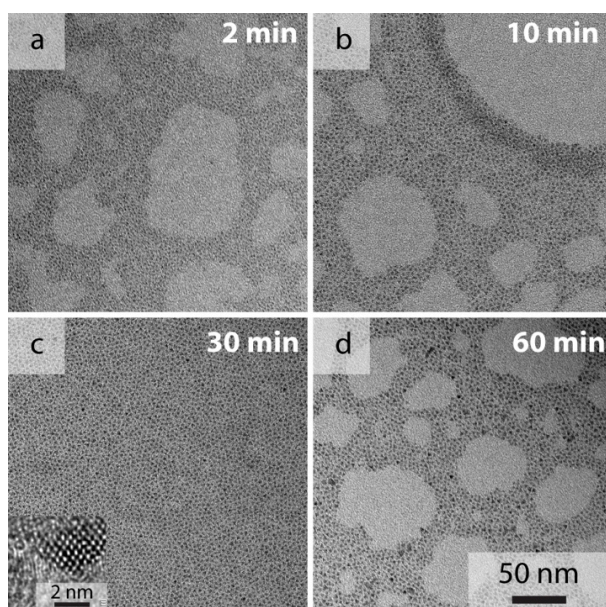
Figure 4.1: TEM of CISS nanocrystals after (A) 2 min, (B) 10 min, (C) 30 min, and (D) 1 hour of growth. Inset in (C): high resolution TEM image of a CISS nanocrystal.
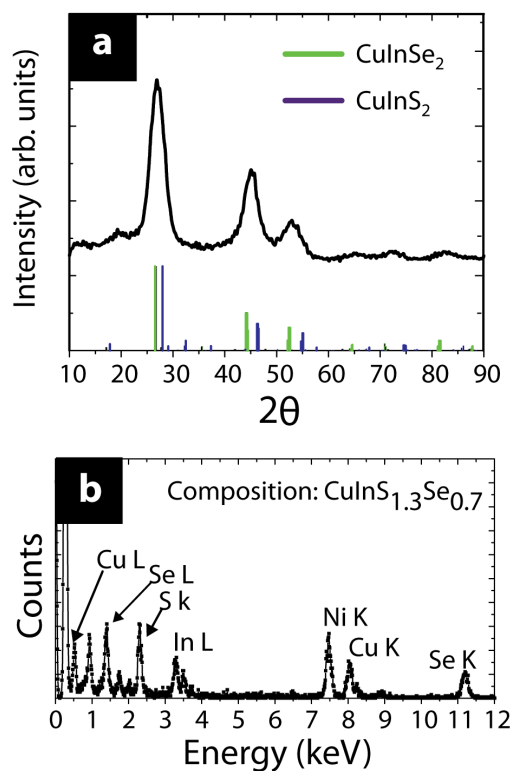
Figure 4.2: XRD and EDS Spectrum of CISS Nanocrystals. (A) XRD and (B) EDS Spectrum.

Absorbance and PL measurements (Figure 4.3) show evidence of quantum confinement in the CISS nanocrystals. Nanocrystals isolated immediately after TBP:Se injection (0 min) exhibited an absorbance shoulder at approximately 380 nm and weak PL at 610 nm (QY < 0.01%). As the reaction proceeds and the CISS nanocrystals grow, the absorbance shoulder and PL redshift. After 90 minutes of particle growth, the exciton peak occurs at ~650 nm and the PL peak at 765 nm. Bulk CISS with the composition calculated by EDS would have band gap of about 1.2 eV (1,030 nm). This indicates that even after 90 minutes of growth time, the nanocrystals exhibit quantum confinement effects, with a size of 2.4 nm.
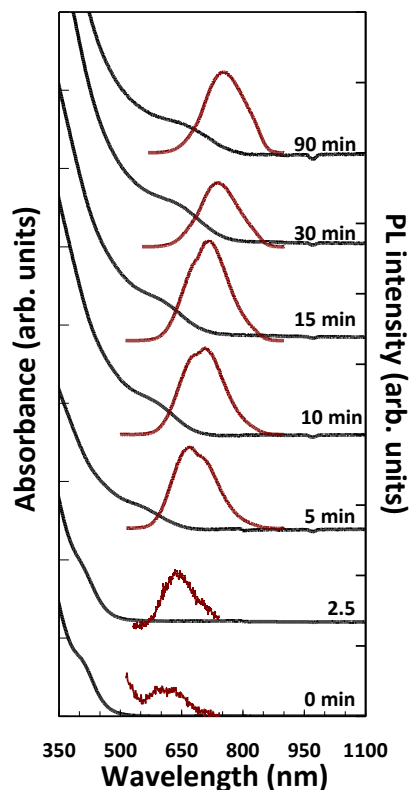
Figure 4.3: Absorbance and PL spectra of CISS nanocrystals. For PL measurements, an excitation wavelength of 400 nm was used. At 5, 15, 30, and 90 minutes the particle diameter measured by small angle x-ray scattering was 1.7±0.5, 1.9±.6, 2.0±.8, and 2.4±1.0 nm.

121

CISS nanoparticle encapsulation in invasin decorated PLGA microparticles

      CISS nanocrystals were integrated into a microparticle-based oral vaccine system to demonstrate biological imaging in deep tissue. Previous work has shown that the bacterial protein invasin, from *Y. pseudotuberculosis*, has the ability to target intestinal M cells, which play a critical role in gut immunity (57, 79). These M cells exist as a small fraction of cells along the gastrointestinal (GI) tract, occurring on the order of 1 in 10,000,000 enterocytes (15). M cells act as a gut portal to the immune system by sampling material (i.e. protein, bacteria, viruses, food, etc). These cells take material in the intestinal lumen and deliver it to lymphocytes residing in the lamina propia. Since a major limitation to successful oral subunit vaccines is delivery of key pathogen components to lymphocytes, the ability to target these M cells has been shown to play an essential role in developing a feasible platform oral vaccine delivery system (40, 42, 90, 93). A single amino acid substitution on the surface of invasin, D911A, leads to loss in binding of invasin for its receptor, $\alpha5\beta1$ (68). In this study we tested the targeting ability of an invasin-functionalized vaccine delivery system. Fluorescent CISS nanocrystals were encapsulated in poly (lactic-co-glycolic) acid microparticles as a label for whole animal fluorescent imaging. The nanocrystals were encapsulated in PLGA microparticles by addition to the oil phase of a Water-in-Oil-in-Water emulsion used to produce the microparticles. Figure 4.4 shows SEM and fluorescence microscopy of the CISS nanocrystal-loaded microparticles. The microparticles range in diameter from 500 to 2,000 nm. The microparticles are fluorescent, confirming that the CISS nanocrystals are encapsulated.
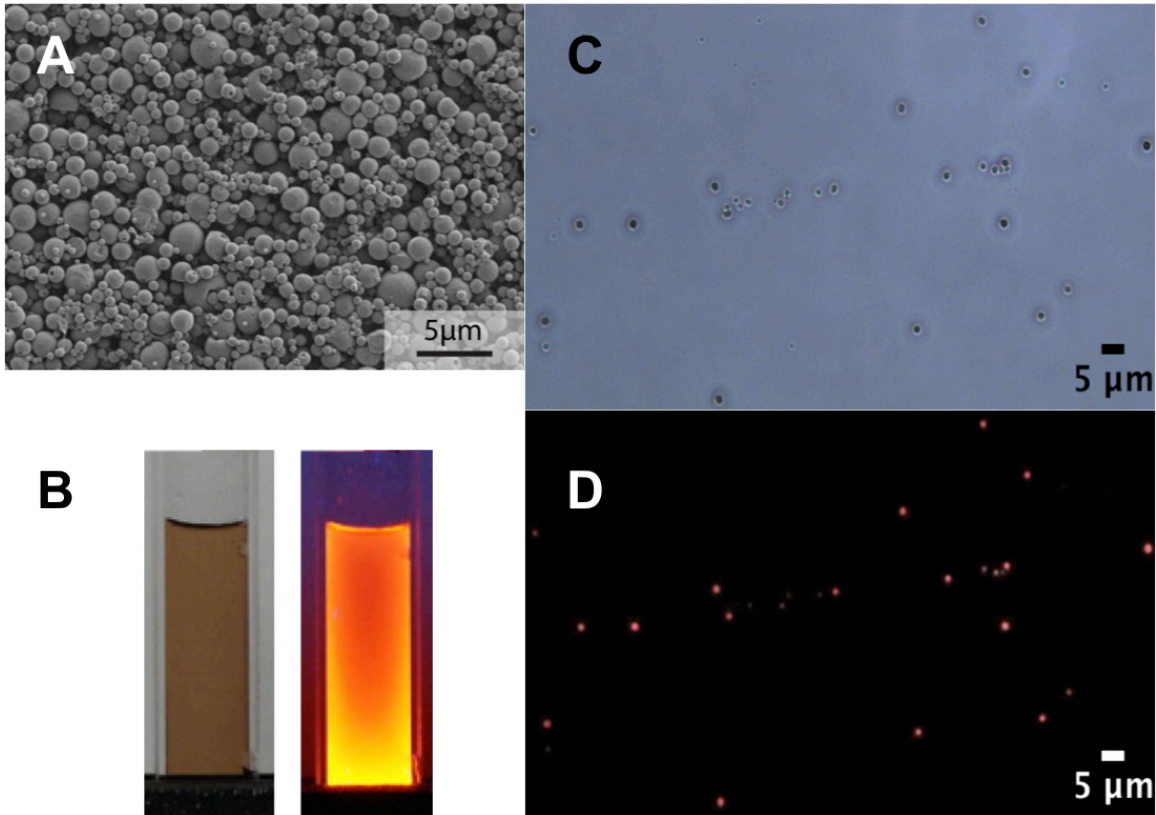
Figure 4.4: In vitro CISS nanoparticle fluorescence before and after encapsulation in PLGA micropartilces. (A) SEM images and (B) Photographs showing dispersions of ZnS@CISS nanocrystals in cuvettes before encapsulation in room light (left) and under a fluorescent lamp (right). (C) Bright field and (D) fluorescence microscopy images of CISS nanocrystal-loaded PLGA microparticles. Fluorescence image taken with excitation 480-550 nm and emission >590 nm.

In vivo imaging of CISS loaded invasin decorated PLGA microparticles

Two sample groups were tested: 1) microparticles conjugated to the extracellular portion of wild-type invasin expressed as a fusion protein on the C-terminus of maltose binding protein (MBP), 2) microparticles conjugated to the same protein with the D911A substitution. A schematic illustrating the experimental process is shown in Figure 4.5.
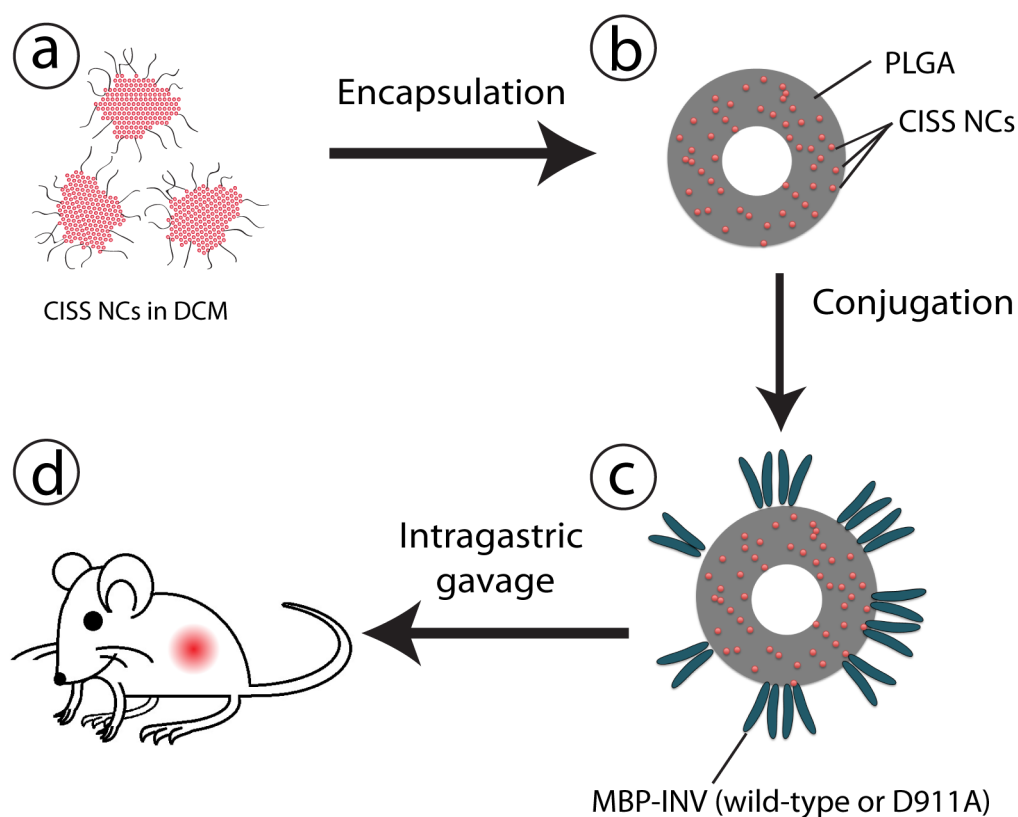
Figure 4.5: Schematic of *in vivo* fluorescence imaging of CISS loaded targeted PLGA microparticles. CISS NCs dispersed in dichloromethane (DCM) (A) are encapsulated in PLGA microspheres (B). The microparticles are conjugated to either wild-type invasin or the protein with a single amino acid substitution (D911A) (C). After intragastric gavage, the in-vivo fluorescence is monitored using an IVIS Spectrum (D).

The invasin functionalized PLGA microparticles encapsulating the CISS nanocrystals (InvaCISS) were orally gavaged to mice and imaged, using a non-invasive Caliper Life Sciences IVIS Spectrum, to track the time-dependent fluorescence retention in the GI tract. The fluorescence should correlate to M cell uptake, as within the GI tract only M cells are known to be capable of transcytosis of particles in the microparticle size range. Figure 4.6 shows whole-animal fluorescence images of mice fed InvaCISS.

	15 min	18 h	45 h	intestines (48 h)
Control (D911A)	a	b	c	d
Wild-type	e	f	g	h
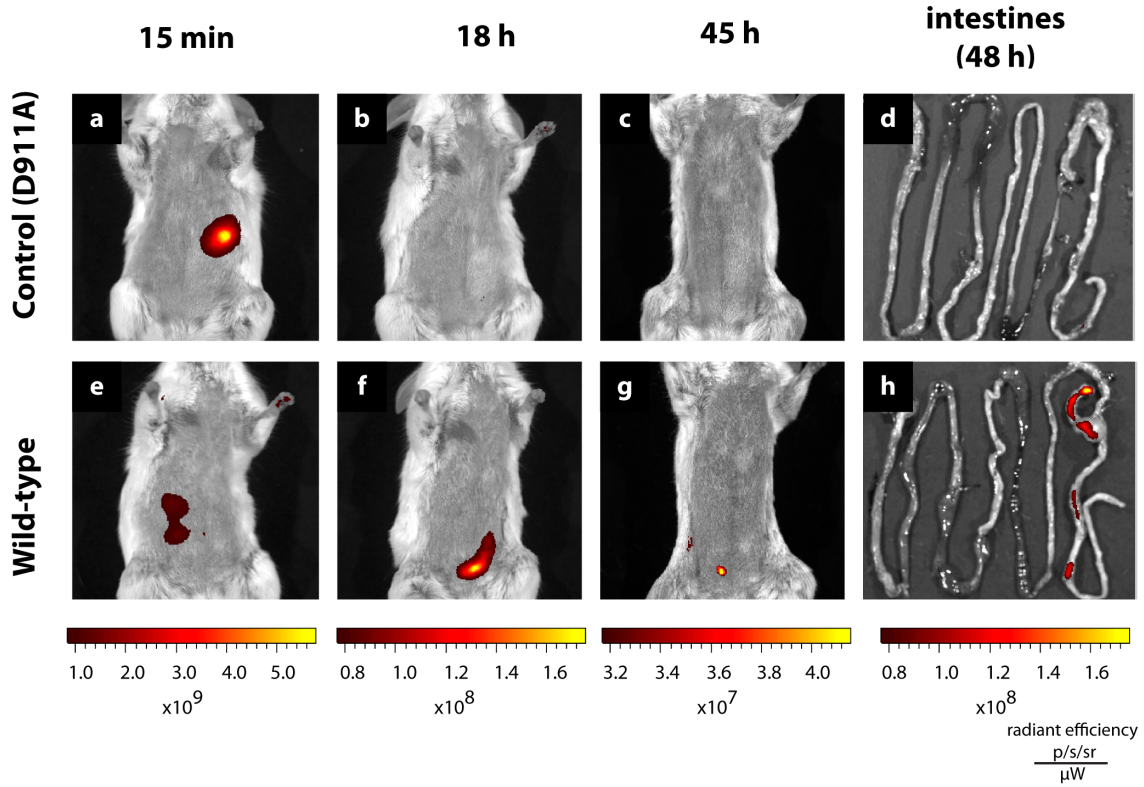
Figure 4.6: In-vivo Fluorescence Imaging. Same subjects tracked at 15 min (A, E), 18 hours (B, F), 45 hours (C, G) after oral gavage and the intestines after dissection at 48 hours (D, H). Mice were administered CISS nanocrystal-loaded PLGA microparticles conjugated with (E-H) wild type invasin-MBP fusion protein or (A-D) the same protein with the D911A substitution abrogating the targeting ability.

The fluorescent CISS nanocrystals were clearly visible in the whole-animal images and identified the location of the microparticles *in vivo*. At 15 minutes, any material orally gavaged would be primarily found in the stomach, as the exponential decay constant of stomach emptying in the mouse is 72 minutes (182). The fluorescence signal in figures 4.6 (a) and (e) is located where the stomach should be located. At 18 and 45 hours, the majority of ingested material that is not mucoadhesive or transported across

the intestinal wall is expected to be excreted. Figure 4.6 (h) shows the fluorescence signal is restricted to the cecum and the colon. In mice, M cells are found along the GI tract in Peyer's patches in the distal small intestine, isolated lymphoid follicles, cecal patches, and colonic patches (145). The greatest amount of microparticles appears to associate with the cecal M cells. Quantatative analysis was performed by integrating the fluorescence intensity over a region of interest (ROI) using multiple filter sets (Figure 4.7). The ROI encompassed the entire abdomen. For images with weaker signals (18 hrs, 45 hrs, intestines), the images were spectrally unmixed using Living Image 4.0 to distinguish tissue autofluorescence from nanocrystal fluorescence.
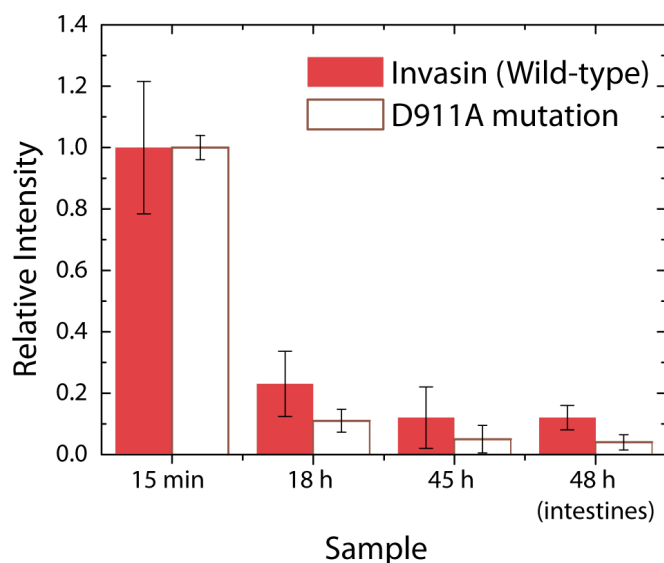
Figure 4.7: Comparison of fluorescence signal from the nanocrystals at 15 min, 18 hours, 45 hours in vivo, and the intestines at 48 hours post-mortem. Error bars correspond to the standard deviation of measurements of multiple mice for each experiment.

CONCLUSIONS

CISS nanocrystal quantum dots with size-dependent, bright PL were synthesized. The initial PL quantum yield of the as-synthesized CISS particles was around 10% and increased to 40% after overgrowth of a ZnS shell. This ZnS shell was also found to be very important for stabilizing the PL in aqueous media. These nanocrystals do not contain toxic heavy metals and emit in the red/NIR wavelength range, making them attractive for medical imaging. We demonstrate in vivo whole animal fluorescence imaging of the microparticles loaded with CISS nanocrystals in deep tissue, within the GI tract. The CISS nanocrystals are promising new materials as a biocompatible diagnostic agent.

MATERIALS AND METHODS

Materials

All chemicals were used as received. Copper (II) acetylacetonate (Cu(acac)$_2$; 99.99+%) and indium (III) acetylacetonate (In(acac)$_3$, 99.99+%), 1-octadecene (ODE, 90%), dodecanethiol (DDT, 98%), selenium powder (99.99%), potassium ethyl xanthogenate (96%), zinc (II) oleate (90%) and tributylphosphine (TBP, 98%) were purchased from Aldrich Chemical Co. Cu(acac)$_2$, In(acac)$_3$, and DDT were stored in a dessicator. Ethanol (absolute), toluene (spectrophotometric grade, 99+%), and isopropanol (≥99%) were purchased from Fisher Scientific. TBP was stored in a N$_2$-filled glovebox. Stock solution of 1M tributylphosphine selenide (TBP:Se) was prepared by dissolving 10 mmol of Se powder (790 mg) in 10 mL TBP inside a N$_2$-filled glovebox. Zinc bis(ethylxanthogenate) was prepared by a method described by Li et al (183). Acid

end-capped PLGA, Resomer RG502H, was purchased from Boehringer Ingelheim. Poly (ethylene-alt-maleic anhydride) was obtained from Polysciences, Inc. α,α-Trehalose, Dihydrate was from J.T. Baker. 1-Ethyl-3-[3-dimethylaminopropyl]carbodiimide hydrochloride (EDC) and N-hydroxysulfosuccinimide (Sulfo-NHS) were from Thermo Scientific Pierce. LB broth (Miller), terrific broth, ampicillin, chloramphenicol, kanamycin, tetracycline, D-glucose, HEPES, MES, NaCl, and Isopropyl-b-D-thiogalactopyranoside (IPTG) were obtained from Fisher Scientific.

Synthesis of CISS nanocrystals

In a typical reaction, 5 mmol $Cu(acac)_2$ (1.3g), 5 mmol $In(acac)_3$ (2.5 g), 20 mL ODE and 10 mL DDT are placed in a 100 mL 3-neck round bottom flask equipped with a magnetic stir bar. The flask is connected to a condenser and sealed with rubber septa. A thermocouple is inserted through one septum to measure the solution temperature. The flask is attached to a Schlenk line and is heated with a heating mantle. The contents are first put under vacuum (~300 mTorr) and heated to 110ºC for 1 hr while stirring. The dispersion, which is initially blue and opaque, transforms into a transparent yellow, viscous solution as it is heated. After 1 hr, the solution ceases to bubble, indicating that all moisture is removed and the flask is thoroughly degassed. The flask is then put under a N_2 atmosphere and the temperature is quickly ramped to 180ºC, where immediately 10 mL of 1M TBP:Se is injected rapidly. Upon injection the temperature drops to ~160 ºC and the flask contents becomes almost colorless. The temperature is then ramped to 220ºC, and aliquots are taken along the course of the reaction. Reaction temperatures over 240ºC lead to uncontrolled growth, with a final product containing mostly large

precipitates with no observed photoluminescence. The solution color is initially pale yellow, and as time goes on the color progresses from yellow to orange, red, and finally dark brown. Aliquots were taken to monitor the photoluminescence peak. The photoluminescent quantum yield of these aliquots were typically between 5 and 10%. A ZnS shell precursor solution was prepared by combining zinc bis(ethyl xanthogenate) (100 mg), zinc (II) oleate (900 mg). ODE (10 mL), trioctylphosphine (3 mL) and oleylamine (1 mL). The CISS nanocrystals are coated with ZnS by cooling the reaction solution to 190ºC and injecting this solution into the reaction flask. The mixture is stirred overnight to allow the shell to form. The heating mantle is removed and the mixture is allowed to cool to room temperature. The nanocrystals are precipitated by adding an ethanol/toluene (~2:1 vol:vol) mixture and centrifuging at 8,000 rpm for 5 min. Addition of only ethanol as an antisolvent is not effective because ethanol is not miscible in octadecene, and the mixture phase segregates. The nanocrystals are further purified by redispersing in toluene and precipitating with a minimal amount of ethanol or isopropanol and centrifuging.

Nanocrystal Characterization

The nanocrystals were characterized using a range of analytical techniques, including transmission electron microscopy (TEM), energy-dispersive X-ray spectroscopy (EDS), X-ray diffraction (XRD), small angle x-ray scattering (SAXS), UV−vis−NIR absorbance spectroscopy and photoluminescence (PL) spectroscopy.

TEM imaging was performed on nanocrystals drop-cast from toluene dispersions on carbon-coated 200 mesh copper or nickel TEM grids (Electron Microscopy Sciences).

TEM images were acquired on either a FEI Technai G20 TEM with 80 kV accelerating voltage or a JEOL 2010F TEM operating at 200 keV. The JEOL 2010F TEM is equipped with an Oxford INCA EDS detector, which was used to collect EDS data.

XRD data was acquired using a Bruker-Nonius D8 Advance θ–2θ Powder Diffractometer equipped with a Bruker Sol-X Si(Li) solid-state detector and a rotating stage. Cu Kα (λ= 1.54 Å) radiation was used. For XRD, the nanocrystals were evaporated from concentrated dispersions onto quartz (0001) substrates as ~0.5 mm thick films. Diffraction data was collected by scanning for 4 to 12 hrs with an angle increment of 0.01° or 0.02° at a scan rate of 6°/min and a rotation speed of 15 rpm.

UV−vis−NIR absorbance spectra were obtained with a Varian Cary 500 UV−vis−NIR spectrophotometer using hexane-dispersed nanocrystals in a quartz cuvette.

CISS Nanocrystal Encapsulation in PLGA Microparticles

Poly (ethylene-alt-maleic anhydride) was hydrolyzed to poly (ethylene-alt-maleic acid) (PEMA) by slow addition to heated double-distilled H2O (ddH2O) (~80 ℃) with the addition of NaOH. The final solution was adjusted to 1% w/v PEMA and pH 7.5, then filtered through a 0.22um bottle top filter. Microparticles were prepared using a modification of a previously described protocols (7, 133). Briefly, 2 batches of 350mg Resomer RG502H and 55mg of CISS nanocrystals were solubilized/dispersed in 8ml of methylene chloride. 300ul of ddH2O was added and the emulsion was homogenized at ~10,500 RPM for 2 minutes using a Silverson SL2T Homogenizer. This emulsion was immediately added to 50ml of a 1% w/v solution of PEMA and homogenized again for 2 minutes at ~10,500 RPM. The Water-in-Oil-in-Water emulsion was then added to 100ml

of 1% w/v PEMA solution and stirred for 3 hrs. The hardened microparticles were washed 3x in ddH2O. During the last wash step the 2 batches were combined then resuspended in ~3ml ddH2O, frozen in liquid nitrogen, and lyophilized on an external manifold of a VirTis Advantage Plus Benchtop Freeze Dryer for ~48 hrs.

Production/Purification of Soluble Invasin

Maltose Binding Protein/Invasin (MBP-INV) fusion proteins were expressed using the pMAL-c5x (New England Biolabs) vector, similar to one used previously (Leong, 1995). The C-terminal 497 amino acids of invasin from *Yersinia* pseudotuberculosis was PCR amplified using the primers TAK046 (agctatcgagctcgaactcattcacattgagcgtc) and TAK047 (cgtcattataccatggctagttaatcattatattgacagcgcacagag) and cloned into pMAL-c5x using the restriction sites SacI and NcoI. The cytoplasmic fusion protein was co-expressed with a cytoplasmic version of the skp chaperone on a separate expression vector, pAR3-Skp in Origami B (EMD Chemicals) (121). Starter cultures were grown in 4 ml of LB with Ampicillin (150 ug/ml), Chloramphenicol (34 ug/ml), Kanamycin (15 ug/ml), Tetracycline (12.5 ug/ml) and shaken at 37°C and 225 RPM. Approximately 16 hours later, 3.5 ml of the starter cultures were inoculated into 500ml of Terrific Broth (TB) containing the same antibiotics plus 2% D-glucose and shaken at 37ºC and 225 RPM. Approximately 16 hrs later, the cells were harvested and resuspended in fresh TB with antibiotics, but no glucose and shaken at 25ºC and 225 RPM. 30 minutes after resuspension, L-arabinose was added to a final concentration of 0.2% w/v. 30 minutes after the addition of L-arabinose, IPTG was added to a final concentration of 1 mM.

131

Expression was carried out at 25ºC for 4 hrs. Cells were then harvested and frozen at -80ºC. Harvested cell pellets were resuspended and lysed via a French Pressure cell. Complete protease inhibitor tablets (Roche Diagnostics) were immediately added to the cell lysate. Cell lysate was clarified via centrifugation and filtration. MBP-INV was purified using a MBPTrap HP (5ml) column on an ÄKTA FPLC system followed by size exclusion chromatography using a Superdex 200 10/300 GL column (GE Healthcare).

Conjugation of MBP/INV to PLGA Microparticles Encapsulating CISS Nanocrystals

420 mg of PLGA microparticles encapsulating CISS nanocrystals were resuspended in 16.8 ml of 0.1 M MES buffer 0.5M NaCl (pH 5.0). 100 ul ddH2O containing 280 mg of EDC and 100ul ddH2O containing 320 mg of Sulfo-NHS were added to the microparticle suspension. The reaction was rotated for 2 hrs at room temperature. After activation, the 2x8ml of the suspension were transferred to new 50 ml conicals. 200 mM HEPES 200 mM NaCl pH 7.4 was added to 50 ml and the microparticles were pelleted. The activated microparticles were resuspended with 10 ml of 200 mM HEPES 200 mM NaCl pH 7.4. 10ml of the same buffer containing 10 mg of the respective MBP-INV variant, wild-type or D911A, was added to the microparticles and rotated for 2 hrs at room temperature. The microparticles were then washed twice in 10 mM HEPES 50 mM NaCl pH 7.4 and resuspended in 3 ml ddH2O containing 20 mg of α,α-Trehalose. The samples were frozen in liquid nitrogen lyophilized as before.

In Vivo Fluorescent Imaging

6-8 week old female albino (BALB/c) mice were purchased from Jackson Laboratories and housed in at the Animal Resource Center, The University of Texas at Austin, in accordance with Institutional Animal Care and Use Committee (IACUC) Guidelines. The mice received an alfalfa free diet (2019 Tekland Global 19% Protein Extruded Rodent Diet) for 7 days prior to commencement of the study in order to reduce intestinal autofluorescence, and were maintained on this diet throughout the duration of the study. Mice were fasted for 3 hrs prior to dosing. 15 mg of microparticles were dosed in 200 ul 5% w/v sodium bicarbonate via intragastric gavage (3 mice per sample group). Immediately after dosing, the subjects were anesthetized in an incubation chamber with 3% isoflurane. The subjects were transferred to an IVIS Spectrum (Caliper Life Sciences) and anesthesia was maintained using 1% isoflurane during imaging. Imaging was carried out using epifluorescence with 14 filter sets for subsequent autofluorescence subtraction. After imaging, the subjects were placed back into conventional housing with food and water ad libitum. Mice were imaged again at 18 hours post-dose under the same conditions. After 45 hrs post-dose, the mice were sacrificed, imaged, then the intestines were removed for further imaging.

Analysis of Fluorescence Imaging Data

For the 15 min time point, the signal-to-noise ratio was sufficiently intense enough that autofluorescence subtraction was unnecessary and the samples were analyzed with the highest contrast filter set (640nm/760nm). For all subsequent time points spectral unmixing was carried out to extract the nanocrystal fluorescence from tissue

autofluorescence using Living Image 4.0 (Caliper Life Science). For whole animal images, the following excitation/emission filter sets were used: 570nm/700nm, 605nm/720nm, 605nm/740nm, 605nm/760nm, 605nm/780nm, 605nm/800nm, 640nm/700nm, 640nm/720nm, 640nm/740nm, 640nm/760nm, 640nm/780nm, and 640nm/800nm. The samples were unmixed using a two fluorophore setting: tissue autofluorescence set to "Auto" and Fixed, nanocrystal fluorescence set to "AF750Ex", an internal spectrum standard which matched well with our nanocrystal fluorescence spectrum. Regions of Interest (ROIs) were drawn around the abdominal area (supporting info). Total Radiant Efficiency [p/sμW-1cm^2] was reported. For intestinal images a three fluorophore setting was used to additionally subtract the stage fluorescence. The previous filter sets were used plus the addition of 570nm/800nm. Note: the D911A sample 3 was not used for analysis as the initial image showed substantial fluorescence around the mouth, relative to the stomach, that may have been slowly ingested, thereby altering later relative fluorescence comparisons.

The PL quantum yield (QY) of the CISS nanocrystals was calculated by comparing the PL spectra to that of fluorescein (QY = 1). The nanocrystal quantum yield (QYNC) was calculated by the following formula:

$$QY_{NC} = \frac{A_{std|exc} \int \frac{I_{NC}}{E} dE}{A_{NC|exc} \int \frac{I_{std}}{E} dE} \frac{n_{solvent,NC}^2}{n_{solvent,std}^2} QY_{std}$$

where A_i are the values of absorbance at the excitation wavelength, I_i are the intensities of the photoluminescence as a function of energy, E is energy, n_i are the dielectric constants of the solvents. The denotations *NC* and *std* refer to nanocrystal and fluorescein standard

values, respectively. The CISS nanocrystals, PL quantum yields of up to 40% were recorded.

Chapter 5: High Dose Subcutaneous Delivery of a Protein Therapeutics

INTRODUCTION

Monoclonal antibodies have generated considerable interest as therapeutics because they specifically target distinct antigens with favorable pharmacokinetic, production, and safety profiles. Currently, 29 monoclonal antibodies have received FDA approval for treatment of a wide variety of diseases, commanding an annual market size of over $20 billion dollars (184, 185). Despite advances in protein drug development which allow tailoring of key biophysical properties, such as solubility(186), stability(187), and binding affinity(188) via recombinant DNA techniques, few options have been developed to deliver these macromolecules at desired dosages (>2 mg antibody/ kg body weight). Typically, large volumes of dilute protein solutions are delivered intravenously to avoid the chemical and physical destabilization and resulting loss in protein activity commonly associated with high concentration formulations (189, 190). For instance, Rituxan doses of 100-500 mg are currently administered by intravenous infusion of a 10 mg/ml solution (191). Self-administered subcutaneous injections offer several major advantages over intravenous infusion, including increased accessibility and patient compliance, along with reduced pain and cost. However, the required therapeutic dosages indicate protein concentrations in excess of 100 mg/ml, given the maximum subcutaneous injection volume of 1.5 ml (192, 193).

Formulation of therapeutic proteins at these high concentrations is intrinsically difficult, demanding solutions customized for each new product. Frequently, it is not possible due to low protein solubility (186, 194), protein instability(195-197), and high

solution viscosity(190, 198, 199) resulting from short-range attractive protein-protein interactions. These interactions, which include hydrophobic interactions, hydrogen bonds and fluctuating charge dipoles (199), act over distances up to ~1 nm (200). At high protein concentrations (over 150 mg/ml), the average separation distance between individual antibody molecules is reduced to less than 10 nm (201). Thus, the probability that two protein molecules will be less than 1 nm apart is high and the effect of the short-range attractive interactions between protein molecules becomes significant (201). This leads to concentration-dependent formation of reversible and irreversible aggregates with potential adverse effects on protein activity, pharmacokinetics and immunogenicity. Most troubling are irreversible aggregates, high molecular weight aggregates comprised of monomers with altered structure and reduced activity, which can lead to a turbid solution or even protein precipitation. The formation of these aggregates is protein specific(202) and can form through physical mechanisms, such as partially unfolded monomers with exposed hydrophobic residues(203) or chemical mechanisms, such as formation of intermolecular bonds mediated by reactive thiols on cysteine or methionine residues (204).

Protein structure and activity in low viscosity formulations can be preserved at high protein concentrations by minimizing the effects of these short-range interactions. For example, concentrated suspensions of protein microparticles in water-insoluble organic solvents(205) and aqueous suspensions of protein crystals(190) with low viscosity have been reported. These formulations succeed by using micron-sized (5-20 μm) particles of proteins as opposed to protein monomers, thus increasing the average

distance between protein particles for a given protein concentration. However, formulations of proteins in organic solvents are not desirable as they require large-bore needles and can result in inflammation at the injection site (206). In addition, while highly concentrated aqueous suspensions of crystalline insulin have a history of clinical use (206), it is challenging to routinely crystallize large protein molecules such as immunoglobulins due to their high molecular weight, surface oligosaccharides, and segmental flexibility (190, 207). Similarly, controlled release formulations in which proteins are encapsulated in polymeric matrices with non-aqueous(208) or aqueous media(209-212) have also been explored. In these cases, the low levels of protein within the particle (~15-20 mass%) result in a low deliverable dose even at high particle volume fractions (127). Moreover, most polymeric delivery systems suffer from challenges related to sterility, protein stability, incomplete protein release, and increased immunogenicity (6, 24, 213).

We recently reported a novel approach to preserve protein activity at high concentrations with low viscosity, via concentrated dispersions of nanoclusters, readily reversible particles (30-500 nm) composed of amorphous antibody molecules (201). In that work, lyophilized monoclonal murine or polyclonal sheep antibody was resuspended in buffer containing trehalose as a "crowder" molecule that occupies a large volume and increases the short-range protein-protein attractive interactions (201). Consequently, most of the protein molecules are concentrated into densely packed equilibrium nanoclusters, ~80-300 nm in diameter, depending on the trehalose concentration used (201). A possible mechanism of nanocluster formation and stabilization was explained in terms of specific

short-ranged attraction, van der Waals and depletion attraction forces balanced against weak electrostatic repulsion to result in a colloidally stable protein nanocluster dispersion of discrete size and low viscosity (201). This hierarchy of attractive and repulsive interactions provides one possible explanation for the colloidally stable protein nanocluster dispersions with low viscosity that were observed experimentally (201). In addition, it was hypothesized that the high volume fraction of protein within the nanoclusters, much higher than is possible with a uniform protein solution, helped to maintain the native protein structure due to a self-crowding, entropic stabilizing mechanism (214, 215). Remarkably, nanocluster formation did not detectably alter the structure, antigen binding activity or in vivo pharmacokinetics of a monoclonal antibody.

While promising, formation of therapeutic protein nanoclusters has only been reported using standard bulk freezing prior to lyophilization followed by resuspension in dispersion buffer with a single extrinisic crowder, trehalose (201). It is unclear whether a single extrinisic crowder will be sufficient to optimize protein formulations for the desired therapeutic properties for wide classes of proteins with varying stabilities, solubilities and molecular shapes. Additionally, more sophisticated freezing techniques than standard lyophilization may be required to preserve protein activity and engineer nanocluster particle morphology. In this study, we demonstrate that a multicomponent mixture of three crowding agents can be used to create stable dispersions of highly concentrated, active monoclonal antibody particles that retain high activity and bioavailability upon subcutaneous administration in mice.

The murine IgG2a monoclonal antibody 1B7, which binds and neutralizes the pertussis toxin (PTx) associated with whooping cough infection (216, 217), was selected to demonstrate applicability to a therapeutically relevant molecule and allow comparisons with previously described trehalose-only dispersion formulations. First, amorphous protein particles were generated via a new freezing method, spiral-wound in-situ freezing technique (SWIFT). Next, these particles were dispersed in the presence of three pharmaceutically acceptable crowding agents(218): water-soluble organic n-methyl-2-pyrrolidone (NMP), polyethylene glycol (PEG), and trehalose to yield a formulation with low viscosity (<50 cP), high antibody concentration (~200 mg/ml) and ~430 nm 1B7 nanoparticles. Importantly, the native 1B7 protein activity was preserved, as measured by in vitro biochemical methods and pharmacokinetics unaltered. Dispersions are a promising approach to generate highly concentrated, low viscosity antibody formulations. They can achieve dosages at least 10-fold higher than can be attained via solutions and can be formulated with a variety of pharmaceutically acceptable agents.

RESULTS AND DISCUSSION

Here, we report formation of highly concentrated, low viscosity dispersions of antibody nanoclusters, in which the antibody retains native size and binding activity upon dilution and in vivo sub-cutaneous administration. In contrast to our prior work (201), we used a novel freezing technique to form amorphous particles and multiple crowding agents to tune particle size. The combination of these innovations allowed us to administer subcutaneous antibody dispersions to mice at typical therapeutic doses (5.6-

7.3 mg/kg) as well as an ultra-high dose, more than 10-fold higher than current practice (51.6 mg/kg). The measured pharmacokinetic parameters were similar for solution and dispersion formulations and antibody present in serum at the terminal timepoint retained antigen binding and neutralizing activities expected for 1B7.

Stable Protein Particles made by SWIFT freezing

The first step in preparation of concentrated aqueous dispersions is formation of a dried powder of protein particles. The choice of freezing method can be critical to both protect antibody structure and activity during freezing, as well as to produce particles of the appropriate size and morphology to yield a colloidally stable dispersion. To address these concerns, we developed a novel freezing technique, SWIFT, which rapidly freezes an antibody solution directly in the final packaging vial prior to lyophilization (Figure 5.1A). The rationale in developing this technique is that two major sources of protein denaturation during freezing are exposure to liquid-gas interfaces during spray-freeze drying and the slow rate of freezing in larger volumes which can result in freeze concentration and subsequent concentration-dependent aggregation (219, 220). By rotating the vial of protein solution while in contact with liquid nitrogen, each concentric layer freezes in less than a second. The remaining liquid is gently mixed due to rotation, normalizing any concentration gradients.
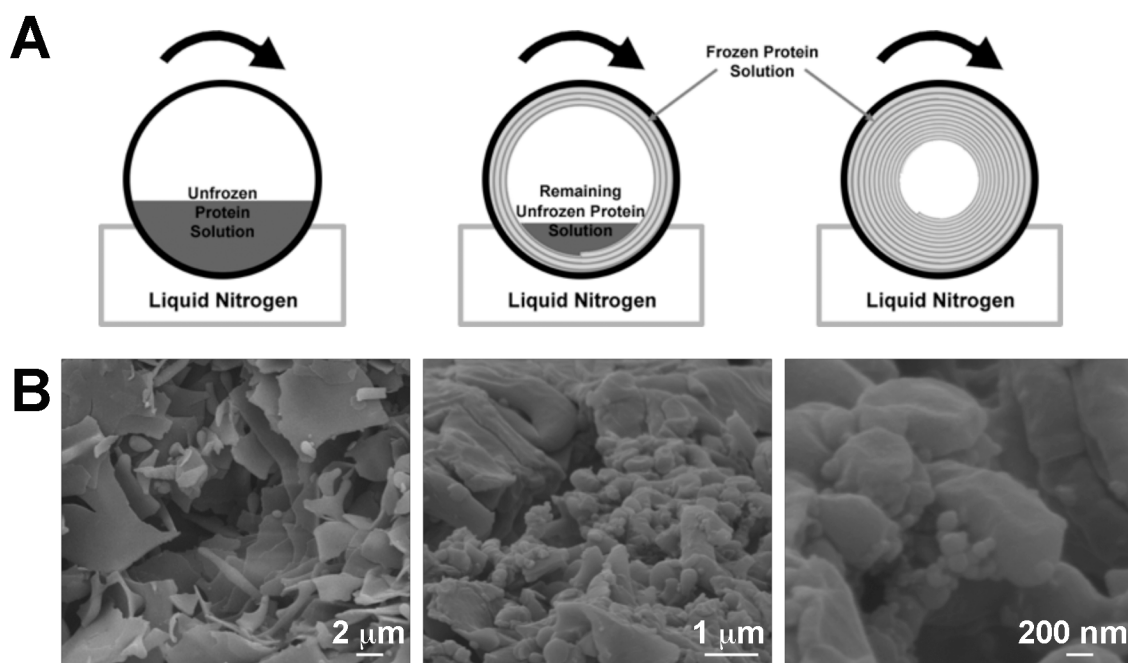
Figure 5.1: Schematic of SWIFT freezing process and dry powder SEM. (A) The unfrozen protein solution in a cylindrical vial is placed on its side and rolled while exposed to liquid nitrogen. This causes a thin film of the protein solution to freeze on the inside edge of the vial followed by subsequent films towards the center of the vial resulting in a frozen annulus of protein solution which is placed in the lyophilizer to remove water. (B) Morphology of SWIFT powder after lyophilization by SEM. Scale bars indicate 2 microns, 1 micron and 200 nm.

We used SWIFT followed by lyophilization to form micron-sized particles of the 1B7 antibody used in the dispersions. These small particles may aid in minimizing any gel formation during the resuspension process that would adversely affect antibody activity and formulation viscosity versus tray lyophilization, which is also compatible with dispersion formulations18. To prevent protein aggregation during freezing, the protein solution was adjusted to contain a 1:1 weight ratio of trehalose as a cryoprotectant (219). The buffer selected, 20 mM histidine pH 5.5, is commonly used during lyophilization steps44. An SEM analysis of the frozen and lyophilized 1B7 indicates the

142

presence of micron-sized particles (Figure 5.1B). Importantly, antibody processed in this manner retained native size and activity upon reconstitution with PBS at 5 mg/ml. At this concentration, DLS detected a single species with a ~10nm hydrodynamic diameter, as expected for an antibody monomer (Figure 5.2A)(196).
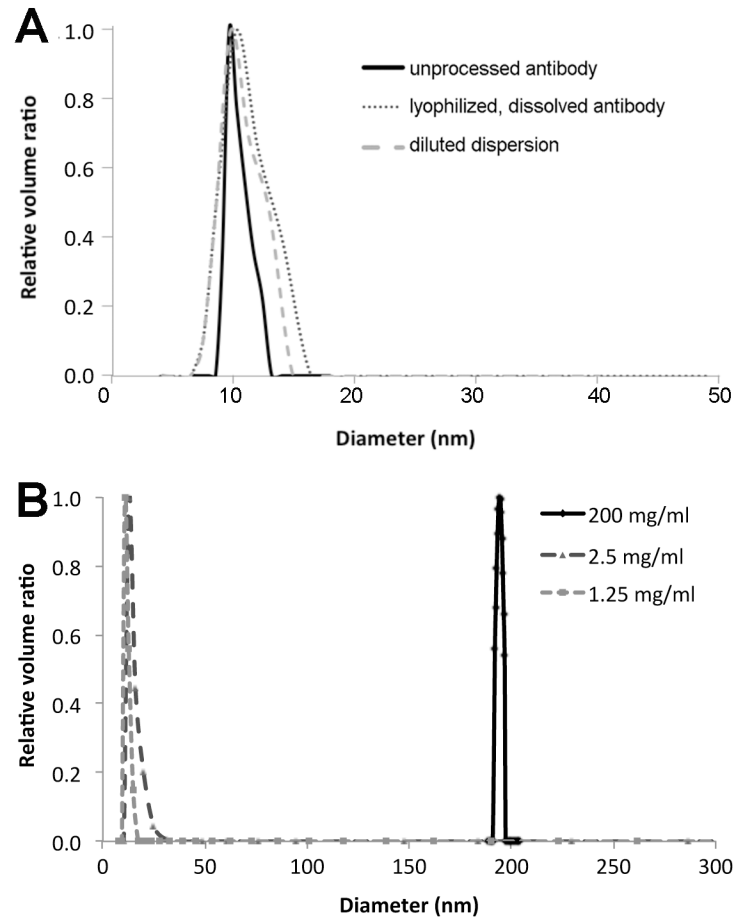
Figure 5.2: Size distribution of antibody particles. (A) Comparison of unprocessed, lyophilized and dispersed 1B7 by DLS. All samples were diluted to 5 mg/ml in PBS. (B) Effect of antibody concentration on particle size in dispersion buffer. At high concentration (200 mg/ml) in dispersion buffer, dynamic light scattering (DLS) detects only large particles of ~430 nm. Upon dilution below the threshold concentration for cluster formation in the dispersion buffer, concentrations of 2.5 and 1.25 mg/ml detect only particles of ~10 nm size, the expected size for monomeric IgG antibody. DLS data was analyzed by CONTIN.

143

The absence of larger particles indicated that the antibody did not form irreversible aggregates during SWIFT and lyophilization. In addition, an ELISA to monitor the specific PTx-binding activity of the reconstituted antibody revealed no significant change in activity due to SWIFT versus the untreated control (Table 5.1; Figure 5.3A), whereas ELISA after heat treatment (70°C for 60 minutes with 1 mM DTT) did detect a significant activity loss (data not shown).

Dispersion buffer	Protein concentration (mg/ml)	Solubility (mg/ml)	Colloid diameter (nm)	Apparent viscosity (cP)	Relative binding activity*
20% NMP 10% PEG300	190 ± 10	>2.5	196 ± 14	24 ± 7	1.50 ± 0.32

Table 5.1: Biophysical characterization of 1B7 dispersions. * Calculated as ($EC_{50,\,test}$/$EC_{50,\,control}$)
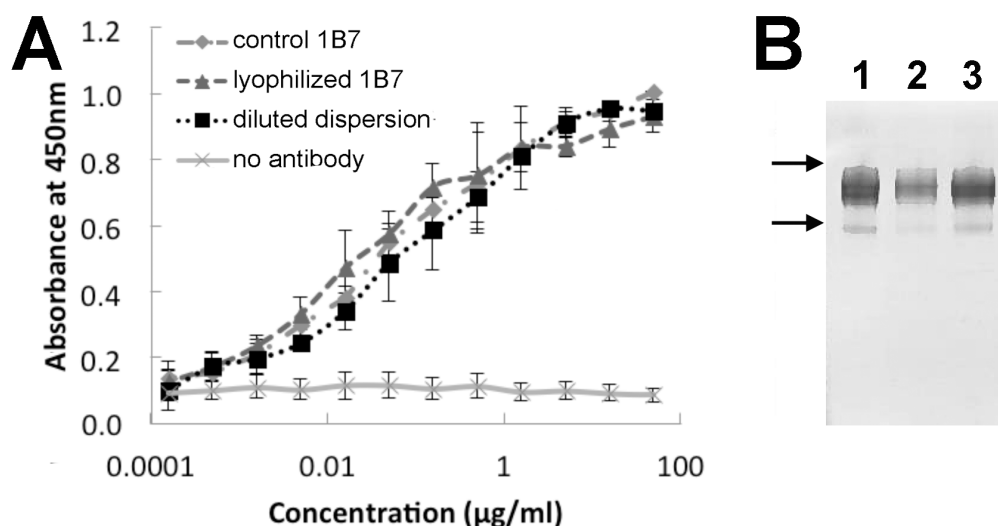
Figure 5.3: Characterization of antibody recovered from dispersion. (A) Comparison of unprocessed, lyophilized and dispersed 1B7 by PTx ELISA to monitor antibody activity. (B) SDS-PAGE gel comparing antibody 1B7 that is unprocessed, purified (lane 1), lyophilized, resuspended (lane 2) and a dispersion diluted from 200 to 1 mg/ml in PBS (lane 3). Arrows indicate the 175 and 140 kDa molecular weight markers.

The SWIFT process was designed to protect protein structure and activity. This is achieved via rapid freezing with minimal liquid-air interface, goals inspired by related process, thin film freezing (TFF)(221). In SWIFT, each film layer, corresponding to a single vial revolution, is ~200 nm thick (data not shown), Indirect contact with liquid nitrogen as a heat sink confers cooling rates of ~102 K/s. In TFF, a small volume of protein solution is deposited on a cryogenically cooled surface, where it spreads to ~210 nm thickness, freezing within a single second (221). Scaling-up to compare freezing times for equal volumes, TFF freezes at a rate of ~5.1 seconds per ml of protein solution, while SWIFT results in a similar rate, ~7.5 seconds/ml (Figure 5.4).
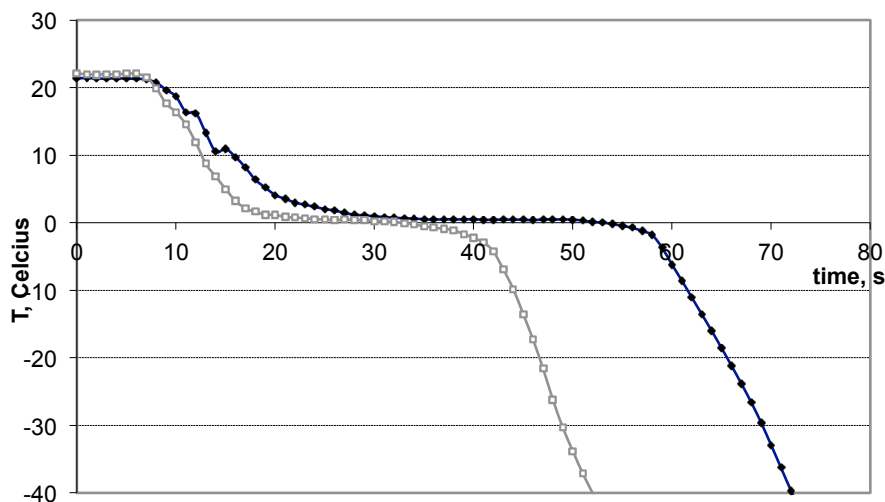
Figure 5.4: SWIFT freezing temperature profiles of lysozyme solutions (10 mg/ml) inside vials. The solutions were frozen in different film thicknesses 2.6 mm and 0.6 mm corresponding to the total liquid volume of 4 ml and 2.6 ml in vials with 15 mm diameter. The coolant temperature was 80 K and the vial rotation speed was 30 rpm.

As a result of the similarities in freezing rates and film thicknesses, TFF and SWIFT processing of similar protein solutions yields dry particles with similar morphologies (Figure 5.1B)(221). For TFF, and by extension, SWIFT, the rapid cooling

and freezing rates generate a large number of ice nuclei, which exclude solute molecules due to freezing point depression effects. The remaining liquid is present in thin channels between ice nuclei, becomes supersaturated with dissolved crowder molecules and protein. The rapid freezing and consequent rapid vitrification of these liquid channels inhibits solute diffusion; as these molecules precipitate, the reduced collision frequency inhibits coagulation of these small insoluble particles to generate larger particles. In addition, as the concentrations of dissolved solutes rise in the unfrozen liquid, the associated viscosity increase further reduces the mobility of the growing particle nuclei. During the dehydration step, water present in these channels is removed, leaving small particles of dry protein and crowder. In contrast, traditional tray freezing lyophilization with its slower freezing rate yields larger liquid channels and larger final particles after drying (221). Thus smaller submicron protein particles, as shown in Figure 5.1B, are formed during SWIFT freezing versus standard tray freezing lyophilization.

With both SWIFT and traditional tray lyophilization, low levels of protein denaturation and aggregation are achieved by kinetic and thermodynamic stabilization of the native protein structure during freezing and lyophilization. The native protein state is stabilized during lyophilization by kinetically trapping protein molecules in an amorphous solid (137, 204, 222), thereby reducing protein mobility that can lead to aggregation. Addition of the lyoprotectant trehalose during lyophilization further thermodynamically stabilizes the protein native state during freezing by entropically favoring the native folded state(204, 222, 223) and during dehydration by forming hydrogen bonds with proteins(224, 225). However, processes to rapidly freeze proteins

146

such as spray freeze drying (SFD), have been shown to increase protein aggregation versus standard tray freezing lyophilization due to the large gas-liquid interface in the spraying step (226, 227). The large area/volume of the gas-liquid interface of ~6000 cm^{-1} in SFD for 10 mm sprayed droplets can lead to protein adsorption at the interface, denaturation and aggregation (137, 226, 228-230). In the case of SWIFT, the gas-liquid interface is minimized as the only exposure of the liquid protein solution to the air is the liquid interface inside the glass vial. As a result, the estimated gas-liquid interface decreases 3 orders of magnitude when compared to SFD to ~4 cm^{-1}. Thus 1B7 was anticipated and found to remain active upon reconstitution to monomer from the dry powder form after SWIFT freezing and lyophilization.

One practical advantage of SWIFT freezing is the ability to freeze directly in the final dosage vial when compared to other rapid freezing techniques such as TFF and SFD (221, 230, 231). This approach avoids the need for costly, solid transfer steps while maintaining aseptic conditions. In this case, if a dosage of 80 mg of the protein is required at a concentration of 20 mg/ml, the 8 ml vial used in the study can serve as both the freezing and reconstitution vial. However, since the cooling rate of SWIFT freezing is governed by the liquid cryogen used and the thickness of the glass vial, as well as the heat transfer coefficients of the materials used, the vial can be readily scaled-up or down to meet dosage requirements. In addition, by removing the transfer step to the final vial, all of the protein can be recovered after lyophilization and utilized in the formation of the final dosage.

Colloidal Characterization of 1B7 particles in dispersion

To form the colloidally stable, translucent nanocluster dispersion, the dry, sub-micron particles of antibody and trehalose produced via SWIFT were combined (Figure 5.5A) with a 50 mM phosphate buffer adjusted to the antibody pI (pH 7.2) containing two additional crowding agents: 20% n-methyl-2-pyrrolidone (NMP) and 10% polyethylene glycol 300 (PEG300) by volume. After combining the SWIFT particles and dispersion buffer, the trehalose contained in the dry powder dissolves. A fraction of the trehalose will diffuse into the solution, increasing the volume fraction of crowding agents as observed previously for sheep IgG (201). Sufficient dispersion buffer was added to the dry powder to yield a final antibody concentration of 190 mg/ml with a final 0.34 volume fraction (Φ) of crowding agents.

Under these conditions, DLS with CONTIN analysis of the dispersion using a low volume (60 μL) cell identified a single population of particles with a ~432 +/- 16 nm diameter. This colloid size was reproduced in three separate experiments, measured each time in triplicate, with a representative curve shown in Figure 5.2B. This particle size was further confirmed by SEM images of the dispersion after dilution to 100 mg/ml in the dispersion buffer, rapid freezing and lyophilization onto an SEM stage (Figure 5.5B).
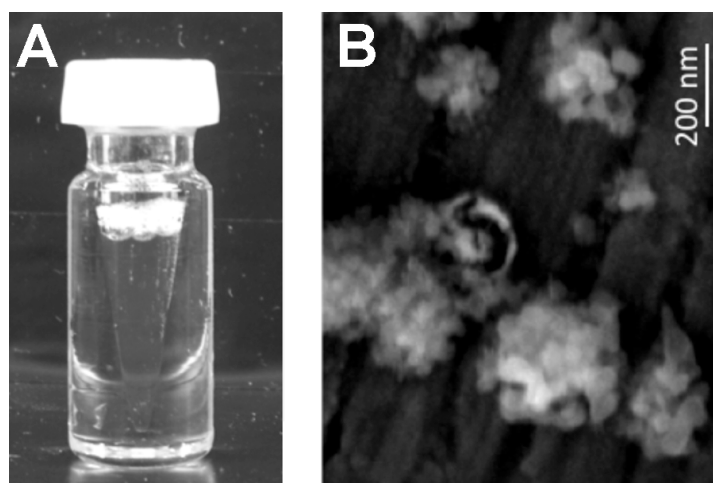
Figure 5.5: Visual appearance of dispersion. (A) Digital image of suspended particles. (B) SEM image of antibody dispersion (200 mg/ml) when diluted to 100 mg/ml in the dispersion buffer, rapidly frozen and the water removed by lyophilization. Scale bar corresponds to 200 nm.

This image shows nanoparticles of a size consistent with DLS measurements, but a different shape due to coating with crystallized trehalose. Previously, SEM and STEM images of dispersed sheep IgG and 1B7 particles at lower trehalose concentrations, visualized the dispersed particles as clusters of smaller particles (201). To confirm that these results are not affected by dissociation of the 1B7 nanoparticles, we determined the conditions where 1B7 nanoclusters dissociate to monomer in dispersion buffer, using methods reported previously (201). Starting with the 190 mg/ml dispersion, we progressively added dispersion buffer to reduce the protein concentration and measured the resulting particle sizes by DLS (Figure 5.2B). We observed a single peak at ~430 nm until the protein concentration was reduced to 2.5 mg/ml or less. At this concentration, only a single ~10 nm peak is present, corresponding to the hydrodynamic diameter of a single monoclonal antibody molecule (196). From these data, we conclude that 1B7 nanoclusters in this dispersion buffer completely dissociate to monomer at ~2.5 mg/ml

and that 1B7 nanoparticles formed with trehalose, PEG and NMP are fully reversible (Table 5.1).

The dispersed particles were formed and exhibited colloidal stability, possibly due to a previously proposed balancing of the intermolecular attractive and repulsive interactions at the protein molecular and colloidal levels, respectively (201). Briefly, individual protein molecules are subject to highly attractive depletion and specific short-ranged interactions such as hydrophobic interactions, hydrogen bonding and charge-dipole interactions (201, 232, 233). Near the 1B7 pI, longer-range electrostatic repulsion is relatively weak and thus the attraction force dominates between isolated pairs of protein molecules. However, once these molecules assemble into nanoclusters of sufficient size, the cumulative electrostatic interactions between particles in the cluster balance the attractions, stabilizing the dominant size (201). Between clusters, short-range attractive interactions are expected to be negligible relative to electrostatic repulsion resulting in a colloidally-stable dispersion of protein nanoclusters, as has been discussed previously (201).

The strength of depletion-attraction forces can be tuned by varying the concentrations of the crowding agents (234, 235). As observed here and previously (201), an increase in crowder concentrations favors 1B7 nanocluster formation. While 1B7 and the sheep IgG dispersions could both be formulated with a single crowding agent, trehalose, the ternary crowder system used here may provide additional flexibility to formulate dispersions with highly soluble proteins or to further control the nanocluster size, protein stability, dispersion viscosity and nanocluster degradation during delivery.

The low apparent viscosity, 24 cP, of the 190 mg/ml 1B7 dispersion was measured as the viscosity through a 25 gauge 1.5 inch needle (Table 5.1). This viscosity measurement was previously characterized for subcutaneous injections of highly concentrated solutions of monoclonal antibodies and non-aqueous suspensions of lyosyzme (205). Due to our very small sample volumes (~100 ul), we were concerned that evaporation would rapidly affect values measured with a traditional viscometer. The apparent dispersion viscosity is commonly described as a function of the intrinsic viscosity, [η], maximum volume fraction of particles, ϕ_{max}, and the solvent viscosity, η_0, using the Krieger-Dougherty equation (Eq. 1)(205, 236).

$$\frac{\eta}{\eta_o} = \left[1 - \left(\frac{\phi}{\phi_{max}} \right) \right]^{-[\eta]\phi_{max}}$$

Eq. 1

The η may be reduced by lowering η_0, or [η], which has a minimum of 2.5 for hard sphere colloids, and increasing ϕ_{max}. For protein molecules in solution at high concentrations, for example f = 0.1 to 0.3, strong short-range specific attractive interactions(233, 237), often produce viscosities 5 to 100 times the hard sphere value (198, 238). For monoclonal antibody solutions with concentrations of 150 mg/mL, viscosities greater than 100 cP have been attributed to reversible self-association of protein molecules, on the basis of measurements by analytical ultracentrifugation (198, 239). In contrast, the low viscosities observed in the present study for the nanocluster dispersions may be consistent with the weak interactions between the nanoclusters, as suggested previously (201).

In vitro molecular stability of 1B7 dispersion

As processing steps can adversely affect protein structure and activity, we monitored the antibody size within the dispersion and after dilution using several techniques, including DLS, non-reducing SDS-PAGE and ELISA (Table 5.1). After a 10-fold dilution from the 190 mg/ml dispersion into PBS, DLS measured a single species with a ~10 nm hydrodynamic diameter, as expected for a single antibody monomer (Figure 5.2A)(196). The absence of larger particles indicates the dispersion formulation does not induce irreversible aggregates and that the antibody can readily recover its monomeric size upon dilution. This is further confirmed by non-reducing SDS-PAGE (Figure 5.3B), in which a single band of the expected antibody monomer size ~150 kDa is observed, indicating an absence of irreversible thiol-linked and SDS-resistant aggregates (240). Finally, an ELISA to monitor the specific PTx-binding activity of the antibody reveals no significant change in activity due to the formation or dilution of the dispersion versus untreated control based on EC_{50} comparisons (Figure 5.3A; Table 5.1).

For antibody formulated as a dispersion to maintain therapeutic efficacy upon in vivo injection(241, 242), the native antibody activity must be maintained through every processing and delivery step: from (1) freezing and lyophilizing the antibody solution, (2) nanocluster formation via dispersion, and (3) delivery through a syringe, to (4) nanocluster dissociation and diffusion from the injection site. While loss of protein conformational stability can result from chemical degradation as well as physical denaturation processes, physical denaturation is expected to be the larger challenge to successful development of high protein concentration formulations due to its strong

dependence on protein concentration (192, 241). As discussed above, the protein powder formed by SWIFT freezing and lyophilization exhibited no detectable loss in antigen-binding activity or development of aggregates after reconstitution in buffer.

It has been speculated that the use of in vitro self-crowding to stabilize native protein might mimic the in vivo intracellular environment, in which folded proteins are stabilized by a high concentration of diverse molecular crowding agents (300-400 mg/ml) (214, 243). In that model, the high protein volume fraction within a nanocluster allows the protein to act as its own crowding agent, entropically favoring the lowest surface area conformation of the protein, which is typically the native state (201, 214, 215). This result was originally predicted theoretically(214), but the first indirect experimental validation awaited development of dispersions(201) as protein solutions cannot achieve the high protein volume fractions (>0.15) necessary. Unfolding and irreversible aggregation of protein molecules in the nanocluster is thought to be further reduced by decreased protein mobility within the highly concentrated nanocluster versus a solution (189, 244, 245). Since molecule collisions can lead to the formation of aggregates, a reduced collision frequency among protein molecules at the nanocluster-buffer interface kinetically stabilizes these molecules (195, 201, 246).

The retention of protein activity and the lack of detectable aggregates upon in vitro dilution from the concentrated dispersion is an important indication of in vivo protein stability. At the high concentrations of the dispersion formulation, we speculate that the 1B7 antibody is stabilized within the nanoclusters by self-crowding, at the nanocluster boundary layer and in the aqueous phase by crowders present in the

dispersion buffer (247). Similarly, the diluted 1B7 is stable at final solution concentrations (~10 mg/ml) in PBS buffer due to the inherent stability of the immunoglobulin fold, which has evolved to persist for ~23 days in serum containing 60-85 mg/ml total protein. The most aggregation-prone step will occur at intermediate concentrations, when the protein is no longer at a sufficiently high concentration for self-crowding to inhibit partial unfolding, but high enough for transiently unfolded intermediates to aggregate via concentration-dependent aggregation. Using the Noyes-Whitney equation for high surface area to volume particles, we predicted a nanocluster dissociation time, to provide an estimate of the duration the protein spends in this intermediate concentration regime. Dilution of ~430 nm antibody nanoclusters into PBS, in which 1B7 nanocluster threshold concentration is >50 mg/ml, is expected to result in particle dissociation in less than one second.

Experimentally, dilution of 1B7 protein nanoclusters with dispersion buffer to maintain a constant crowder concentration resulted in recovery of monomeric, active protein, as measured by DLS and ELISA (201). For a trehalose-induced polyclonal sheep IgG dispersion at a constant protein concentration, a steady decrease in nanoparticle size was achieved by diluting the crowder to weaken the attractive forces between immunoglobulin molecules (201). At each step, the clusters were fully diluted and characterized, and found to have expected activity as measured by ELISA (201). The protein molecules on the cluster surface are expected to be crowded by protein molecules on the cluster side and sugar molecules at the cluster-buffer interface. As protein

154

molecules diffuse away from the cluster surface into the PBS media, they retain activity as shown by the DLS and ELISA experiments.

In vivo bioavailability of stable 1B7 from dispersions

No reliable in vitro models exist to mimic in vivo dissociation of the dispersion after subcutaneous injection. Thus, we proceeded to a mouse model to measure the pharmacokinetic parameters as well as the specific activity of in vivo dissolved antibody material. The five treatment groups included three control groups to allow direct pharmacokinetic comparison of low volume, high concentration and large volume, high concentration dispersion test groups. The control groups 1 and 2 received a standard antibody dose (4.6-5.6 mg/kg in 100 μl) to allow for a direct comparison of the subcutaneous dispersion injection pharmacokinetics to intravenous and sub-cutaneous delivery of an antibody solution. A third control, group 3, assessed the effect of dispersion formulation on antibody pharmacokinetics, in which the dispersion was diluted to 1.4 mg/ml with dispersion buffer, a concentration below the cluster limit and comprised of antibody monomers. Two test groups were designed to assess the combined effects of dispersion concentration and delivered volume on in vivo dissociation rates and the resulting pharmacokinetics. In group 4, mice received a standard dose (7.3 mg/kg) administered as a high concentration dispersion (190 mg/ml) in a small 1 μl volume. Group 5 received an ultra-high antibody dose, which can only be achieved with high concentration, low viscosity formulations such as a dispersion. These mice received a ten-fold higher dose than the other groups (51.6 mg/kg in 100 μl). For all groups, serum

samples were collected from the tail vein over 14 days, with the concentrations of total and active 1B7 antibody in each sample measured by streptavidin and PTx capture ELISAs, respectively. The efficacy of antibody present at the terminal time point was also assessed using an in vitro activity assay, based on antibody-mediated inhibition of toxin activity.

Overall, the 1B7 pharmacokinetic profile is quite similar for all groups, with distribution and elimination kinetics all within error. The primary differences result from the injection site and injection volume, affecting the time to reach the maximum concentration (t_{max}) and the value of the maximum concentration (C_{max}/ dose). Looking first at the three control groups, delivery via subcutaneous dispersion resulted in a lower C_{max}/dose and delayed t_{max}, as compared to IV and subcutaneous delivery of solutions (Table 5.2; Figure 5.6).

Group	1: IV Solution *	2: SQ Solution *	3: SQ Diluted Dispersion	4: SQ Dispersion, Standard Dose	5: SQ Dispersion, High Dose
N	6	4	5	5	6
Injection Volume (μl)	100	100	100	1	100
Dose (mg/kg)	5.6	5.6	4.6	7.3	51.6
C_{max}/dose (μg/ml)/(mg/kg)	25.5 ± 3.8	18.8 ± 4.4	9.1 ± 3.2	7.3 ± 1.3	7.6 ± 2.6
AUC $_{0-\infty}$/ dose (μg·hr/ml)/(mg/kg)	3582 ± 990	2699 ± 583	1790 ± 630	1345 ± 467	1919 ± 566
t_{max} (hours)	15.1 ± 0.7	18.9 ± 3.1	28.8 ± 12.0	20.1 ± 3.2	20.2 ± 5.2
$t_{1/2,\alpha}$ (hours)	45.7 ± 22.8	43.4 ± 17.3	54 ± 21 *	49 ± 29*	51 ± 23 *
$t_{1/2,\beta}$ (hours)	227.1 ± 24.9	210.0 ± 17.4	219 ± 25	180± 16	250± 24
Relative Neutralization Activity	2.3 ± 1.7	1.0 ± 1.8	0.4 ± 0.2	0.5 ± 0.2	2.1 ± 1.0

Table 5.2: Pharmacokinetic parameters for antibody 1B7 formulations. * $t_{1/2,\alpha}$ determined from 2 points for some mice. Data reported(201)
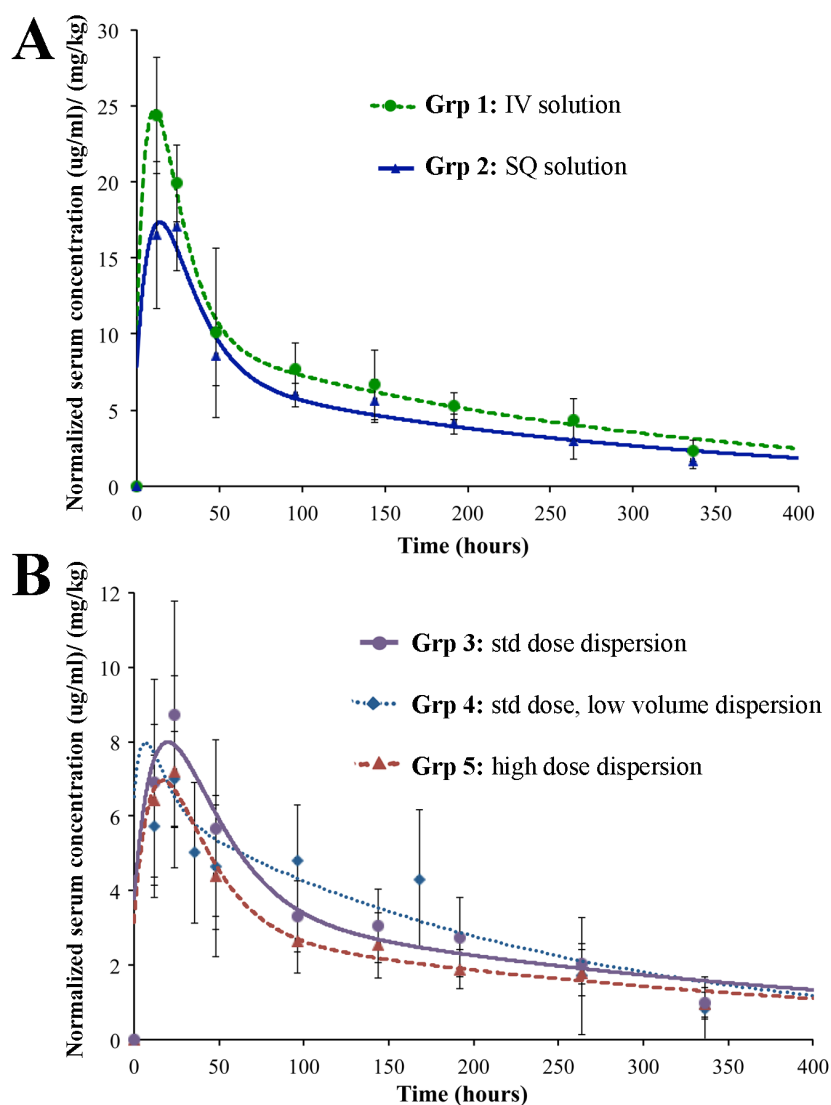
Figure 5.6: Serum concentrations of antibody 1B7 after delivery. The 1B7 antibody was formulated and administered to mice with the indicated volumes and doses. At the indicated times, tail vein samples were collected and the concentration of active antibody present measured by PTx ELISA, normalized by the administered dose and plotted. (A) Comparison of antibody 1B7 pharmacokinetics when delivered as a 100 μl solution. Group 1 mice received an IV administration at 5.6 mg/kg, while Group 2 mice received a subcutaneous delivery at 5.6 mg/kg. (B) Comparison of 1B7 pharmacokinetics when delivered via subcutaneous dispersion with varying concentrations and injection volumes. Groups 3 mice received a standard dose as a diluted dispersion at 4.6 mg/kg in a 100 μl injection volume, Group 4 mice received a standard dose dispersion at 7.3 mg/kg in a 1 μl injection volume, while Group 5 mice received high-dose dispersion at 51.6 mg/kg dose in a 100 μl injection volume. Curve fits by spline fitting.

The group 1 control IV solution reached a maximum serum concentration at the first measured time point (12 hours), followed by a rapid decrease as the antibody is distributed throughout the tissues (201). In comparison, the subcutaneous solution group displayed a slightly reduced C_{max}/dose (25.5 versus 18.8 ug/ml/ mg/kg) and statistically significant delayed t_{max} (15 versus 19 hrs; $p<0.05$). While IV-administered material is instantly diluted in the blood volume, material administered subcutaneously must diffuse from the injection site through interstitial fluid to reach the lymphatic and blood vessels before distribution in the blood volume, delaying these pharmacokinetic parameters (Figure 5.6A)(201, 248). The subcutaneous dispersion injections, groups 3 and 5, exhibit similar trends as the subcutaneous solution but with a slightly lower C_{max} and delayed t_{max} when compared to the subcutaneous solution (Figure 5.6B). This may reflect the effects of the dispersion buffer on antibody diffusion, as the effect is minimized with group 4, standard dose subcutaneous dispersion, which was injected as a ~1 ul volume instead of a 100 ul volume using a positive displacement microvolume syringe. For this sample, the t_{max} was similar (within error) to that of the subcutaneous solution.

Once the maximum serum concentration is attained, all groups show similar 1B7 distribution and elimination pharmacokinetics. As seen in Figure 5.6, these data fit a biphasic exponential profile, with α distribution and β elimination time constants that are within experimental error for all groups, based on 1B7 concentrations measured by the PTx ELISA (Table 5.2). The β elimination half-life was also within error for all groups when measured using a total 1B7 ELISA assay, based on streptavidin detection of the biotinylated antibody (data not shown). The distribution phase represents passive

159

antibody diffusion from the well-mixed blood volume into other tissues, driven by the 1B7 concentration gradient and the elevated vascular pressure, while antibody elimination rates are controlled by interactions with specific receptors such as the FcRn (248, 249). Notably, both rates will vary with antibody aggregation and misfolding. A soluble aggregate will have a larger size and consequently larger diffusion constant and slower $t_{1/2}\alpha$, while a misfolded monomer or soluble aggregate will exhibit different binding kinetics for the FcRn and a different $t_{1/2}\beta$. The similar kinetics observed for all groups indicate that the antibody delivered as a subcutaneous dispersion is able to dissociate from the nanocluster and diffuse away from the injection site while retaining an active, monomeric form, similar to our in vitro observation in which active 1B7 monomer is rapidly recovered upon dispersion dilution.

These experiments were performed in mice, where the large permissible injection volume per body mass (100 μl/ 25g) allows for direct comparisons between solutions and dispersions formulated at the same concentration. A similar comparison is not possible in humans, as subcutaneous injections are restricted to ~1.5 ml volume. To demonstrate that dispersions can achieve dosages relevant for humans, we prepared group 4 as a scaled-down version of a human dose (Figure 5.6B). Here, a ~1 μl volume of highly concentrated dispersion (190 mg/ml) was administered subcutaneously, for a final 7.6 mg/kg murine dosage. Scaling-up to calculate the human dosage, in which a 190 mg/ml dispersion could be administered in a 1.5 ml volume, this is equivalent to a 4.3 mg/kg human dose, exceeding current typical dosing guidelines (2 mg/kg). To evaluate the potential for dispersions to result in less-frequent administration of ultra-high antibody

dosages, which are not currently achievable with solutions, group 5 mice received a large, 100 μl injection volume of highly concentrated dispersion (190 mg/ml), for a 51.6 mg/kg dose. In spite of the large error inherent to administering a 1 μl injection of a viscous solution, this group also exhibited similar pharmacokinetics (similar t_{max}, $t_{1/2}$,α, t1/2,β) and 1B7 bioavailability indicating concentration and dose-independent pharmacokinetics. Reduced absolute bioavailability of 50-100% is expected for a subcutaneous administration and was observed in this study as 75.4% +/- 26.4 for the sub-cutaneous solution control. The relative bioavailability of the dispersion formulations were further reduced (66.3% +/- 27.4 for the diluted dispersion, 49.8% +/- 20.4 for the standard dose dispersion, and 71.1% +/- 26.0 for the high-dose dispersion), possibly due to incomplete cluster dissociation and/or increased lymphatic processing. This decrease in relative bioavailability is likely related to the use of crowder agents employed in this study, as previous work using only trehalose resulted in relative bioavailability within error of subcutaneous solution injections (201).

To provide an orthogonal measurement of antibody quality to complement antigen ELISA, we measured 1B7 biological activity with an in vitro CHO cell neutralization assay using sera from the terminal time point. Free PTx will bind cell-surface receptors, undergo receptor-mediated endocytosis and eventually ADP-ribosylation of $G_{i/o}$ coupled receptors; phenotypically, the cells lose contact inhibition and grow in a clustered morphology. Antibody-mediated neutralization of PTx blocks toxin entry into cells, protecting the normal growth phenotype. Sera were diluted in the presence of a fixed PTx concentration, CHO cells added and, after 24 hrs growth, scored

161

for normal or clustered morphology. The highest sera dilution completely preventing CHO cell clustering was recorded and compared versus purified control 1B7 antibody. This assay resulted in no statistically significant differences between groups on titre per µg antibody basis. Based on this assay, there is no evidence for a loss in antibody efficacy as a result of injection site (subcutaneous vs. IV) or formulation (Table 5.2). Western blot analysis was used to demonstrate the absence of gross physical changes in serum antibody due to formulation and administration route, such as formation of insoluble or disulfide bonded aggregates (data not shown). This in vivo data is consistent with our in vitro observations, that the protein within the dispersion shows no detectable loss of native size or activity during processing or in vivo administration.

CONCLUSIONS

Nanocluster dispersions allow monoclonal antibody formulation at high concentration and low viscosity, with no detectable loss in antibody size or activity in vitro or in vivo and similar pharmacokinetics when administered subcutaneously to mice. Highly concentrated ~190 mg/ml aqueous-based dispersions of a therapeutically relevant antibody, 1B7(217), were formed from stable, submicron protein particles containing a 1:1 weight ratio of trehalose in an aqueous buffer with multiple crowding agents, including trehalose, PEG and NMP. These particles were produced by rapid freezing in a dosage vial using SWIFT to minimize protein denaturation and aggregation, followed by lyophilization. A nanocluster dispersion was formed in the aqueous-based solvent near 1B7's pI by adding pharmaceutically acceptable crowding agents, PEG300 and NMP,

along with the trehalose from the dry powder. Additional analyses, ELISA, DLS and SDS-PAGE, indicate that the protein rapidly recovers a fully active monomeric form upon dilution of the dispersion with PBS. The apparent viscosity of the 190 mg/ml IgG dispersion with NMP and PEG through a 25 g 1.5" needle was only 24 cP, reflecting the low initial solution viscosity and the low intrinsic viscosity. The measured in vivo distribution and elimination half-lives were similar for control solution and dispersion formulations administered at similar doses. The time to peak serum concentration (t_{max}) was delayed for the subcutaneous injections, consistent with the expected slower diffusion kinetics from this injection site. Remarkably, analysis of terminal serum samples was unable to detect a loss in 1B7 activity over the 14-day study period. This formulation strategy, in which crowding agents drive formation and stabilization of protein nanoclusters, has been shown to be applicable for both monoclonal and polyclonal antibodies. In this work, we demonstrate formulation with multiple crowding agents, which will provide flexibility in formulating additional therapeutic proteins. The ability to form stable, highly concentrated dispersions of a protein therapeutic with low viscosities and favorable bioavailability will increase the potential use of subcutaneous injection, possibly for treatment of many chronic diseases.

MATERIALS AND METHODS

Antibody expression and, purification

Murine hybridoma cells producing the IgG2a antibody 1B7 were grown in 1 liter shaker flasks in Hybridoma-SFM serum-free media (Gibco) at 37°C with 5% CO2, as

reported previously (201, 217). Briefly, antibody purification consisted of media clarification by centrifugation at 3,000 rpm for 20 minutes, followed by filter sterilization using a 0.2 μm filter, 1:1 dilution with binding buffer (20 mM pH 7.0 sodium phosphate) and loading onto a pre-equilibrated Protein-A column with an Akta FPLC system (GE Healthcare). After baseline stabilization, 1B7 was eluted into collection tubes containing 1 M Tris pH 8.0 using a low-pH elution buffer (0.1M glycine pH 2.7), concentrated and buffer exchanged with centrifugal micro-dialysis units (Centricon). Protein concentration was measured with micro-bicinchonoinic acid (BCA) assay (Pierce, Rockford, IL), while non-reducing SDS-PAGE verified protein preparation homogeneity and purity. Purified 1B7 was labeled with biotin using EZ-link® Sulfo-NHS-LC-Biotin (Pierce, Rockford, IL) to provide an orthogonal detection handle to track the murine antibody in murine serum samples. A 5 mM solution of the biotin reagent was added at a 5:1 molar ratio to a 1 mg/ml solution of the 1B7 in PBS at room temperature and allowed to react for 30 minutes. Excess biotin was removed by buffer exchange using 50,000 MWCO Centricon concentrators with PBS. Protein was >95% pure, as judged by SDS-PAGE, SEC and isoelectric focusing gel.

Amorphous particle formation by spiral wound in-situ freezing technology (SWIFT)

Purified and biotinylated 1B7 was buffer exchanged into 20 mM pH 5.5 histidine buffer using Centricons, as above. The protein concentration was measured, solid α-α trehalose (JT Baker) was added to a 1:1 wt ratio as a cryoprotectant and gently mixed to dissolve. The resulting solution was filter sterilized (0.22 μm), diluted to 20 mg/ml

protein and transferred to a sterile 8ml (1.9 cm x 4.8 cm) glass vial for SWIFT freezing. During SWIFT, the base of the vial was contacted with liquid nitrogen while rotating the vial on its side (~1 revolution/second), resulting in a thin film of frozen solution on the inside edge of the vial, with subsequent thin films freezing in a spiral towards the center of the vial (Figure 5.1A). After the entire volume was frozen (~10-40 seconds), the samples were placed upright on a pre-cooled lyophilizer shelf at -40℃. The samples were then lyophilized for 12 hours at -40°C at 100mTorr, followed by a 6 hour ramp to 25°C at 50 mTorr, and maintained for secondary drying at 25°C at 50 mTorr for at least an additional 6 hours. To assess protein activity after freezing, powder was reconstituted at 5 mg/ml in PBS for analysis by dynamic light scattering (DLS) and enzyme-linked immunosorbent assay (ELISA) as described below. Samples of the dry powders after lyophilization for scanning electron microscopy (SEM) analysis were placed on adhesive carbon tape to fix the sample to the SEM stub. Each sample for SEM was platinum-palladium sputter coated using a Cressington 208 bench top sputter coater to a thickness of 10nm. Micrographs were taken using a Zeiss Supra 40 VP scanning electron microscope with an accelerating voltage of 5 kV.

Dispersion formation

To form the dispersion, SWIFT frozen and lyophilized 1B7 protein powder was compacted into 0.1ml conical vials (Wheaton Science Products No. 986211) such that the total powder weight was 0.04 ± 0.001 g. An aqueous-based solvent dispersion buffer, containing 10% (v/v) PEG300 (Spectrum Chemical Manufacturing) and 20% (v/v) n-

methyl-2-pyrrolidone (NMP; Malinckrodt) in a 50 mM phosphate buffer with the pH adjusted to match the measured antibody pI (pH 7.2, data not shown), was added to the lyophilized protein. Gentle stirring with the tip of a needle removed air pockets, to yield a uniform, optically clear dispersion with a final 1B7 concentration of 190 mg/ml. Neither sonication nor violent mixing was necessary to form a uniform translucent dispersion. All analyses were performed within two hours of dispersion formulation.

Viscosity measurement

The apparent viscosity of the 1B7 dispersion was measured as the time to draw 50 μl of the dispersion into a 25 gauge 1.5" long needle attached to a 1ml tuberculin slip tip syringe, as reported previously for sheep IgG dispersions (201). Briefly, videos of the conical vial containing the dispersion were taken and the time to draw from a height 0.4" from the bottom of the cone to a height 0.1" from the bottom of the cone was measured using Image J software. A standard curve using known solutions with various viscosities provided a linear correlation between the time to draw 50 μl from the conical vial to the viscosity with an R^2 value greater than 0.9918. These results are consistent with previous work with suspensions of model proteins and protein solutions which found that the time to draw up a specified amount of the sample in a syringe was correlated linearly to viscosity (198, 201, 205).

Colloidal size determination/ characterization

Dynamic light scattering (DLS) was used to measure the sizes of particles present in the purified 1B7 preparation, concentrated 1B7 dispersion and dilutions of the

dispersion using a custom-built DLS apparatus39 modified to include backscattering angles up to 165°(201). Particle sizes in the concentrated dispersion were measured with a small volume cell (60 μl, Beckman Coulter #A54094) at ~23°C and a 160° scattering angle, while all other measurements were made in a standard 1 ml cell at ~23°C and scattering angles optimized to detect the relevant particle size, as analyzed with CONTIN. To estimate the concentration below which only 1B7 monomers are present in the dispersion buffer, the 190 mg/ml dispersion was diluted 1:40, 1:80 and 1:160 in dispersion buffer and particle sizes measured at a 90° scattering angle. We define the concentration of 1B7 at which the protein monomer peak is observed by DLS as the threshold concentration for cluster formation. To mimic the effects of dilution on particle size and detect formation of aggregates, the dispersion was diluted 1:40 in PBS to give a final 5 mg/ml 1B7 concentration and the resulting particle sizes measured at a scattering angle of 30°. The size of purified 1B7 monomeric antibody in PBS was measured at 5 mg/ml and a scattering angle of 30°.

In vitro antibody activity and aggregation assays

All assays of protein activity and structural stability were conducted on 1B7 dispersion diluted to 1 mg/ml in PBS. Controls included lyophilized 1B7 and purified, untreated 1B7, both adjusted to 1 mg/ml in PBS. The formation of insoluble and di-sulfide linked aggregates was monitored by non-reducing SDS-PAGE. Here, 3 μg 1B7 sample was combined with loading buffer, separated on a 4-20% precast linear gradient polyacrylamide gel (Bio-Rad) and stained with Gel-Code Blue (Bio-Rad).

To monitor ligand-binding activity, an indirect PTx ELISA was employed as reported previously (201, 217). High-binding ELISA plates (Costar) were coated with pertussis toxin (PTx, List Biological Laboratories) at 0.75 μg/ml in PBS and incubated at 4°C overnight. Wells were blocked with assay buffer (PBS-1% milk) for 1 hour, prior to addition of 1B7 samples in a √10 serial dilution scheme from 50 μg/ml in assay buffer. After a one hour incubation at room temperature and triplicate washes with PBS-0.05% Tween-20, goat anti-mouse IgG-horseradish peroxidase conjugate (1:2,000 dilution in assay buffer, Sigma) was incubated for one hour at room temperature. Plates were washed in triplicate and signal developed with tetramethylbenzidine dihydrochloride (TMB) substrate (Pierce), quenched with 1N HCl and the resulting absorbance at 450 nm recorded using a SpectraMax M5 instrument. The EC_{50} value was calculated from the linear range of the dose-response curve as the antibody concentration corresponding to 50% of the maximum absorbance, based on a four-parameter fit. For comparison between samples, the relative EC_{50} was calculated as the ratio of the sample EC_{50} to unprocessed control antibody EC_{50}. All samples were run in triplicate.

In vivo bioavailability in BALB/c mice

An in vivo pharmacokinetic study of the 1B7 dispersion and control solution was performed over a 14 day period using four to six healthy 24-27g, female BALB/c mice per group. Mice were administered a single 1 or 100 μl subcutaneous injection of 1B7 at standard (4.6-7.3 mg 1B7/kg body weight) or high (~51.6 mg/kg) doses. The five sample groups compared in this study included two solution control groups receiving (1) IV and

(2) subcutaneous injections of 100 μl 1B7 solution (1.4 mg/ml solution for a final 5.6 mg/kg dose),(201) as well as three test groups, receiving subcutaneous injections of (3) 100 μl of a diluted PEG-NMP dispersion at standard dose (4.6 mg/kg), (4) 1 μl dispersion at a standard (7.3 mg/kg) dose; and (5) 100 μl of dispersion at high dose (51.6 mg/kg) (see Table 5.2). The previously reported solution controls (groups 1 and 2) were prepared from a 20 mg/ml 1B7 solution in PBS diluted to 1.4 mg/ml in PBS(201) while the dispersion samples were diluted from a 190 mg/ml 1B7 dispersion to a concentration of 1.2 mg/ml for group 3 (at this concentration, below the threshold for nanocluster formation, the antibodies are recovered as monomers), 12.9 mg/ml for group 4, and 190 mg/ml for group 5 with dispersion buffer immediately prior to injection.

Prior to the injection and at eight additional timepoints between 12 and 336 hours, mice were weighed and a blood sample (~20 μl) collected from the tail vein. After collection, the samples were allowed to clot, centrifuged at 5,000 rpm for 10 minutes and serum transferred to a new tube. At the terminal timepoint (336 hours), mice were anaesthetized and between 0.2 and 1 ml serum collected by cardiac puncture. These samples were used in ELISA assays, to measure the total and active concentrations of 1B7 in the serum and, for the terminal time point, to measure antibody activity via an in vitro neutralization assays and to provide an initial estimate of mouse anti-1B7 responses. This study was performed with approval by the Institutional Animal Care and Use Committee at the University of Texas at Austin (protocol #AUP-2010-00070) in compliance with guidelines from the Office of Laboratory Animal Welfare. To estimate

t_{max} and C_{max}, a curve was fit to the pharmacokinetic data for each mouse using natural cubic spline interpolation over the entire time interval. The corresponding maximum was then determined analytically from the resulting cubic polynomial on the interval of interest. To calculate the AUC values, the data were fit to a four-parameter bi-exponential model with one termed weighted by time: $c = A \exp(-\alpha t) + B\, t \exp(-\beta t)$. The AUC was defined as the improper integral of this model as time approaches infinity.

Measurement of 1B7 in serum samples

To determine the concentration of active 1B7 in serum samples, a standard ELISA approach was used with the following modifications as previously reported (201, 250). ELISA plates were coated with PTx at 1.5 µg/ml in PBS. The assay buffer used as diluent in all steps consists of 4% bovine serum albumin, 4% fetal bovine serum (FBS), 0.05% Tween 20, in PBS, pH 7.4. After blocking with assay buffer, 2.3 µl serum sample was serially 1:√10 diluted in 50 µl per well assay buffer. Each plate included mouse serum (Sigma) as a negative control and a 1B7 standard curve diluted to an initial concentration of 100 µg/ml in mouse serum. Additional samples were analyzed to assess total 1B7 protein levels using a streptavidin coating on the ELISA plates to detect the biotinylated 1B7.

After measurement of the resulting absorbance values, SoftMax Pro v5 was used to calculate EC_{50} values based on the serum dilution using a 4-parameter logistic (4PL) model for each individual curve. Concentrations of active 1B7 in each serum sample were calculated from a linear correlation between the log [(sample EC_{50})/ (standard

EC_{50})] versus the log of the known 1B7 concentration in the standard curve. A linear correlation with a fit > 0.95 from at least 5 independent standard curves were determined.

Measurement of active antibody by CHO cell neutralization assay

As an orthogonal activity measurement to determine the concentration of serum 1B7 able to neutralize PTx activity in vitro, we employed a CHO cell neutralization assay modified from Gillenius et al (217, 251). The concentration of neutralizing antibody was measured as the sera dilution that completely inhibited PTx-induced CHO cell clustering relative to a standard curve of purified 1B7 with known concentration. Briefly, 50 μl of 0.5 ng/ml pertussis in Dulbecco's Modified Eagle Medium (DMEM) with 10% FBS was added directly to each well of a sterile 96 well tissue culture plate. Terminal serum samples (23 μl) were serially diluted into the PTx media using a 1:√10 dilution scheme. After incubation for 30 minutes at 37°C and 5% carbon dioxide, 100 μl / well of freshly trypsinized CHO cells at 10^5cells/ ml were seeded in each well. After 48 h of incubation at 37°C and 5% CO_2, wells were scored for CHO clustering using 0-3 scale, with 0 as elongated (non-clustered) and 3 as completely clustered. A 5-parameter logistic model was used to fit the assay scores against 1B7 concentration and to find the hypothetical concentration yielding a CHO score of 1.5. The molar ratio of 1B7 to PTx at this point was then calculated relative to that of the standard and reported as the relative activity.

Chapter 6: Conclusions and Future Directions

CONCLUSIONS

The work described in this dissertation was focused on developing delivery systems for vaccines and therapeutic proteins with the overall goal of achieving administration by routes previously not possible. Approved vaccines today rely on injection (subcutaneous or intradermal) of live-attenuated pathogens or protein antigens and glycoconjugates with adjuvant formulations. Such methods have drawbacks; for example injectable vaccines use heat-killed or pathogen subunits in order to elicit immune responses, without administering live microorganisms or viruses into systemic circulation. However, these injectable vaccines bypass the natural infection route, leading to a lack of mucosal immunity (253). Live-attenuated pathogens administered via mucosal route would result in more complete protection by inducing secretory IgA, which plays an important role in preventing physiological entry of pathogens (20, 253). However, there are important safety concerns when utilizing "live" vaccines, the major concern being their potential to revert to a virulent form (20, 85). Due to practicality of administration and the lack of systemic immunity induced by other routes, oral and nasal delivery are the only mucosal routes clinically suitable for vaccines (4, 88). While researchers are making strides to develop subunit nasal vaccines, clinical success has been stunted due to safety concerns (88). This thesis therefore devoted a large portion of its efforts towards developing a platform for oral delivery of mucosal vaccines.

One of the key challenges facing oral vaccines is an inability to efficiently target intestinal sampling cells called M cells (88, 90). In Chapter Two, we describe the

173

molecular engineering of an M cell targeting protein ligand. One potential M cell target, not expressed on the apical surface of other enterocytes, is α5β1 integrin (32, 57, 59). We used a naturally existing α5β1 integrin found in the pathogen *Yersinia psuedotuberculosis*, called invasin, as a template to engineer a higher affinity M cell targeting ligand (69). Since this protein is naturally displayed on the bacterial surface, affinity matured variants could be selected using cell adhesion/internalization and FACS enrichment (68, 81, 254). We used alanine scanning of solvent exposed tyrosines to map the binding interface and elucidate important regions to be targeted for mutagenesis. Four site-saturation mutagenesis libraries were generated and subsequently screened to identify affinity-matured variants binding α5β1 integrin. Selection was carried out by panning for Caco-2 cell adhesion and internalization, which was followed by FACS enrichment using fluorescently labeled α5β1 integrin. This process led to the identification of three beneficial substitutions. Two of these substitutions introduced an RGD epitope in a region of invasin, which has previously been compared to the RGD epitope in fibronectin, responsible for β1 integrin recognition (96). Together these three substitutions resulted in a nine-fold improvement in EC_{50} compared to wild-type (measured by ELISA against α5β1 integrin). This engineered high-affinity invasin mutant termed RGD844, may aid targeted oral vaccine delivery by offering enhanced translocation through M cells.

Chapter Three sought to generate a polymeric antigen delivery system capable of testing the benefits of the RGD844 variant. This delivery system encapsulated antigen within poly(lactic-co-glycolic acid) (PLGA) microparticles. The formulation was

174

improved to encapsulate increased amounts of the model protein antigen, ovalbumin, by the addition of 5% NaCl to the external aqueous phase during the double emulsion process. Substituting the emulsification surfactant from polyvinyl alcohol to poly(ethylene-alt-maleic acid) generated particles with an increased capacity for the amount of targeting ligand that could be coupled to the particles surface. In parallel, this surfactant exchange increased the amount of encapsulated ovalbumin displayed on the particle surface. Invasin variants with different affinities toward $\alpha5\beta1$ integrin were recombinantly expressed as a fusion protein to maltose binding protein (MBP) and conjugated to the particle surface. We showed, via flow cytometry, that with similar levels of ligand on the particle surface, recognition for $\alpha5\beta1$ integrin was dependent on the invasin variant used.

These particles were then studied *in vivo* by orally administering the particles in suspension to mice. In Chapter Four, the particles were loaded with novel fluorescent nanocrystals to serve as a contrast agent for whole animal imaging. These studies suggest that the wild-type aids in retention of our microparticles in the gastroinstinal tract. The ability of these particles to modulate immune responses was also characterized in Chapter Three. Serum samples were collected from mice that received oral doses of particles conjugated to different invasin variants, encapsulating ovalbumin. The serum samples were then analyzed for specific IgG responses. This study showed that antibody humoral immunity was generated to the invasin targeting ligand but not the encapsulated ovalbumin antigen. There were not clear distinctions in immune responses between sample groups using different invasin variants for targeting. We also found serum IgG

175

responses to be generated by our soluble oral ovalbumin control group. This suggests the addition of a bystander protein, in this case 5% BSA, may be an important factor for protection of antigens delivered orally. This study has provided valuable information, which will lead to future optimizations of oral vaccines. In the future, we can consider conjugation and formulation details in order to optimize an oral microparticle vaccine delivery system based on M cell targeting.

In addition to vaccine delivery, we have created formulations of therapeutic proteins suitable for subcutaneous administration (Chapter Five). The dose requirements for delivery of biologics via the subcutaneous route often require highly concentrated formulations (201). These concentrations produce unstable formulations prone to aggregation and are too viscous to be passed through the needle of a syringe. We were able to create protein nanoclusters, with the addition of crowding agents that revert to monomer upon dilution. We showed that these dispersions yielded similar pharmacokinetic profiles as solution based formulations.

FUTURE DIRECTIONS

The generation of an affinity-matured invasin variant may lead future contributions in two areas: 1) understanding of pathogenicity by *Yersinia psuedotuberculosis and entericolitica* and 2) the employment in targeted oral vaccine delivery systems. Invasin has been heavily studied, by Isberg and others, to help understand the role it plays in pathogenicity of certain *Yersinia* strains (61, 103, 255). It has often been compared to the endogenous human $\alpha5\beta1$ integrin ligand fibronection, in particular the D911 residue of invasin and the RGD epitope of fibroectin (96). Here we

show, for the first time, that the introduction of an RGD epitope containing D911 enhances invasin's affinity toward α5β1 integrin. The fibronectin- α5β1 integrin interaction has been shown to be dynamic, acting as a "catch-bond"(75). It would be interesting to study the invasin-integrin bond strengths induced in the tensioned states in the advanced system used by Friedland et al., along with the incorporations of the three substitutions we found through our affinity maturation process. These studies may further aid in the understanding of *Yersinia* pathogenicity.

The RGD844 variant created in this work may also to lead to important advances in targeted oral vaccination. While our studies were not able to elucidate modulations in immune responses based on the invasin variant used, others have shown the ability to target M cells plays an important role (42, 93). Incorporating the RGD844 variant into these systems may lead to further improvements on current targeting strategies.

Additionally, the knowledge gained from this work also provides an important foundation for optimization of our particle-based delivery system. The lack of response to ovalbumin in our oral particle delivery systems indicated that the conjugation process used to couple the targeting ligand might alter the ability of the ovalbumin to be efficiently processed for MHC presentation. Efforts could be focused on altering the conjugation chemistry to allow for efficient antigen processing of encapsulated proteins. However, since we did observe serum IgG responses directed at our targeting ligand, the delivery system could simply be modified to co-couple the antigen(s) and the targeting ligand on the particle surface.

Given the inability to discern significant differences in immune responses due to our targeting ligand and the presence of a response in our soluble oral ovalbumin control group, certain control studies should be carried out to further understand these observations. Recently, it has been postulated that the inclusion of bystander proteins in oral vaccine delivery systems may protect antigen from proteolytic degradation, by competitive inhibition (147). We used this information, along with our simulated digestion studies, to include 5% BSA in our oral formulations. This excipient may have had pronounced effects on antigen recognition. The lack of distinction between sample groups with different invasin variants may have been due to saturation of M cell uptake. If saturation was the cause for the similarity between groups, the addition of 5% BSA may have contributed to this effect. Various doses of invasin targeted particles with and without the addition of BSA, would help elucidate the roles of bystander protein and M cell targeting. These further studies will help advance the efficacy of oral vaccines.

References

1.   M Murphy K, Travers P, Walport M, Janeway C (2008) Janeway's Immunobiology, International Student Edition.

2.   Obukhanych TV, Nussenzweig MC (2006) T-independent type II immune responses generate memory B cells. *J Exp Med* 203:305–310.

3.   De Groot AS, Scott DW (2007) Immunogenicity of protein therapeutics. *Trends Immunol* 28:482–490.

4.   Holmgren J, Czerkinsky C (2005) Mucosal immunity and vaccines. *Nat Med*:S45–S53.

5.   Kasturi SP, Sachaphibulkij K, Roy K (2005) Covalent conjugation of polyethyleneimine on biodegradable microparticles for delivery of plasmid DNA vaccines. *Biomaterials* 26:6375–6385.

6.   Singh M et al. (1997) Controlled release microparticles as a single dose hepatitis B vaccine: evaluation of immunogenicity in mice. *Vaccine* 15:475–481.

7.   Singh A et al. (2008) Efficient modulation of T-cell response by dual-mode, single-carrier delivery of cytokine-targeted siRNA and DNA vaccine to antigen-presenting cells. *Mol Ther* 16:2011–2021.

8.   Mestecky J, Nguyen H, Czerkinsky C, Kiyono H (2008) Oral immunization: an update. *Curr Opin Gastroenterol* 24:713–719.

9.   Lavelle EC, O'Hagan DT (2006) Delivery systems and adjuvants for oral vaccines. *Expert Opin Drug Deliv* 3:747–762.

10.   Levine MM et al. (1981) Duration of infection-derived immunity to cholera. *J INFECT DIS* 143:818–820.

11.   Rescigno M et al. (2001) Dendritic cells express tight junction proteins and penetrate gut epithelial monolayers to sample bacteria. *Nat Immunol* 2:361–367.

12.   Kerneis S, Bogdanova A, Kraehenbuhl JP, Pringault E (1997) Conversion by Peyer's patch lymphocytes of human enterocytes into M cells that transport bacteria. *Science* 277:949–952.

13.   Niess JH et al. (2005) CX3CR1-mediated dendritic cell access to the intestinal lumen and bacterial clearance. *Science* 307:254–258.

14.   Brayden D, Baird A (2004) Apical membrane receptors on intestinal M cells:

potential targets for vaccine delivery. *Adv Drug Deliv Rev* 56:721–726.

15. Tyrer PC, Ruth Foxwell A, Kyd JM, Otczyk DC, Cripps AW (2007) Receptor mediated targeting of M-cells. *Vaccine* 25:3204–3209.

16. Baylor NW, Egan W, Richman P (2002) Aluminum salts in vaccines--US perspective. *Vaccine* 20 Suppl 3:S18–23.

17. McCluskie MJ, Weeratna RD, Krieg AM, Davis HL (2000) CpG DNA is an effective oral adjuvant to protein antigens in mice. *Vaccine* 19:950–957.

18. McLachlan JB et al. (2008) Mast cell activators: a new class of highly effective vaccine adjuvants. *Nat Med* 14:536–541.

19. Holmgren J, Czerkinsky C, Eriksson K, Mharandi A (2003) Mucosal immunisation and adjuvants: a brief overview of recent advances and challenges. *Vaccine* 21 Suppl 2:S89–95.

20. Lauring AS, Jones JO, Andino R (2010) Rationalizing the development of live attenuated virus vaccines. *Nat Biotechnol* 28:573–579.

21. Azevedo MSP et al. (2010) An oral versus intranasal prime/boost regimen using attenuated human rotavirus or VP2 and VP6 virus-like particles with immunostimulating complexes influences protection and antibody-secreting cell responses to rotavirus in a neonatal gnotobiotic pig model. *Clin Vaccine Immunol* 17:420–428.

22. Singh M et al. (1997) Immunogenicity and protection in small-animal models with controlled-release tetanus toxoid microparticles as a single-dose vaccine. *Infect Immun* 65:1716–1721.

23. Taluja A, Youn Y, Bae Y (2007) Novel approaches in microparticulate PLGA delivery systems encapsulating proteins. *J Mater Chem* 17:4002–4014.

24. Ye M, Kim S, Park K (2010) Issues in long-term protein delivery using biodegradable microparticles. *J Control Release*.

25. Corr SC, Gahan CCGM, Hill C (2008) M-cells: origin, morphology and role in mucosal immunity and microbial pathogenesis. *FEMS Immunol Med Microbiol* 52:2–12.

26. Mazmanian SK, Round JL, Kasper DL (2008) A microbial symbiosis factor prevents intestinal inflammatory disease. *Nature* 453:620–625.

27. Mowat AM (2003) Anatomical basis of tolerance and immunity to intestinal

antigens. *Nat Rev Immunol* 3:331–341.

28. Cornes JS (1965) Number, size, and distribution of Peyer"s patches in the human small intestine: Part I The development of Peyer"s patches. *Gut* 6:225–229.

29. Brayden DJ, Jepson MA, Baird AW (2005) Keynote review: intestinal Peyer's patch M cells and oral vaccine targeting. *Drug Discov Today* 10:1145–1157.

30. Buda A, Sands C, Jepson MA (2005) Use of fluorescence imaging to investigate the structure and function of intestinal M cells. *Adv Drug Deliv Rev* 57:123–134.

31. Giannasca PJ, Giannasca KT, Leichtner AM, Neutra MR (1999) Human intestinal M cells display the sialyl Lewis A antigen. *Infect Immun* 67:946–953.

32. Kyd JM, Cripps AW (2008) Functional differences between M cells and enterocytes in sampling luminal antigens. *Vaccine* 26:6221–6224.

33. Kraehenbuhl JP, Neutra MR (1992) Molecular and cellular basis of immune protection of mucosal surfaces. *Physiol Rev* 72:853–879.

34. Gullberg E et al. (2000) Expression of specific markers and particle transport in a new human intestinal M-cell model. *Biochem Biophys Res Commun* 279:808–813.

35. Rieux des A et al. (2007) An improved in vitro model of human intestinal follicle-associated epithelium to study nanoparticle transport by M cells. *European Journal of Pharmaceutical Sciences* 30:380–391.

36. Schulte R et al. (2000) Translocation of Yersinia entrocolitica across reconstituted intestinal epithelial monolayers is triggered by Yersinia invasin binding to beta1 integrins apically expressed on M-like cells. *Cell Microbiol* 2:173–185.

37. Gullberg E et al. (2006) Identification of cell adhesion molecules in the human follicle-associated epithelium that improve nanoparticle uptake into the Peyer's patches. *J Pharmacol Exp Ther* 319:632–639.

38. G Tran Van Nhieu, R R Isberg (1993) Bacterial internalization mediated by beta 1 chain integrins is determined by ligand affinity and receptor density. *The EMBO Journal* 12:1887–1895.

39. Harokopakis E, Childers NK, Michalek SM, Zhang SS, Tomasi M (1995) Conjugation of cholera toxin or its B subunit to liposomes for targeted delivery of antigens. *J Immunol Methods* 185:31–42.

40. Shukla A, Katare OP, Singh B, Vyas SP (2010) M-cell targeted delivery of recombinant hepatitis B surface antigen using cholera toxin B subunit conjugated bilosomes. *Int J Pharm* 385:47–52.

41. Blanco LP, Dirita VJ (2006) Antibodies enhance interaction of Vibrio cholerae with intestinal M-like cells. *Infect Immun* 74:6957–6964.

42. Fievez V et al. (2009) Targeting nanoparticles to M cells with non-peptidic ligands for oral vaccination. *Eur J Pharm Biopharm* 73:16–24.

43. Kadiyala I, Loo Y, Roy K, Rice J, Leong KW (2010) Transport of chitosan-DNA nanoparticles in human intestinal M-cell model versus normal intestinal enterocytes. *Eur J Pharm Sci* 39:103–109.

44. Artis D (2008) Epithelial-cell recognition of commensal bacteria and maintenance of immune homeostasis in the gut. *Nat Rev Immunol* 8:411–420.

45. Ley RE, Peterson DA, Gordon JI (2006) Ecological and evolutionary forces shaping microbial diversity in the human intestine. *Cell* 124:837–848.

46. Turnbull EL, Yrlid U, Jenkins CD, Macpherson GG (2005) Intestinal dendritic cell subsets: differential effects of systemic TLR4 stimulation on migratory fate and activation in vivo. *J Immunol* 174:1374–1384.

47. Mazmanian SK, Kasper DL (2006) The love-hate relationship between bacterial polysaccharides and the host immune system. *Nat Rev Immunol* 6:849–858.

48. Sun JB, Rask C, Olsson T, Holmgren J, Czerkinsky C (1996) Treatment of experimental autoimmune encephalomyelitis by feeding myelin basic protein conjugated to cholera toxin B subunit. *Proc Natl Acad Sci USA* 93:7196–7201.

49. Friedman A, Weiner HL (1994) Induction of anergy or active suppression following oral tolerance is determined by antigen dosage. *Proc Natl Acad Sci USA* 91:6688–6692.

50. Coombes J, Maloy K (2007) Control of intestinal homeostasis by regulatory T cells and dendritic cells. *Semin Immunol* 19:116–126.

51. Milling SWF et al. (2009) Steady-state migrating intestinal dendritic cells induce potent inflammatory responses in naive CD4+ T cells. *Mucosal Immunology* 2:156–165.

52. Goubier A et al. (2008) Plasmacytoid dendritic cells mediate oral tolerance. *Immunity* 29:464–475.

53.   Ito T et al. (2007) Plasmacytoid dendritic cells prime IL-10-producing T regulatory cells by inducible costimulator ligand. *J Exp Med* 204:105–115.

54.   Miyamoto K et al. (2005) The ICOS molecule plays a crucial role in the development of mucosal tolerance. *J Immunol* 175:7341–7347.

55.   Tsuji N, Kosaka A (2008) Oral tolerance: intestinal homeostasis and antigen-specific regulatory T cells. *Trends Immunol* 29:532–540.

56.   Jepson MA, Clark MA (1998) Studying M cells and their role in infection. *Trends Microbiol* 6:359–365.

57.   Clark MA, Hirst BH, Jepson MA (1998) M-cell surface beta1 integrin expression and invasin-mediated targeting of Yersinia pseudotuberculosis to mouse Peyer's patch M cells. *Infect Immun* 66:1237–1243.

58.   R R Isberg, Barnes P (2001) Subversion of integrins by enteropathogenic Yersinia. *J Cell Sci* 114:21–28.

59.   Tyrer P et al. (2002) Validation and quantitation of an in vitro M-cell model. *Biochem Biophys Res Commun* 299:377–383.

60.   Marra A, R R Isberg (1997) Invasin-dependent and invasin-independent pathways for translocation of Yersinia pseudotuberculosis across the Peyer's patch intestinal epithelium. *Infect Immun* 65:3412–3421.

61.   R R Isberg, Voorhis DL, Falkow S (1987) Identification of invasin: a protein that allows enteric bacteria to penetrate cultured mammalian cells. *Cell* 50:769–778.

62.   Dersch P, R R Isberg (1999) A region of the Yersinia pseudotuberculosis invasin protein enhances integrin-mediated uptake into mammalian cells and promotes self-association. *The EMBO Journal* 18:1199–1213.

63.   Pepe JC, Miller VL (1990) The Yersinia enterocolitica inv gene product is an outer membrane protein that shares epitopes with Yersinia pseudotuberculosis invasin. *J Bacteriol* 172:3780–3789.

64.   Leong JM, Fournier RS, R R Isberg (1991) Mapping and topographic localization of epitopes of the Yersinia pseudotuberculosis invasin protein. *Infect Immun* 59:3424–3433.

65.   Leong JM, Fournier RS, Isberg RR (1990) Identification of the integrin binding domain of the Yersinia pseudotuberculosis invasin protein. *The EMBO Journal* 9:1979–1989.

66. Leong JM, Morrissey PE, R R Isberg (1993) A 76-amino acid disulfide loop in the Yersinia pseudotuberculosis invasin protein is required for integrin receptor recognition. *J Biol Chem* 268:20524–20532.

67. Saltman LH, Lu Y, Zaharias EM, R R Isberg (1996) A region of the Yersinia pseudotuberculosis invasin protein that contributes to high affinity binding to integrin receptors. *J Biol Chem* 271:23438–23444.

68. Leong JM, Morrissey PE, Marra A, R R Isberg (1995) An aspartate residue of the Yersinia pseudotuberculosis invasin protein that is critical for integrin binding. *The EMBO Journal* 14:422–431.

69. R R Isberg, Leong JM (1990) Multiple beta 1 chain integrins are receptors for invasin, a protein that promotes bacterial penetration into mammalian cells. *Cell* 60:861–871.

70. Krukonis ES, Isberg RR (2000) Integrin beta1-chain residues involved in substrate recognition and specificity of binding to invasin. *Cell Microbiol* 2:219–230.

71. Garinot M et al. (2007) PEGylated PLGA-based nanoparticles targeting M cells for oral vaccination. *J Control Release* 120:195–204.

72. Tyrer P, Ruth Foxwell A, Cripps AW, Apicella MA, Kyd JM (2006) Microbial pattern recognition receptors mediate M-cell uptake of a gram-negative bacterium. *Infect Immun* 74:625–631.

73. Van Nhieu GT, R R Isberg (1991) The Yersinia pseudotuberculosis invasin protein and human fibronectin bind to mutually exclusive sites on the alpha 5 beta 1 integrin receptor. *J Biol Chem* 266:24367–24375.

74. Palumbo RN, Wang C (2006) Bacterial invasin: structure, function, and implication for targeted oral gene delivery. *Current drug delivery* 3:47–53.

75. Friedland J, Lee M, Boettiger D (2009) Mechanically Activated Integrin Switch Controls {alpha}5{beta}1 Function. *Science* 323:642.

76. Brett S, Mazurov A, Charles I, Tite J (1993) The invasin protein of Yersinia spp. provides co-stimulatory activity to human T cells through interaction with β integrins. *Eur J Immunol* 23.

77. Schulte R et al. (2000) Yersinia enterocolitica invasin protein triggers IL-8 production in epithelial cells via activation of Rel p65-p65 homodimers. *FASEB J* 14:1471–1484.

78.   Autenrieth S, Autenrieth I (2008) Yersinia enterocolitica: Subversion of adaptive immunity and implications for vaccine development. *International Journal of Medical Microbiology* 298:69–77.

79.   Hussain N, Florence AT (1998) Utilizing bacterial mechanisms of epithelial cell entry: invasin-induced oral uptake of latex nanoparticles. *Pharm Res* 15:153–156.

80.   Bühler OT et al. (2006) The Yersinia enterocolitica invasin protein promotes major histocompatibility complex class I- and class II-restricted T-cell responses. *Infect Immun* 74:4322–4329.

81.   Critchley-Thorne RJ, Stagg AJ, Vassaux G (2006) Recombinant Escherichia coli expressing invasin targets the Peyer's patches: the basis for a bacterial formulation for oral vaccination. *Mol Ther* 14:183–191.

82.   Mishra N et al. (2010) Recent advances in mucosal delivery of vaccines: role of mucoadhesive/biodegradable polymeric carriers. *Expert Opin Ther Pat* 20:661–679.

83.   Bomsel M et al. (2011) Immunization with HIV-1 gp41 Subunit Virosomes Induces Mucosal Antibodies Protecting Nonhuman Primates against Vaginal SHIV Challenges. *Immunity* 34:269–280.

84.   Neutra MR, Kozlowski PA (2006) Mucosal vaccines: the promise and the challenge. *Nat Rev Immunol* 6:148–158.

85.   Minor P (2009) Vaccine-derived poliovirus (VDPV): Impact on poliomyelitis eradication. *Vaccine* 27:2649–2652.

86.   De Temmerman M-L et al. (2011) Particulate vaccines: on the quest for optimal delivery and immune response. *Drug Discov Today* 16:569–582.

87.   Singh M, O'Hagan D (1998) The preparation and characterization of polymeric antigen delivery systems for oral administration. *Adv Drug Deliv Rev* 34:285–304.

88.   Azizi A, Kumar A, Diaz-Mitoma F, Mestecky J (2010) Enhancing oral vaccine potency by targeting intestinal m cells. *PLoS Pathog* 6:e1001147.

89.   Kraehenbuhl JP, Neutra MR (2000) Epithelial M cells: differentiation and function. *Annu Rev Cell Dev Biol* 16:301–332.

90.   KuoLee R, Chen W (2008) M cell-targeted delivery of vaccines and therapeutics. *Expert Opin Drug Deliv*.

91.   Yoo M-K et al. (2010) Targeted delivery of chitosan nanoparticles to Peyer's patch using M cell-homing peptide selected by phage display technique. *Biomaterials*.

92.   Gupta PN, Khatri K, Goyal AK, Mishra N, Vyas SP (2007) M-cell targeted biodegradable PLGA nanoparticles for oral immunization against hepatitis B. *Journal of Drug Targeting* 15:701–713.

93.   Nochi T et al. (2007) A novel M cell-specific carbohydrate-targeted mucosal vaccine effectively induces antigen-specific immune responses. *J Exp Med* 204:2789–2796.

94.   Carniel E, Autenrieth I, Cornelis G, Fukushima H (2006) Y. enterocolitica and Y. pseudotuberculosis. *Prokaryotes*.

95.   Fairman JW et al. (2012) Crystal Structures of the Outer Membrane Domain of Intimin and Invasin from Enterohemorrhagic E. coli and Enteropathogenic Y. pseudotuberculosis. *Structure*.

96.   Hamburger ZA, Brown MS, R R Isberg, Bjorkman PJ (1999) Crystal structure of invasin: a bacterial integrin-binding protein. *Science* 286:291–295.

97.   Dersch P, R R Isberg (2000) An immunoglobulin superfamily-like domain unique to the Yersinia pseudotuberculosis invasin protein is required for stimulation of bacterial uptake via integrin receptors. *Infect Immun* 68:2930–2938.

98.   Rankin S, R R Isberg, Leong JM (1992) The integrin-binding domain of invasin is sufficient to allow bacterial entry into mammalian cells. *Infect Immun* 60:3909–3912.

99.   Fellouse FA, Wiesmann C, Sidhu SS (2004) Synthetic antibodies from a four-amino-acid code: a dominant role for tyrosine in antigen recognition. *Proc Natl Acad Sci USA* 101:12467–12472.

100.   Daugherty PS (2007) Protein engineering with bacterial display. *Curr Opin Struct Biol* 17:474–480.

101.   Kenrick S, Rice J, Daugherty P (2007) Flow cytometric sorting of bacterial surface-displayed libraries. *Curr Protoc Cytom* Chapter 4:Unit4.6.

102.   Bessette PH, Rice JJ, Daugherty PS (2004) Rapid isolation of high-affinity protein binding peptides using bacterial display. *Protein Eng Des Sel* 17:731–739.

103. Ragnarsson EGE et al. (2008) Yersinia pseudotuberculosis induces transcytosis of nanoparticles across human intestinal villus epithelium via invasin-dependent macropinocytosis. *Lab Invest* 88:1215–1226.

104. Heise T, Dersch P (2006) Identification of a domain in Yersinia virulence factor YadA that is crucial for extracellular matrix-specific cell adhesion and uptake. *Proc Natl Acad Sci USA* 103:3375–3380.

105. Lind PA, Andersson DI (2008) Whole-genome mutational biases in bacteria. *Proc Natl Acad Sci USA* 105:17878–17883.

106. Johansson S, Svineng G, Wennerberg K, Armulik A, Lohikangas L (1997) Fibronectin-integrin interactions. *Front Biosci* 2:d126–46.

107. Takagi J, Strokovich K, Springer TA, Walz T (2003) Structure of integrin alpha5beta1 in complex with fibronectin. *The EMBO Journal* 22:4607–4615.

108. Mould AP et al. (2005) Evidence that monoclonal antibodies directed against the integrin beta subunit plexin/semaphorin/integrin domain stimulate function by inducing receptor extension. *J Biol Chem* 280:4238–4246.

109. Cluzel C et al. (2005) The mechanisms and dynamics of (alpha)v(beta)3 integrin clustering in living cells. *J Cell Biol* 171:383–392.

110. Luo B-H, Carman CV, Springer TA (2007) Structural basis of integrin regulation and signaling. *Annu Rev Immunol* 25:619–647.

111. Wang N, Butler JP, Ingber DE (1993) Mechanotransduction across the cell surface and through the cytoskeleton. *Science* 260:1124–1127.

112. ALTMAN G, HORAN R, Martin I, Farhadi J (2002) Cell differentiation by mechanical stress. *The FASEB Journal*.

113. Wang N (1994) Control of cytoskeletal mechanics by extracellular matrix, cell shape, and mechanical tension. *Biophys J*.

114. Lin CQ, Bissell MJ (1993) Multi-faceted regulation of cell differentiation by extracellular matrix. *FASEB J* 7:737–743.

115. Simonet M, Riot B, Fortineau N, Berche P (1996) Invasin production by Yersinia pestis is abolished by insertion of an IS200-like element within the inv gene. *Infect Immun* 64:375–379.

116. Dou Y, Fan Y, Zhao J, Gregersen H (2006) Longitudinal residual strain and stress-strain relationship in rat small intestine. *Biomed Eng Online* 5:37.

117. Dou Y, Zhao J, Gregersen H (2003) Morphology and stress-strain properties along the small intestine in the rat. *J Biomech Eng* 125:266–273.

118. Gregersen H (1996) Biomechanics of the gastrointestinal tract. *Neurogastroenterology & Motility*.

119. Guzman LM, Belin D, Carson MJ, Beckwith J (1995) Tight regulation, modulation, and high-level expression by vectors containing the arabinose PBAD promoter. *J Bacteriol* 177:4121–4130.

120. Sidhu S Constructing phage display libraries by oligonucleotide-directed mutagenesis. *Phage display: a practical approach*.

121. Levy R, Weiss R, Chen G, Iverson BL, Georgiou G (2001) Production of correctly folded Fab antibody fragment in the cytoplasm of Escherichia coli trxB gor mutants via the coexpression of molecular chaperones. *Protein Expr Purif* 23:338–347.

122. Challacombe SJ, Rahman D, Jeffery H, Davis SS, O'Hagan DT (1992) Enhanced secretory IgA and systemic IgG antibody responses after oral immunization with biodegradable microparticles containing antigen. *Immunology* 76:164–168.

123. Pickard JM, Chervonsky AV (2010) Sampling of the intestinal microbiota by epithelial M cells. *Curr Gastroenterol Rep* 12:331–339.

124. Fievez V et al. (2010) In vitro identification of targeting ligands of human M cells by phage display. *Int J Pharm*.

125. Gupta PN et al. (2006) Lectin anchored stabilized biodegradable nanoparticles for oral immunization 1. Development and in vitro evaluation. *Int J Pharm* 318:163–173.

126. Jaganathan KS, Singh P, Prabakaran D, Mishra V, Vyas SP (2004) Development of a single-dose stabilized poly(D,L-lactic-co-glycolic acid) microspheres-based vaccine against hepatitis B. *J Pharm Pharmacol* 56:1243–1250.

127. Zhu G, Mallery SR, Schwendeman SP (2000) Stabilization of proteins encapsulated in injectable poly (lactide- co-glycolide). *Nat Biotechnol* 18:52–57.

128. Castellanos IJ, Carrasquillo KG, López JD, Alvarez M, Griebenow K (2001) Encapsulation of bovine serum albumin in poly(lactide-co-glycolide) microspheres by the solid-in-oil-in-water technique. *J Pharm Pharmacol* 53:167–178.

129. Sharif S, O'Hagan D (1995) A comparison of alternative methods for the

determination of the levels of proteins entrapped in poly(lactide-co-glycolide) microparticles. *Int J Pharm* 115:259–263.

130. Liu R, Huang S-S, Wan Y-H, Ma G-H, Su Z-G (2006) Preparation of insulin-loaded PLA/PLGA microcapsules by a novel membrane emulsification method and its release in vitro. *Colloids Surf B Biointerfaces* 51:30–38.

131. Katare YK, Panda AK (2006) Influences of excipients on in vitro release and in vivo performance of tetanus toxoid loaded polymer particles. *Eur J Pharm Sci* 28:179–188.

132. Scholes PD et al. (1999) Detection and determination of surface levels of poloxamer and PVA surfactant on biodegradable nanospheres using SSIMS and XPS. *J Control Release* 59:261–278.

133. Keegan M, Falcone J, Leung T, Saltzman W (2004) Biodegradable microspheres with enhanced capacity for covalently bound surface ligands. *Macromolecules* 37:9779–9784.

134. Gramoun A et al. (2010) Fibronectin inhibits osteoclastogenesis while enhancing osteoclast activity via nitric oxide and interleukin-1β-mediated signaling pathways. *J Cell Biochem* 111:1020–1034.

135. Coffman RL, Sher A, Seder RA (2010) Vaccine adjuvants: putting innate immunity to work. *Immunity* 33:492–503.

136. Aida Y, Pabst MJ (1990) Removal of endotoxin from protein solutions by phase separation using Triton X-114. *J Immunol Methods* 132:191–195.

137. Carpenter JF, Chang BS, Randolph TW (2005) in *Lyophilization Of Biopharmaceuticals*, eds Costantino HR, Pikal MJ (AAPS Press, Arlington, VA), pp 423–442.

138. Kaushik JK, Bhat R (2003) Why is trehalose an exceptional protein stabilizer? An analysis of the thermal stability of proteins in the presence of the compatible osmolyte trehalose. *J Biol Chem* 278:26458–26465.

139. Lowman AM, Morishita M, Kajita M, Nagai T, Peppas NA (1999) Oral delivery of insulin using pH-responsive complexation gels. *J Pharm Sci* 88:933–937.

140. Trček J et al. (2011) Gut proteases target Yersinia invasin in vivo. 4:129.

141. Morishita M, Peppas NA (2006) Is the oral route possible for peptide and protein drug delivery? *Drug Discov Today* 11:905–910.

142.   Russell TL et al. (1993) Upper gastrointestinal pH in seventy-nine healthy, elderly, North American men and women. *Pharm Res* 10:187–196.

143.   Jepson MA, Clark MA, Hirst BH (2004) M cell targeting by lectins: a strategy for mucosal vaccination and drug delivery. *Adv Drug Deliv Rev* 56:511–525.

144.   Bejugam N, Uddin A, Gayakwad S, D'Souza M (2008) Formulation and evaluation of albumin microspheres and its enteric coating using a spray-dryer. *Journal of Microencapsulation* 25:577–583.

145.   McConnell EL, Basit AW, Murdan S (2008) Measurements of rat and mouse gastrointestinal pH, fluid and lymphoid tissue, and implications for in-vivo experiments. *J Pharm Pharmacol* 60:63–70.

146.   Miller DA, DiNunzio JC, Yang W, McGinity JW, Williams RO (2008) Targeted intestinal delivery of supersaturated itraconazole for improved oral absorption. *Pharm Res* 25:1450–1459.

147.   Reuter F, Bade S, Hirst TR, Frey A (2009) Bystander protein protects potential vaccine-targeting ligands against intestinal proteolysis. *J Control Release* 137:98–103.

148.   Piper DW, Fenton BH (1965) pH stability and activity curves of pepsin with special reference to their clinical importance. *Gut* 6:506–508.

149.   Klinman DM et al. (2010) Immunostimulatory CpG oligonucleotides: Effect on gene expression and utility as vaccine adjuvants. *Vaccine* 28:1919–1923.

150.   Wagner H (2009) The immunogenicity of CpG-antigen conjugates. *Adv Drug Deliv Rev* 61:243–247.

151.   Shargh VH et al. (2012) Liposomal SLA co-incorporated with PO CpG ODNs or PS CpG ODNs induce the same protection against the murine model of leishmaniasis. *Vaccine*.

152.   Haas T et al. (2008) The DNA sugar backbone 2' deoxyribose determines toll-like receptor 9 activation. *Immunity* 28:315–323.

153.   Nembrini C et al. (2011) PNAS Plus: From the Cover: Nanoparticle conjugation of antigen enhances cytotoxic T-cell responses in pulmonary vaccination. *Proc Natl Acad Sci USA* 108:E989–E997.

154.   Kenawy ER, Abdel Hay F, Newehy El M, Ottenbrite RM (2008) Effect of pH on the drug release rate from a new polymer–drug conjugate system. *Polymer International* 57:85–91.

155. Reddy ST et al. (2007) Exploiting lymphatic transport and complement activation in nanoparticle vaccines. *Nat Biotechnol* 25:1159–1164.

156. Slütter B et al. (2009) Mechanistic study of the adjuvant effect of biodegradable nanoparticles in mucosal vaccination. *J Control Release* 138:113–121.

157. Tabata Y, Inoue Y, Ikada Y (1996) Size effect on systemic and mucosal immune responses induced by oral administration of biodegradable microspheres. *Vaccine* 14:1677–1685.

158. Fineschi B, Miller J (1997) Endosomal proteases and antigen processing. *Trends in biochemical sciences* 22:377–382.

159. Puzzo DP et al. (2011) Visible colloidal nanocrystal silicon light-emitting diode. *Nano Lett* 11:1585–1590.

160. Steckel JS, Coe Sullivan S, Bulović V, Bawendi MG (2003) 1.3 μm to 1.55 μm tunable electroluminescence from PbSe quantum dots embedded within an organic device. *Advanced Materials* 15:1862–1866.

161. Gur I, Fromer NA, Geier ML, Alivisatos AP (2005) Air-stable all-inorganic nanocrystal solar cells processed from solution. *Science* 310:462–465.

162. Panthani MG et al. (2008) Synthesis of CuInS2, CuInSe2, and Cu(InxGa(1-x))Se2 (CIGS) nanocrystal "inks" for printable photovoltaics. *J Am Chem Soc* 130:16770–16777.

163. Pattantyus-Abraham AG et al. (2010) Depleted-heterojunction colloidal quantum dot solar cells. *ACS nano* 4:3374–3380.

164. Michalet X et al. (2005) Quantum dots for live cells, in vivo imaging, and diagnostics. *Science* 307:538–544.

165. Medintz IL, Uyeda HT, Goldman ER, Mattoussi H (2005) Quantum dot bioconjugates for imaging, labelling and sensing. *Nat Mater* 4:435–446.

166. Hessel CM et al. (2010) Alkyl passivation and amphiphilic polymer coating of silicon nanocrystals for diagnostic imaging. *Small* 6:2026–2034.

167. Farokhzad OC, Langer R (2006) Nanomedicine: developing smarter therapeutic and diagnostic modalities. *Adv Drug Deliv Rev* 58:1456–1459.

168. Resch-Genger U, Grabolle M, Cavaliere-Jaricot S, Nitschke R, Nann T (2008) Quantum dots versus organic dyes as fluorescent labels. *Nat Meth* 5:763–775.

169. Fountaine TJ, Wincovitch SM, Geho DH, Garfield SH, Pittaluga S (2006)

Multispectral imaging of clinically relevant cellular targets in tonsil and lymphoid tissue using semiconductor quantum dots. *Mod Pathol* 19:1181–1191.

170.   Hessel CM et al. (2011) Copper selenide nanocrystals for photothermal therapy. *Nano Lett* 11:2560–2566.

171.   Harbold JM et al. (2005) Time-resolved intraband relaxation of strongly confined electrons and holes in colloidal PbSe nanocrystals. *Physical Review B* 72:195312.

172.   Murphy JE et al. (2006) PbTe colloidal nanocrystals: synthesis, characterization, and multiple exciton generation. *J Am Chem Soc* 128:3241–3247.

173.   Peng ZA, Peng X (2001) Formation of high-quality CdTe, CdSe, and CdS nanocrystals using CdO as precursor. *J Am Chem Soc* 123:183–184.

174.   Guzelian A, Banin U, Kadavanich A, Peng X, Alivisatos A (1996) Colloidal chemical synthesis and characterization of InAs nanocrystal quantum dots. *Appl Phys Lett* 69:1432.

175.   Harris DK et al. (2011) Synthesis of cadmium arsenide quantum dots luminescent in the infrared. *J Am Chem Soc* 133:4676–4679.

176.   Zhong H et al. (2011) Colloidal CuInSe2 Nanocrystals in the Quantum Confinement Regime: Synthesis, Optical Properties and Electroluminescence. *The Journal of Physical Chemistry C*.

177.   Steinhagen C et al. (2009) Synthesis of Cu(2)ZnSnS(4) nanocrystals for use in low-cost photovoltaics. *J Am Chem Soc* 131:12554–12555.

178.   Allen PM, Bawendi MG (2008) Ternary I-III-VI quantum dots luminescent in the red to near-infrared. *J Am Chem Soc* 130:9240–9241.

179.   Li L et al. (2009) Highly luminescent CuInS2/ZnS core/shell nanocrystals: cadmium-free quantum dots for in vivo imaging. *Chemistry of Materials* 21:2422–2429.

180.   Chiang MY, Chang SH, Chen CY, Yuan FW, Tuan HY (2011) Quaternary CuIn (S1– x Se x) 2 Nanocrystals: Facile Heating-Up Synthesis, Band Gap Tuning, and Gram-Scale Production. *The Journal of Physical Chemistry C*.

181.   Chichibu S (1997) Room-temperature near-band-edge photoluminescence from CuInSe heteroepitaxial layers grown by metalorganic vapor phase epitaxy. *Appl Phys Lett* 70:1840.

182. Schwarz R, Kaspar A, Seelig J, Künnecke B (2002) Gastrointestinal transit times in mice and humans measured with 27Al and 19F nuclear magnetic resonance. *Magn Reson Med* 48:255–261.

183. Li L et al. (2011) Efficient synthesis of highly luminescent copper indium sulfide-based core/shell nanocrystals with surprisingly long-lived emission. *J Am Chem Soc* 133:1176–1179.

184. Reichert JM, Rosensweig CJ, Faden LB, Dewitz MC (2005) Monoclonal antibody successes in the clinic. *Nat Biotechnol* 23:1073–1078.

185. Nelson AL, Dhimolea E, Reichert JM (2010) Development trends for human monoclonal antibody therapeutics. *Nat Rev Drug Discov* 9:767–774.

186. Trevino SR, Scholtz JM, Pace CN (2008) Measuring and increasing protein solubility. *J Pharm Sci* 97:4155–4166.

187. Chennamsetty N, Voynov V, Kayser V, Helk B, Trout BL (2009) Design of therapeutic proteins with enhanced stability. *Proc Natl Acad Sci USA* 106:11937–11942.

188. Maynard JA et al. (2002) Protection against anthrax toxin by recombinant antibody fragments correlates with antigen affinity. *Nat Biotechnol* 20:597–601.

189. Frokjaer S, Otzen DE (2005) Protein drug stability: a formulation challenge. *Nat Rev Drug Discov* 4:298–306.

190. Yang MX et al. (2003) Crystalline monoclonal antibodies for subcutaneous delivery. *Proc Natl Acad Sci USA* 100:6934–6939.

191. Anonymous (2010) Rituximab full prescribing information. *South San Francisco, California: Genentech, Inc*:1–38.

192. Shire SJ, Shahrokh Z, Liu J (2004) Challenges in the development of high protein concentration formulations. *J Pharm Sci* 93:1390–1402.

193. Dani B, Platz R, Tzannis ST (2007) High concentration formulation feasibility of human immoglubulin G for subcutaneous administration. *J Pharm Sci* 96:1504–1517.

194. Neal BL, Asthagiri D, Lenhoff AM (1998) Molecular origins of osmotic second virial coefficients of proteins. *Biophys J* 75:2469–2477.

195. Chi EY et al. (2003) Roles of conformational stability and colloidal stability in the aggregation of recombinant human granulocyte colony-stimulating factor.

Protein Sci 12:903–913.

196. Harn N, Allan C, Oliver C, Middaugh CR (2007) Highly concentrated monoclonal antibody solutions: direct analysis of physical structure and thermal stability. *J Pharm Sci* 96:532–546.

197. Young TM, Roberts CJ (2009) Structure and thermodynamics of colloidal protein cluster formation: comparison of square-well and simple dipolar models. *J Chem Phys* 131:125104.

198. Liu J, Nguyen MDH, Andya JD, Shire SJ (2005) Reversible self-association increases the viscosity of a concentrated monoclonal antibody in aqueous solution. *J Pharm Sci* 94:1928–1940.

199. Sear RP (2006) Interactions in protein solutions. *Current opinion in colloid & interface science* 11:35–39.

200. Curtis RA, Prausnitz JM, Blanch HW (1998) Protein-protein and protein-salt interactions in aqueous protein solutions containing concentrated electrolytes. *Biotechnol Bioeng* 57:11–21.

201. Johnston KP et al. (2012) Concentrated Dispersions of Equilibrium Protein Nanoclusters That Reversibly Dissociate into Active Monomers. *ACS nano* 6:1357–1369.

202. Scherer TM, Liu J, Shire SJ, Minton AP (2010) Intermolecular interactions of IgG1 monoclonal antibodies at high concentrations characterized by light scattering. *The journal of physical chemistry B* 114:12948–12957.

203. Kendrick BS, Carpenter JF, Cleland JL, Randolph TW (1998) A transient expansion of the native state precedes aggregation of recombinant human interferon-gamma. *Proc Natl Acad Sci USA* 95:14142–14146.

204. Wang W, Nema S, Teagarden D (2010) Protein aggregation--pathways and influencing factors. *Int J Pharm* 390:89–99.

205. Miller MA, Engstrom JD, Ludher BS, Johnston KP (2010) Low viscosity highly concentrated injectable nonaqueous suspensions of lysozyme microparticles. *Langmuir* 26:1067–1074.

206. DeFelippis MR, Akers MJ (2000) in *In Pharmaceutical Formulation Development of Peptides and Proteins*, eds Frokjaer S, Hovgaard L (Taylor & Francis Ltd., Philadelphia, PA), pp 113–143.

207. Shenoy B, Wang Y, Shan W, Margolin AL (2001) Stability of crystalline

proteins. *Biotechnol Bioeng* 73:358–369.

208. Foster TP et al. (1997) Sustained elevated serum somatotropin concentrations in Holstein steers following subcutaneous delivery of a growth hormone releasing factor analog dispersed in water, oil or microspheres. *J Control Release* 47:91–99.

209. Putney SD, Burke PA (1998) Improving protein therapeutics with sustained-release formulations. *Nat Biotechnol* 16:153–157.

210. Fu K, Klibanov AM, Langer R (2000) Protein stability in controlled-release systems. *Nat Biotechnol* 18:24–25.

211. Tae G, Kornfield JA, Hubbell JA (2005) Sustained release of human growth hormone from in situ forming hydrogels using self-assembly of fluoroalkyl-ended poly(ethylene glycol). *Biomaterials* 26:5259–5266.

212. Mok H, Park TG (2008) Water-free microencapsulation of proteins within PLGA microparticles by spray drying using PEG-assisted protein solubilization technique in organic solvent. *Eur J Pharm Biopharm* 70:137–144.

213. Gombotz W, Pettit D (1995) Biodegradable polymers for protein and peptide drug delivery. *Bioconjug Chem* 6:332–351.

214. Cheung MS, Klimov D, Thirumalai D (2005) Molecular crowding enhances native state stability and refolding rates of globular proteins. *Proc Natl Acad Sci USA* 102:4753–4758.

215. Shen VK, Cheung JK, Errington JR, Truskett TM (2009) Insights into crowding effects on protein stability from a coarse-grained model. *J Biomech Eng* 131:071002.

216. Sato H, Sato Y (1990) Protective activities in mice of monoclonal antibodies against pertussis toxin. *Infect Immun* 58:3369–3374.

217. Sutherland JN, Maynard JA (2009) Characterization of a key neutralizing epitope on pertussis toxin recognized by monoclonal antibody 1B7. *Biochemistry* 48:11982–11993.

218. Strickley RG (2004) Solubilizing excipients in oral and injectable formulations. *Pharm Res* 21:201–230.

219. Carpenter JF, Chang BS, Garzon-Rodriguez W, Randolph TW (2002) *Rational design of stable lyophilized protein formulations: theory and practice* (Pharmaceutical biotechnology).

220. Engstrom JD et al. (2007) Stable high surface area lactate dehydrogenase particles produced by spray freezing into liquid nitrogen. *Eur J Pharm Biopharm* 65:163–174.

221. Engstrom JD et al. (2008) Formation of stable submicron protein particles by thin film freezing. *Pharm Res* 25:1334–1346.

222. Souillac PO, Middaugh CR, Rytting JH (2002) Investigation of protein/carbohydrate interactions in the dried state. 2. Diffuse reflectance FTIR studies. *Int J Pharm* 235:207–218.

223. Timasheff SN (1992) in *Stability of Protein Pharmaceuticals*, eds Ahern TJ, Manning MC (Springer), pp 265–285.

224. Carpenter JF, Izutsu KI (2004) *Freezing-and drying-induced perturbations of protein structure and mechanisms of protein protection by stabilizing additives* eds Rey L, May JC (Marcel Dekker, Inc).

225. Allison SD, Chang B, Randolph TW, Carpenter JF (1999) Hydrogen bonding between sugar and protein is responsible for inhibition of dehydration-induced protein unfolding. *Arch Biochem Biophys* 365:289–298.

226. Webb SD, Cleland JL, Carpenter JF, Randolph TW (2003) Effects of annealing lyophilized and spray-lyophilized formulations of recombinant human interferon-gamma. *J Pharm Sci* 92:715–729.

227. Yu Z, Garcia AS, Johnston KP, Williams RO (2004) Spray freezing into liquid nitrogen for highly stable protein nanostructured microparticles. *Eur J Pharm Biopharm* 58:529–537.

228. Kueltzo LA, Wang W, Randolph TW, Carpenter JF (2008) Effects of solution conditions, processing parameters, and container materials on aggregation of a monoclonal antibody during freeze-thawing. *J Pharm Sci* 97:1801–1812.

229. Costantino HR et al. (2000) Protein spray-freeze drying. Effect of atomization conditions on particle size and stability. *Pharm Res* 17:1374–1383.

230. Engstrom JD, Simpson DT, Lai ES, Williams RO, Johnston KP (2007) Morphology of protein particles produced by spray freezing of concentrated solutions. *Eur J Pharm Biopharm* 65:149–162.

231. Maa YF, Prestrelski SJ (2000) Biopharmaceutical powders: particle formation and formulation considerations. *Curr Pharm Biotechnol* 1:283–302.

232. AM K, AP C, KS S, CF Z (2000) Effects of polyethylene glycol on protein

interactions. *J Chem Phys* 113:9863–9873.

233. Lu PJ et al. (2008) Gelation of particles with short-range attraction. *Nature* 453:499–503.

234. Boncina M, Rescic J, Vlachy V (2008) Solubility of lysozyme in polyethylene glycol-electrolyte mixtures: the depletion interaction and ion-specific effects. *Biophys J* 95:1285–1294.

235. Shulgin IL, Ruckenstein E (2006) Preferential hydration and solubility of proteins in aqueous solutions of polyethylene glycol. *Biophys Chem* 120:188–198.

236. Hiemenz PC, Rajagopalan R (1997) *Principles of colloid and surface chemistry* (Marcel Dekker, Inc, New York). 3rd Ed.

237. Porcar L et al. (2009) Formation of the dynamic clusters in concentrated lysozyme protein solutions. *J Phys Chem Lett* 1:126–129.

238. Laflèche F, Durand D, Nicolai T (2003) Association of adhesive spheres formed by hydrophobically end-capped PEO. 1. Influence of the presence of single end-capped PEO. *Macromolecules* 36:1331–1340.

239. Kanai S, Liu J, Patapoff TW, Shire SJ (2008) Reversible self-association of a concentrated monoclonal antibody solution mediated by Fab-Fab interaction that impacts solution viscosity. *J Pharm Sci* 97:4219–4227.

240. Gabrielson JP et al. (2007) Quantitation of aggregate levels in a recombinant humanized monoclonal antibody formulation by size-exclusion chromatography, asymmetrical flow field flow fractionation, and sedimentation velocity. *J Pharm Sci* 96:268–279.

241. Saluja A, Kalonia DS (2008) Nature and consequences of protein-protein interactions in high protein concentration solutions. *Int J Pharm* 358:1–15.

242. Maas C, Hermeling S, Bouma B, Jiskoot W, Gebbink MFBG (2007) A role for protein misfolding in immunogenicity of biopharmaceuticals. *J Biol Chem* 282:2229–2236.

243. Pincus DL, Thirumalai D (2009) Crowding effects on the mechanical stability and unfolding pathways of ubiquitin. *The journal of physical chemistry B* 113:359–368.

244. Desai UR, Klibanov AM (1995) Assessing the structural integrity of a lyophilized protein in organic solvents. *J Am Chem Soc* 117:3940–3945.

245.   Roberts CJ, Debenedetti PG (2002) Engineering pharmaceutical stability with amorphous solids. *AIChE Journal* 48:1140–1144.

246.   Krishnan S et al. (2002) Aggregation of granulocyte colony stimulating factor under physiological conditions: characterization and thermodynamic inhibition. *Biochemistry* 41:6422–6431.

247.   Zhou H-X, Rivas G, Minton AP (2008) Macromolecular crowding and confinement: biochemical, biophysical, and potential physiological consequences. *Annu Rev Biophys* 37:375–397.

248.   Wang W, Wang EQ, Balthasar JP (2008) Monoclonal antibody pharmacokinetics and pharmacodynamics. *Clin Pharmacol Ther* 84:548–558.

249.   Tabrizi MA, Tseng CML, Roskos LK (2006) Elimination mechanisms of therapeutic monoclonal antibodies. *Drug Discov Today* 11:81–88.

250.   Sutherland JN, Chang C, Yoder SM, Rock MT, Maynard JA (2011) Antibodies recognizing protective pertussis toxin epitopes are preferentially elicited by natural infection versus acellular immunization. *Clin Vaccine Immunol* 18:954–962.

251.   Gillenius P, Jäätmaa E, Askelöf P, Granström M, Tiru M (1985) The standardization of an assay for pertussis toxin and antitoxin in microplate culture of Chinese hamster ovary cells. *J Biol Stand* 13:61–66.

252.   Miller MA et al. (2012) Antibody nanoparticle dispersions formed with mixtures of crowding molecules retain activity and In Vivo bioavailability. *J Pharm Sci*:n/a–n/a.

253.   Jain AK et al. (2010) PEG-PLA-PEG block copolymeric nanoparticles for oral immunization against hepatitis B. *Int J Pharm* 387:253–262.

254.   Daugherty PS, Chen G, Olsen MJ, Iverson BL, Georgiou G (1998) Antibody affinity maturation using bacterial surface display. *Protein Eng* 11:825–832.

255.   Dube P (2009) Interaction of Yersinia with the gut: mechanisms of pathogenesis and immune evasion. *Curr Top Microbiol Immunol* 337:61–91.